NEW APPROACH TO OMEGA PPCs

Peter B. Morris

Radha R. Gupta

THE ANALYTIC SCIENCES CORPORATION
55 Walkers Brook Drive
Reading, Massachusetts 01867

AD-A215 610

November 1989

Final Report

Prepared for:

**U.S. DEPARTMENT OF TRANSPORTATION
UNITED STATES COAST GUARD
OMEGA Navigation System Center
Alexandria, Virginia 22310**

TECHNICAL REPORT DOCUMENTATION PAGE

1. REPORT NO.	2. GOVERNMENT ACCESSION NO.	3. RECIPIENT'S CATALOG NO.

4. TITLE AND SUBTITLE	5. REPORT DATE
New Approach to Omega PPCs	November 1989
	6. PERFORMING ORGANIZATION CODE

7. AUTHOR(S)	8. PERFORMING ORGANIZATION REPORT NO.
P.B. Morris, R.R. Gupta	TIM-5351-9-1

9. PERFORMING ORGANIZATION NAME AND ADDRESS	10. WORK UNIT NO. (TRAIS)
The Analytic Sciences Corporation 55 Walkers Brook Drive Reading, MA 01867	11. CONTRACT OR GRANT NO. DTCG 23-86-C-20024 Task Order No. 88-0002

12. SPONSORING AGENCY NAME AND ADDRESS	13. TYPE OF REPORT AND PERIOD COVERED
U.S. Department of Transportation U.S. Coast Guard Omega Navigation System Center 7323 Telegraph Road Alexandria, VA 22310-3998	Final Report September 1988 — November 1989
	14. SPONSORING AGENCY CODE

15. SUPPLEMENTARY NOTES

16. ABSTRACT

The currently available propagation correction (PPC) model algorithm maintained by the U.S. Coast Guard Omega Navigation System Center was developed in 1980. Although an improvement over the earlier 1974 algorithm, the 1980 PPC model exhibits a number of deficiencies. To correct these deficiencies, a new approach to modeling PPCs is presented. This model incorporates semi-empirical forms directly into the time-dependent portions of the model, thus insuring that the PPC predictions are directly data-driven and data collected during path transition conditions may be used for model calibration. A geomagnetic conductivity sub-model is described which provides effective phase velocity and excitation factor phase functional forms for day or night path segments with given geomagnetic bearing, geomagnetic latitude, and ground conductivity. This sub-model describes all space-dependent quantities (on which phase depends) except for the spatially anomalous ionospheres of the auroral and polar regions. A diurnal sub-model is described in which the diurnal phase behavior on a propagation path is treated as a sum of discrete phase changes on path segments having ionospheric reflection heights determined from classical Chapman photoionization models. In addition, onset and recovery times for sunrise and sunset are characterized by several parameters which can be adjusted to fit observed data. Nighttime phase is modeled on the basis of Lyman-alpha scattering into the nighttime hemisphere. The calculation of the total phase variation differs from the 1980 PPC model; the spatial and temporal sub-models are combined using three types of evolution functions to drive the solar zenith angle dependence of the functional forms.

17. KEY WORDS	18. DISTRIBUTION STATEMENT
Omega signal propagation; VLF Phase Data Propagation Correction (PPC); Geomagnetic Field Semi-empirical model; Model Calibration Diurnal Phase Behavior; Ionosphere	Document is available to the U.S. Public through the National Technical Information Service, Springfield, VA 22161

19. SECURITY CLASSIF. (Of This Report)	20. SECURITY CLASSIF. (Of This Page)	21. NO. OF PAGES	22. PRICE
UNCLASSIFIED	UNCLASSIFIED		

F910
6/21/88

NOTICE

This document is disseminated under the sponsorship of the Department of Transportation in the interest of information exchange. The United Stated Government assumes no liability for its contents or use thereof.

METRIC CONVERSION FACTORS

Approximate Conversions to Metric Measures

Symbol	When You Know	Multiply by	To Find	Symbol
		LENGTH		
in	inches	*2.5	centimeters	cm
ft	feet	30	centimeters	cm
yd	yards	0.9	meters	m
mi	miles	1.6	kilometers	km
		AREA		
in²	square inches	6.5	square centimeters	cm²
ft²	square feet	0.09	square meters	m²
yd²	square yards	0.8	square meters	m²
mi²	square miles	2.6	square kilometers	km²
	acres	0.4	hectares	ha
		MASS (weight)		
oz	ounces	28	grams	g
lb	pounds	0.45	kilograms	kg
	short tons (2000 lb)	0.9	tonnes	t
		VOLUME		
tsp	teaspoons	5	milliliters	ml
Tbsp	tablespoons	15	milliliters	ml
fl oz	fluid ounces	30	milliliters	ml
c	cups	0.24	liters	l
pt	pints	0.47	liters	l
qt	quarts	0.95	liters	l
gal	gallons	3.8	liters	l
ft³	cubic feet	0.03	cubic meters	m³
yd³	cubic yards	0.76	cubic meters	m³
		TEMPERATURE (exact)		
°F	Fahrenheit temperature	5/9 (after subtracting 32)	Celsius temperature	°C

*1 in = 2.54 (exactly). For other exact conversions and more detailed tables, see NBS Misc. Publ. 286. Units of Weights and Measures, Price $2.25, SD Catalog No. C13.10:286.

Approximate Conversions from Metric Measures

Symbol	When You Know	Multiply by	To Find	Symbol
		LENGTH		
mm	millimeters	0.04	inches	in
cm	centimeters	0.4	inches	in
m	meters	3.3	feet	ft
m	meters	1.1	yards	yd
km	kilometers	0.6	miles	mi
		AREA		
cm²	square centimeters	0.16	square inches	in²
m²	square meters	1.2	square yards	yd²
km²	square kilometers	0.4	square miles	mi²
ha	hectares (10,000 m²)	2.5	acres	
		MASS (weight)		
g	grams	0.035	ounces	oz
kg	kilograms	2.2	pounds	lb
t	tonnes (1000 kg)	1.1	short tons	
		VOLUME		
ml	milliliters	0.03	fluid ounces	fl oz
l	liters	2.1	pints	pt
l	liters	1.06	quarts	qt
l	liters	0.26	gallons	gal
m³	cubic meters	35	cubic feet	ft³
m³	cubic meters	1.3	cubic yards	yd³
		TEMPERATURE (exact)		
°C	Celsius temperature	9/5 (then add 32)	Fahrenheit temperature	°F

TABLE OF CONTENTS

TABLE OF CONTENTS (Continued)

LIST OF FIGURES

LIST OF TABLES

1.   INTRODUCTION

1.1   BACKGROUND

Omega Navigation System signals have the advantage of long range when compared to other terrestrial-based radionavigation systems. Because of their long range, Omega signals propagating between the earth and the ionosphere encounter many different perturbing effects. These effects are due to ground conductivity (which varies over the earth by over five orders of magnitude), the earth's magnetic field, conductivity of the ionosphere which changes with time. and direction of signal propagation. Because of the associated variations in signal phase caused by these effects, acceptable Omega navigation accuracy is achieved only if the signal is *corrected*, i.e., use of *a priori* knowledge and compensation for these effects. Such *a priori* knowledge, or prediction, is possible (though not simple) if the signal, as a function of distance and time, is sufficiently well-behaved. In the context of the most commonly-used signal propagation model (the waveguide-mode model), "sufficiently well-behaved" means the signal is primarily composed of a single "mode" (specifically, Mode 1 ; see Chapter 3 for further discussion of signal modes). For those regions/times in which the propagated Omega signal comprises multiple modes (of roughly equal strength) or is dominated by a single higher-order mode, usable prediction of the signal phase is simply not possible, due both to the theoretical complexity and the inherent signal instability under such conditions. Stated another way, the phase of an Omega signal in the "far field" (i.e., greater than about 1000 km from the transmitting source) varies approximately in a linear fashion with distance from the transmitting source. Small departures from this linear behavior (i.e., Mode 1 conditions) can be predicted but large, rapid variations and sudden shifts (due to the presence of higher-order modes) cannot be predicted.

Omega propagation corrections (PPCs) are predicted phase values which, when applied to the received Omega signal phase measurement, provide a "nominal" linear phase versus distance relationship. The nominal "value" is simply the ratio of the cumulative "idealized" phase developed by a signal to the distance over which the signal is propagated (in general, this ratio is called the wave number). The numerical value of the nominal is not critical; it is only important that the value be "near" the average over all time and space conditions. The central problem in developing Omega PPCs, then, is to calculate the *variation* of Omega signal phase

relative to a reference, i.e., the nominal phase. Since a number of geophysical parameters are involved, the model for phase variation is conveniently partitioned into *sub-models* which are either time-dependent (temporal) or space-dependent (spatial). The principal temporal sub-model is the diurnal sub-model which mainly treats the solar zenith angle dependence of the phase variation. The spatial sub-models describe effects due to: geomagnetic bearing/latitude, ground conductivity, auroral zone, and polar region. Each sub-model includes functional forms and associated calibration coefficients for computing the contribution to the phase variation.

The importance of Omega PPCs was recognized very early in the System's history. J.A. Pierce was the first to propose simple corrections based on day/night considerations (Ref 1). The Naval Electronics Laboratory (now known as Naval Ocean Systems Center (NOSC)) began an extensive theoretical and experimental investigation of Omega signal propagation prediction in the 1960's which laid the groundwork for a semi-empirical Omega phase prediction model. E.R. Swanson of NOSC led the development effort which resulted in the current Omega PPC model structure (Ref. 2). A model based on path segmentation and waveguide-mode theory was available in the late 1960's but the first widely disseminated documentation of the model appeared in 1974 (Ref. 3) when the U.S. Coast Guard took over responsibility for Omega engineering, operations, and user support. In 1980, a major re-calibration of the 1974 PPC model structure was undertaken using three-frequency data acquired from a global distribution of monitor sites (Ref. 4). The only change to the model structure was the addition of a long-term time contribution to the phase variation. This addition was based on the assumption that the ionosphere is "hardening" (increased ionization) by a fixed percentage increase each year, thus leading to a long-term exponential increase in phase variation. The validity of this assumption is the subject of a separate investigation and is not addressed in this report.

The PPCs based on the 1980 PPC model calibration showed a significant improvement over those of the 1974 model. However, subsequent usage and experimentation revealed some shortcomings in addition to those which may be due to the predicted long-term variation. Most of the reported large prediction errors (Ref. 5) occur when the signal path is in transition, i.e. a sunrise/sunset terminator lies between the transmitter and receiver. On that portion of the path near the terminator, the current diurnal sub-model predicts phase variations from anomalous injections ("dumps") of electrons into the ionosphere and a "dynamic" contribution based on an incorrect characterization of D-region dynamics. In addition, transition errors may be due to the absence of transition data in the model's calibration database. Large phase prediction errors

1-2

have also been detected on day and night transequatorial paths (Ref. 5). These large errors may indicate the need for a separate sub-model invoked in the equatorial region or could, perhaps, be explained as an improperly modeled feature within the geomagnetic bearing/latitude sub-model. Similarly, large observed errors over the higher latitude regions (Ref. 6) could indicate the need for revision of the polar/auroral sub-models or may be due to the unmodeled coupling between ground conductivity and geomagnetic field direction (with respect to the direction of signal propagation). These observed errors and possible model deficiencies point to the need for a revision of the model structure.

1.2 OBJECTIVE/APPROACH

The objective of the effort addressed in this report is to formulate a new semi-empirical PPC model structure which retains the advantages of the current model structure and remedies the apparent deficiencies identified in Section 1.1. The new model structure should conform to current geophysical/wave propagation models as much as possible yet not be overburdened with complex, detailed calculations. Being semi-empirical in form, the model should be data-driven as much as possible, especially in the calculation of those parameters to which the phase prediction accuracy is especially sensitive. Therefore, the functional forms comprising each sub-model should be as few as possible (yet retaining essential characteristic behavior), simple in form, and independent/uncorrelated. The sub-models should be appropriately combined or coupled, and be consistent with physical models and observed data. Finally, the model should be structured to permit calibration with phase data recorded on paths at all times.

The new model structure should include sub-models for characterizing:

1) Time-dependent ionospheric parameters
2) Vector geomagnetic field
3) Direction of signal propagation

and other geophysical quantities, if significantly coupled to the three parameters above. Revision of the current sub-models characterizing the phase variation in the polar/auroral zones as well as long-term phase variation are not addressed in this report.

1.3 Report Overview

Presentation of the new model structure is organized to first address the development of each sub-model separately and then address the integration of the sub-models into an overall

structure. This presentation structure is employed because the composition of each sub-model involves specific/unique concepts.

Chapter 2 presents the diurnal sub-model which includes models of the daytime and nighttime phase variation. Parameters defining the important day/night time "boundary" are presented and the predicted boundary times are compared with observed data. Since this chapter presents phase variation forms which are substantially different from those of the current (1980) model, the development of these new functional forms is presented in some depth. Consequently, in order to provide the basis for understanding the origins and rationale for the new functional forms, Chapter 2 includes a brief review of the relevant principles of ionospheric physics

The single spatial sub-model, which combines geomagnetic field, wave propagation direction, and ground conductivity effects is presented in Chapter 3. The integration of these geophysical quantities into one sub-model reflects the parameter coupling implied by standard wave propagation models. The chapter also presents alternative descriptions of phase behavior in a certain range of wave propagation directions near the geomagnetic equator.

Chapter 4 provides a description how the two sub-models are combined to provide the total phase variation/PPC. The temporal forms are recast as "evolution functions" which dictate the changes in the spatial functional forms with changing solar zenith angle. Model calibration is a three-step cycle: determine the calibration coefficients for daytime, nighttime, and parameters for the day/night time boundary (onset/recovery times). A method for calibrating the onset/recovery time parameters is also presented. Chapter 4 concludes with a comparison of the current (1980) and the new (1990) PPC models. The last chapter includes a summary, together with conclusions and recommendations.

The appendices include mathematical details of some of the quantitative features/processes of ionospheric dynamics needed for prediction of the phase variation. Also included as appendix material is a description of the analog data used to develop/test the new diurnal sub-model.

2.   DIURNAL SUB-MODEL

2.1   INTRODUCTION

This chapter presents tne temporai characteristics of the predicted Omega signal phase. These temporal characteristics are almost entirely manifested by changes in the ionosphere (ground conductivity and other electromagnetic properties affecting wave propagation vary little with time at Omega frequencies). Thus, a description of signal phase variation over time scales of interest to the Omega user (more than a few minutes but less than a year) must focus on the dynamics of the ionosphere in addition to the characteristics of wave propagation.

Prediction of signal phase behavior over long (>650 km) sub-ionospheric paths requires models of wave/ionosphere interaction, wave/earth-surface interaction, and wave propagation between the earth's surface and ionosphere. As noted above, the temporal component of signal phase prediction arises from the changing ionosphere and the resulting change in wave propagation characteristics. Wave propagation characteristics are assumed to follow from a waveguide-mode model in which the path between transmitter and receiver is partitioned into segments, each of which are sufficiently short so that earth's surface and ionosphere properties are constant within the segment. Each segment can be viewed as a section of an indefinitely long waveguide having the same boundary properties as the segment. The long waveguide has a characteristic phase versus distance relationship which differs from that of free space. This difference, referenced to a path segment length, is the incremental phase contributed by the path segment. The sum (over all path segments) of the incremental phase contributions is added to the total free-space phase change along the path to obtain the total predicted path phase.

At the local path segment level, the ionosphere is predominantly controlled by direct solar radiation from the point at which the sun is directly overhead to a threshold solar zenith angle (see Fig. 2.1-1(a)). This range of solar zenith angle, when referenced to a path segment, refers to an illumination condition known as *local day*. For solar zenith angles larger than the threshold value, the path segment ionosphere is controlled by ionization sources other than direct solar radiation and the path segment illumination condition is defined as *local night*.

A path is composed of numerous segments and, as a result, its illumination conditions differ from those of a single segment. *Path night* is said to occur when all path segments are in a

LOCAL DAY ⟶ ⟵ LOCAL NIGHT ⟶

0           $\pi/2$ χ_{THR} π χ

$$\left(\begin{array}{c} \text{SOLAR} \\ \text{ZENITH} \\ \text{ANGLE} \end{array} \right)$$

a) Local (Path Segment) Temporal Conditions

| PATH NIGHT (PDF = 1.0) | PATH SUNRISE (PDF DECREASES) | PATH DAY (PDF = 0.0) | PATH SUNSET (PDF INCREASES) | PATH NIGHT (PDF = 1.0) |

0 HRS $\chi = \chi_{THR}$ AT E.P.S. $\chi = \chi_{THR}$ AT W.P.S. $\chi = \chi_{THR}$ AT E.P.S. $\chi = \chi_{THR}$ AT W.P.S.   24 HRS   TIME

E.P.S. = EASTERNMOST PATH SEGMENT (OF IONOSPHERIC INTERACTION)
W.P.S. = WESTERNMOST PATH SEGMENT (OF IONOSPHERIC INTERACTION)

b) Path Temporal Conditions

Figure 2.1-1   Local (Path Segment) and Path Temporal Conditions

local night condition. The *path darkness fraction* (PDF) is the number of path segments in a local night condition divided by the total number of segments (in which the wave interacts with the ionosphere). Thus, for path night, PDF=1.0. *Path sunrise* is defined as the condition in which the PDF *decreases* in time (i.e., path segments are changing from a local night to a local day condition). *Path day* occurs when PDF=0.0, i.e., when all path segments are in a local day condition. *Path sunset* is said to occur when the PDF *increases* on the path. Figure 2.1-1 illustrates and compares local and path temporal conditions.

Once phase behavior at the local day and local night ionosphere has been established, it is critical to determine the time at which each of these conditions begins and ends. The first arrow shown (following T=0) in Fig. 2.1-1(b) indicates the time at which the threshold solar zenith angle is attained at the easternmost path segment and is known as the *sunrise onset time*. The second arrow indicates the time at which the threshold solar zenith angle is attained at the

2-2

westernmost path segment and is known as the *sunrise recovery time*. Similarly, the third arrow indicates the *sunset onset time* and the fourth arrow the *sunset recovery time*.

The importance of accurately specifying onset/recovery times is illustrated in Fig. 2.1-2. From the figure, it is clear that the phase error (difference between observed and predicted phase) during path sunrise is a monotonically increasing function of both the onset-time prediction error and the slope of the sunrise phase decrease. The relationship between phase error and onset time error is given approximately by

$$\Delta\phi_E \cong \frac{0.03 L \Delta T_o}{\Delta\Phi}$$

where L is the path length (in Mm), ΔT_o is the error in onset-time prediction (in minutes), $\Delta\Phi$ is the longitude difference between the path end-points (in degrees), and $\Delta\phi_E$ is the resulting phase prediction error (in cycles). For a given onset-time prediction error, the phase error is seen to be larger for longer paths and those that are more north-south oriented ($\Delta\Phi$ smaller).
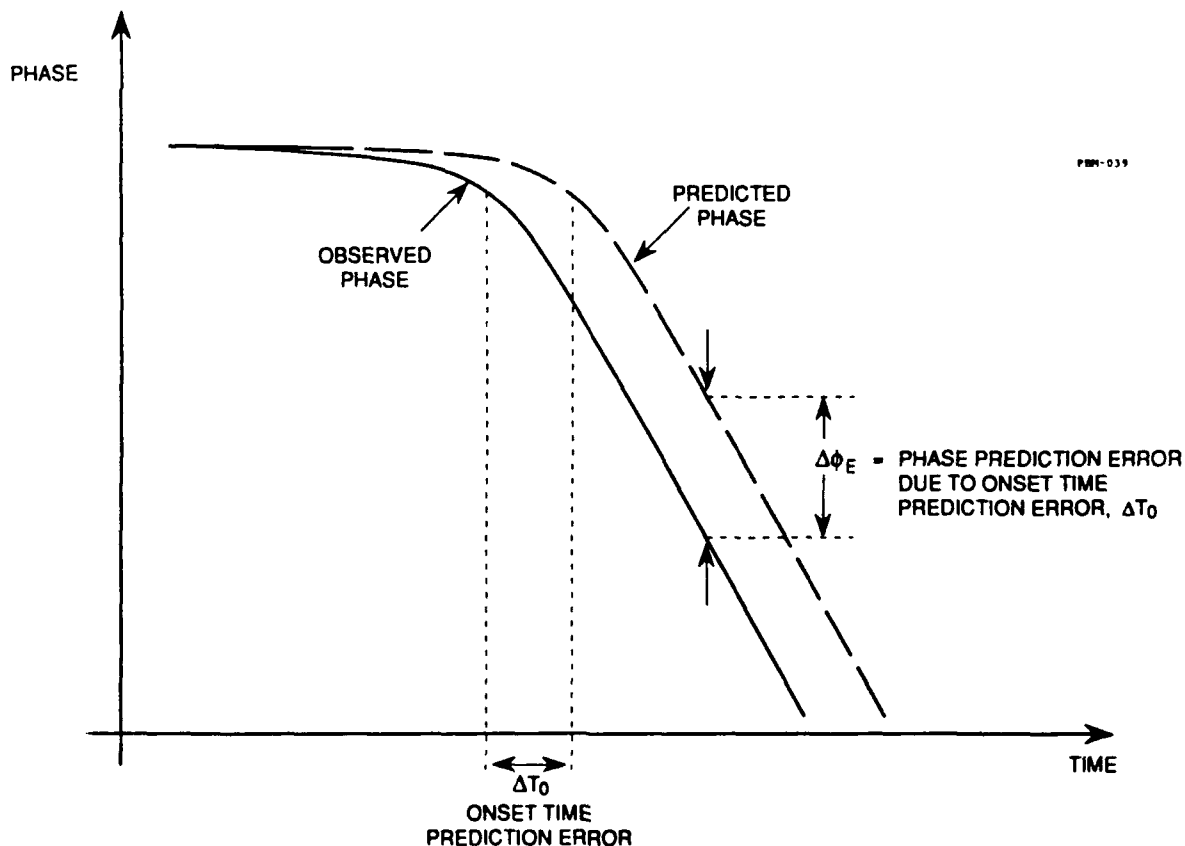
Figure 2.1-2 Phase Prediction Error due to Onset Time Prediction Error

2-3

This chapter is organized to address the three most important aspects of diurnal phase predication noted above:

- Signal phase perturbations due to a local daytime ionosphere
- Signal phase perturbations due to a local nighttime ionosphere
- Parameters describing path sunrise/sunset onset/recovery times

Since the description of phase behavior under daytime/nighttime ionosphere requires some familiarity with the dynamics and morphology of the lower ionosphere, the chapter begins with a brief background in ionospheric physics.

2.2 BACKGROUND: IONOSPHERIC PHYSICS

2.2.1 Ionospheric Dynamics

In simplest terms, the ionosphere is that portion of the upper atmosphere (above about 70 km) in which a small but important component of the particle population consists of charged particles whose numbers are maintained as a result of the competing forces of solar photoionization and reconstitution into neutral atoms/molecules as a result of various mechanisms. For a given particle species, this balance is described by a *continuity* equation which states that (for a given volume):

Rate of change of charged particle number = (charged particle production rate) —
(charged particle loss rate)

The types of charged particles found in the ionosphere include electrons, negative ions and positive ions. The specific components which are ionized in the lower ionosphere are mainly atomic/molecular forms of nitrogen, oxygen, and nitric oxide.

In tracing the balance of positive ions (other species give similar results), it is seen that positive ions are lost when combined with electrons or negative ions. The rate of loss is proportional to both the positive ion density and the combining species density. Thus, the continuity equation becomes (Ref. 7)

$$\frac{dN_+}{dt} = q - a_e N_+ N_e - a_i N_+ N_- \qquad (2.2\text{-}1)$$

where N_+ is the positive ion density, N_e is the electron density, N_- is the negative ion density, q is the production function, a_e is the electron-positive ion recombination coefficient, a_i is the

positive ion-negative ion recombination coefficient, and t is the time. Since charge neutrality holds for time scales of minutes throughout the ionosphere,

$$N_+ = N_- + N_e = (1 + \lambda)N_e \qquad (2.2\text{-}2)$$

where $\lambda = N_-/N_e$ is the negative ion ratio. Since λ is practically independent of time, substitution of Eq. 2.2-2 into Eq. 2.2-1 yields

$$\frac{dN_e}{dt} = q' - a'_E N_e^2 \qquad (2.2\text{-}3)$$

where $q' = q/(1 + \lambda)$ and $a_E' = a_e + \lambda a_i$ is known as the effective recombination coefficient. Equation 2.2-3 can be solved analytically for very simple forms of q'; otherwise approximation methods or numerical integration must be employed.

2.2.2 Wave Reflection Height

The lower ionosphere is frequently defined as a "weakly ionized plasma" which means that it does not consist *entirely* of charged particles. In fact only a small (but important) fraction of the particles in the lower ionosphere is charged. If the charged particles of the ionospheric plasma are separated and then released, the plasma oscillates at a frequency known as the *plasma frequency*. No electromagnetic wave with a frequency less than the plasma frequency can propagate through the plasma (without losing energy to the particles) since longer wave periods impart larger spatial amplitudes to the particles which drives them out of their equilibrium states. For a plasma of electrons and positive ions, the plasma frequency (MKS units) is given by

$$\omega_p = \sqrt{\frac{N_e e^2}{m \epsilon_0}}$$

where N_e is the electron density, e is the electron change, m is the mass of the electron and ϵ_0 is the permittivity of free space.

Thus, an electromagnetic wave of frequency ω will propagate through regions of the ionosphere for which

$$N_e < \frac{m \epsilon_0 \omega^2}{e^2}$$

The electron density generally increases with height since fewer electron-ion collisions occur at higher altitudes (where total particle density is smaller) and thus electron loss due to

recombination is less frequent. Hence, an electromagnetic wave of frequency ω generated at the ground travels upward until it encounters an ionospheric layer with electron density

$$N_c = \frac{m\epsilon_0\omega^2}{e^2} \qquad (2.2\text{-}4)$$

whereupon it is reflected back to the ground.

At Omega frequencies ($\sim 10^4$ Hz), the critical electron density (~ 1 electron/cm^3) given by Eq. 2.2-4 occurs at an altitude of 50-60 km. It is important to recognize that this is not a sharply defined reflection boundary. A closer analysis reveals that, at the altitude of the critical electron density, the wave front begins to turn from its upward direction, propagate horizontally, and eventually returns to earth. Thus, the wave actually scatters through the ionosphere, though it may appear to a ground observer that the wave is nearly reflected from a sharply-defined surface at a somewhat higher altitude than that given by Eq. 2.2-4. This altitude is called the effective reflection height and varies from about 70-75 km (day, sun directly overhead) to about 85-90 km (night, at antisolar point).

2.2.3 Photoionization/Chapman Model

In descriptions of the atmosphere/ionosphere, a length scale is established to describe approximate distances over which various processes occur. For example, if the atmosphere is approximated as an ideal gas, then the pressure (P) and temperature (T) are related by

$$P = nkT$$

where n is the neutral particle number density and k is Boltzmann's constant. The pressure of a column of gas of height H and mass density ϱ in the (local) earth's gravitational field (described by the gravitational constant, g) is

$$P = \varrho g H$$

where $\varrho = mn$ and m is the average mass of the neutral particles. Equating these two expressions for the pressure gives an expression for H, viz

$$H = \frac{kT}{mg} \equiv H_{sc}$$

which is known as the *scale height*.

2-6

Solar radiation (photons) striking the earth's atmosphere loses some or all of its energy when it ionizes neutral particles. This *absorption* of solar radiation may also occur without ionization (particle is raised to an excited state). A measure of absorption/attenuation of solar radiation is the *optical depth* (τ) which is given by (sun directly overhead)

$$\tau = n\sigma H_{sc}$$

where n is neutral particle density and σ is the atomic cross section for absorption (Ref. 7). The optical depth is generally a decreasing function of altitude, z (following n(z)), and the ionosphere is said to be optically thin at high altitudes and optically thick at low altitudes. It is easily shown (Ref. 7) that if I_o is the radiation flux at the top of the ionosphere, then the radiation flux at altitude z is

$$I(z) = I_o e^{-\tau(z)}$$

The *height of unit optical depth* is the height (z_o) at which the optical depth is 1, i.e. $\tau(z_o) = 1$. At this altitude, solar radiation flux is reduced to (1/e) of its incident level. This height represents a balance between the competing processes of absorption and ionization: At lower altitudes more neutral particles are available for the solar photons to ionize (usually into ion-electron pairs); however, fewer solar photons are available to ionize the neutrals due to absorption of solar photons at higher altitudes.

When the sun is not directly overhead ($\chi > 0°$), solar radiation traverses more of the ionosphere (thereby intercepting more particles) to reach the same altitude and the optical depth is increased. For $\chi \leq 70°$, the optical depth increases by a factor of approximately sec χ; for larger χ, the spherical nature of the atmospheric/ionosphere must be accounted for and the optical depth is increased by the *Chapman Function*, Ch (z,χ,H_{sc}) (see Appendix A for details). Thus the optical depth is more generally expressed (for a fixed ionizing energy) as

$$\tau(z,\chi) = n(z)\sigma H_{sc} Ch(z, \chi, H_{sc}) \qquad (2.2\text{-}5)$$

The electron production function, introduced in Section 2.2.1 may be expressed (for a fixed energy) as

$$q(z,\chi) = \frac{n(z)}{w} \sigma E_o e^{-\tau(z,\chi)} \qquad (2.2\text{-}6)$$

where w is the energy required to produce one ion-electron pair and E_o is the energy flux at the top of the ionosphere, (all other quantities have been defined earlier). Because $e^{-\tau}$ increases

and n(z) decreases with increasing altitude, the electron production is maximum at some intermediate altitude.

Based on the definitions and assumptions given above, Chapman (Ref. 8) showed that, for a fixed ionizing energy and scale height, the electron production function can be written as

$$q(z', \chi) = q_m \exp[1 - z'/H_{sc} - e^{-z'/H_{sc}} Ch(z', \chi, H_{sc})] \qquad (2.2\text{-}7)$$

where q_m is the production at height of unit optical depth and z' is the altitude referenced to the height of unit optical depth.

2.3 DAYTIME PHASE BEHAVIOR

Based on characteristics of the ionosphere described in Section 2.2 and the principles of wave propagation, a relationship is established in this section between signal phase variation and solar zenith angle. Included in the relationship are necessary (and generally well-known) ionospheric and propagation parameters.

2.3.1 Variation of Reflection Height

In Section 2.2, the Chapman electron production function is presented (Eq. 2.2-7) in terms of a reduced height (relative to the height of unit optical depth). Eq. 2.2-7 may be rewritten as

$$\log_e(q/q_m) = 1 - z'/H_{sc} - e^{-z'/H_{sc}} Ch(z', \chi, H_{sc}) = F(q(z', x))$$

The function F is a monotonically increasing function of q; thus its maximum corresponds to q's maximum. The maximum F (over altitude) is easily shown to occur (ignoring the weak dependence of the Chapman function on z') when

$$z' = H_{sc} \log_e Ch(z', \chi, H_{sc}) = z - z_0 \qquad (2.3\text{-}1)$$

where z_0 is the height of unit optical depth.

For those situations in which the electron density changes comparatively slowly over time, $dN_e/dt \sim 0$ and Eq. 2.2-3 becomes $(\lambda \sim 0)$

$$q = a_e N_e^2$$

In this case, the altitudes for maximum electron production and electron density coincide. Even when dN_e/dt cannot be neglected, the altitudes of the corresponding maxima do not differ significantly in the lower ionosphere.

Thus, Eq. 2.3-1 essentially describes the variation of the peak electron density altitude referenced to the height of unit optical depth. Although the effective reflection height of a wave in the 10-14 kHz range may not be the same as the altitude of the peak electron density, the *variation* of the two defined altitudes with solar zenith angle is expected to be the same (Ref. 7). Hence the variation in reflection height, Δh, due to changing solar zenith angle behaves as

$$\Delta h \;\propto\; H_{sc} \log_e Ch(z', \chi, H_{sc}) \tag{2.3-2}$$

which emphasizes the fact that the variation, Δh, is not *equal* to the variation expressed in Eq. 2.3-1 but rather that *behavior* with changing solar zenith angle is the same.

2.3.2 Phase Change Due to Variation in Reflection Height

Because an electromagnetic wave at 10 kHz has a wavelength nearly equal to 1/2 the distance from the earth's surface (where the wave reflects) to the ionospheric region where the wave scatters/returns (-70 km in day), the signal cannot be treated as a "ray" using geometrical optics. For long-wavelength signals, two descriptions of signal propagation are generally used, depending upon the application. The *wavehop* model (Ref. 14) treats the signal received at a point between the earth's surface and ionosphere as a sum of wave "hops", each of which is a distinct integral number of reflections from the earth/ionosphere. The *waveguide-mode* model (Ref. 15) treats the earth's surface and ionosphere as waveguide boundaries (the "earth-ionosphere (EI) waveguide") and the signals generated and propagated inside it are considered to be formed from a series of "modes" characteristic of the waveguide. The latter wave propagation model has been developed extensively (Ref. 12) and is the basis for most of the semi-empirical modeling described in this report.

Both the wavehop and the waveguide-mode models lead to an approximate, linear relationship between signal phase variation ($\Delta\phi$) on signal paths within the EI waveguide and variation of effective reflection height (Δh) with solar zenith angle. A straightforward development (Ref. 17) yields

$$\Delta\phi = \frac{L}{\lambda}\left(\frac{1}{2R_E} + \frac{\lambda^2}{16z^3}\right)\Delta h \qquad (2.3\text{-}3)$$

where L is the path length, λ is the signal wavelength, z is nominal reflection height, and R_E is the mean earth radius. In day, z=70 km so that (with R_E = 6367 km)

$$\Delta\phi = \frac{L}{\lambda}(7.853 \times 10^{-5} + 1.823 \times 10^{-7}\lambda^2)\Delta h \qquad (2.3\text{-}4)$$

where all length quantities are in kilometers and $\Delta\phi$ in cycles. For a 1 Mm path and a frequency of 10 kHz, the above reduces to

$$\Delta\phi = 8.084 \times 10^{-3} \ \Delta h$$

The nominal day-to-night difference in effective reflection height is about 15 km so that

$$\Delta\phi_{\text{DAY}\rightarrow\text{NIGHT}} \cong 12 \ \text{cec/Mm} \qquad (10\text{kHz})$$

where 1 cec $\equiv$ 0.01 cycle. This corresponds approximately to the diurnal shift observed in Omega phase data recordings (Appendix B).

Substituting Eq. 2.3-2 into Eq. 2.3-3 yields

$$\Delta\phi = C_D\frac{L}{\lambda}(1 + 2.321 \times 10^{-3}\lambda^2)H_{sc}\log_e \text{Ch}(z', \chi, H_{sc}) \qquad (2.3\text{-}5)$$

where all lengths are in kilometers and a factor of 7.853×10^{-5} is taken out of Eq. 2.3-4 and absorbed into the unknown constant C_D which represents the proportionality constant implied by Eq. 2.3-2. Note that the phase variation depends upon

- frequency (through the wavelength, λ)
- solar zenith angle
- scale height
- path length.

The scale height used for most atmospheric models (Ref. 9) is about 5-6 km for altitudes ranging from 70 to 90 km. A default of H_{sc} = 5 km is recommended although the value can be

changed if so demanded by the observed phase data. The value of the constant C_D is to be determined by the data as discussed in Chapter 4. The functional behavior of $\Delta\phi$ as a function of χ given by Eq. 2.3-5 is in general agreement with the observed data (Appendix B).

2.4 NIGHTTIME PHASE BEHAVIOR

Since solar radiation is not directly responsible for maintenance of the ionosphere at night, the development in this section does not strictly follow the classical Chapman model described in Section 2.2. The basic result follows from semi-quantitative arguments and observational data.

2.4.1 Variation of Reflection Height

At night, direct solar photoionization is absent and the ionospheric profile (electron density vs height) changes markedly. The D-region effectively disappears at night primarily due to a lack of strong x-ray and extreme ultraviolet (EUV) sources. Thus VLF waves are scattered through the lower E-region (85-90 km) which is maintained by:

- Cosmic rays
- Galactic radiation (x-ray stars, etc)
- Scattered solar radiation.

Of these three sources, the most important is the scattered solar radiation which consists of three principal types (Ref. 9): (1) Lyman-α, (2) Lyman-β, and (3) He II. In the lower E-region, Lyman-α fluxes predominate over the other sources. Lyman-α (the primary transition between the first two orbitals of hydrogen) is produced in immense quantities by the sun but it has a relatively long wavelength (1216 $\overset{\circ}{A}$)/low energy so it does not normally penetrate the lower ionosphere even on the dayside. However, nitric oxide in the ionosphere is very efficiently ionized by Lyman-α photons so that even small fluxes contribute to D/E-region ionization. Lyman-α radiation also passes through the earth's geocorona and resonantly scatters from the large local population of hydrogen atoms/ions. This scattering is relatively efficient and can produce significant fluxes of Lyman-α radiation incident on the nightside ionosphere (Ref. 9). Satellite measurements of this radiation (Ref. 10) show a distinct solar zenith angle dependence $(0 < \chi < \pi)$. Figure 2.4-1 shows the Lyman-α radiation received at a near-zenith angle from
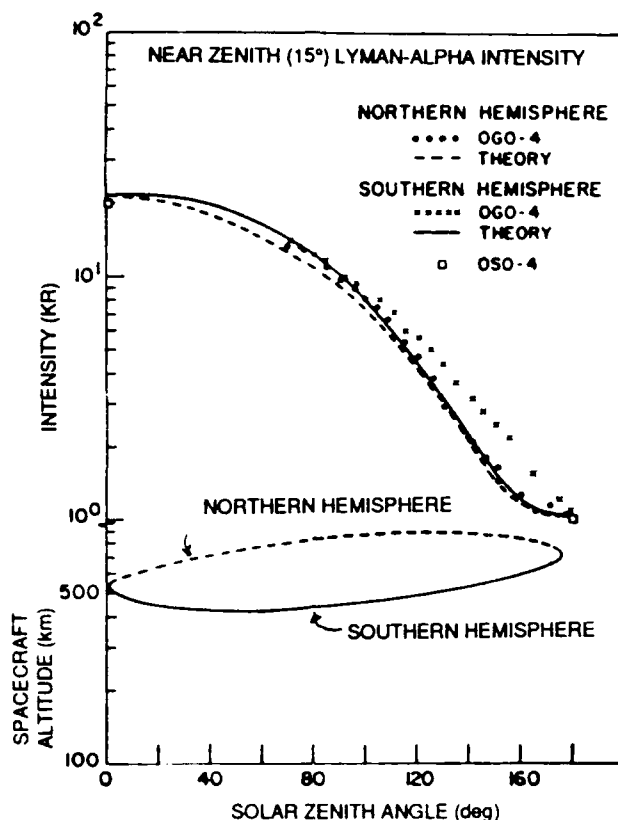
Figure 2.4-1 Theoretical and Experimental Near-zenith Lyman-alpha Intensity as a Function of Solar Zenith Angle (from Ref. 10)

the satellite. This behavior, together with the nadir intensity behavior (see Ref. 10) indicates an approximate cosine-type functional dependence on solar zenith angle.

If the Lyman-α radiation actually controls the nighttime effective reflection height, then the observed signal phase should reflect this behavior during the nighttime measurement period (phase should peak when the average solar zenith angle on a path is maximum). If no effective source of nighttime ionization is present but the recombination processes are very slow, the phase should gradually rise during the time the ionosphere controlling the signal path is fully dark. The observed data (Appendix B) frequently shows a slight peak during the nighttime portions indicating a solar zenith angle dependence.

In order to derive a quantitative relationship between Lyman-α flux and solar zenith angle, first assume that the effective flux is incident normal to the nighttime ionosphere (i.e., radially inward at any point on the nightside). This corresponds to $\chi = 0$ in the Chapman formalism and Eq. 2.2-7 may be written

$$q(z',0) = q_m \exp\left[1 - z'/H_{sc} - e^{-z'/H_{sc}}\right] \qquad (2.4\text{-}1)$$

since $Ch(z,0,H_{sc}) = \sec(0) = 1$. As noted earlier, q_m is the electron production relative to the height of unit optical depth (z_0), i.e., $q_m = q(z' = 0,0)$ where $z' = z - z_0$. Using Eqs. 2.2-5 and 2.2-6, q_m may be written ($\chi = 0$)

$$q_m = \left.\frac{\tau E_0 e^{-\tau}}{wH_{sc}}\right|_{\tau = 1} = \frac{E_0}{ewH_{sc}}$$

Since w is the minimum energy required to create an ion-electron pair, E_0/w is just the ionizing efficiency (η) times the incident photon flux (I_0) at the top of the ionosphere. Thus

$$q_m = \frac{\eta I_0}{eH_{sc}} \tag{2.4-2}$$

This differs from the solar Chapman model in that the radiation is normally incident but the external flux (or intensity) I_0 is a function of solar zenith angle.

Further assume that the ionosphere is approximately in equilibrium so that Eq. 2.2-3 becomes (with $\lambda = 0$)

$$q = \alpha_e N_e^2$$

which, when combined with Eqs. 2.4-1, 2.4-2 yields

$$\alpha_e N_e^2 = \frac{\eta I_0(\chi)}{H_{sc}} \exp\left[-z'/H_{sc} - e^{-z'/H_{sc}}\right] \tag{2.4-3}$$

The reasonable assumption is now made that wave reflection occurs at a fixed value of electron density, N_e (i.e., a fixed plasma frequency; see Eq. 2.2-4). Thus, in Eq. 2.4-3, only the reduced height z' changes in response to the solar zenith angle-dependent intensity I_0. Since the height of unit optical depth for Lyman-a radiation is 75 km (Ref. 9) and the nighttime reflection height is 80-90 km,

$$1 \leq z'/H_{sc} \leq 3$$

and the exponential term inside the brackets in Eq. 2.4-3 may reasonably be neglected in comparison to the linear term. Thus, Eq. 2.4-3 becomes

$$e^{z'/H_{sc}}\alpha_e N_e^2 = \frac{\eta I_0(\chi)}{H_{sc}}$$

2-13

or

$$z' = H_{sc} \log_e I_0(\chi) + \text{(terms independent of } \chi) \qquad (2.4\text{-}4)$$

Recall that the satellite observations (see Fig. 2.4-1) showed that the logarithm of Lyman-α radiation intensity has a cosine-type dependence on solar zenith angle. This fact, coupled with Eq. 2.4-4 implies that $z' = z - z_0$ depends linearly on $\cos\chi$ and hence it follows that

$$\Delta h = A \cos\chi + B \qquad (2.4\text{-}5)$$

where it is assumed, that the variation in altitude of the ionospheric level having constant electron density (critical value for reflection of 10-14 kHz waves) referenced to the height of unit optical depth is the same as the variation in reflection height. In Eq. 2.4-5, A and B are constants to be determined from the observed phase data and by matching phase at the day/night boundary.

2.4.2 Phase Change Due to Variation in Reflection Height

The signal phase variation due to the reflection height change given by Eq. 2.4-5 is obtained from the general form, Eq. 2.3-3. Thus, with z = 87 km for the nominal nighttime ionospheric reflection height,

$$\Delta\phi = \frac{L}{\lambda} (1 + 1.209 \times 10^{-3}\lambda^2)(A \cos\chi + B) \qquad (2.4\text{-}6)$$

Note that the coefficient A must be negative since the phase increases as the reflection height increases and thus as the solar zenith angle increases from $\pi/2$ to π .

2.5 ONSET/RECOVERY TIME PARAMETERS

The two previous sections addressed phase behavior as a function of solar zenith angle for local daytime and nighttime ionospheric conditions. Accurate specification of the solar zenith angle "boundary" between these two temporal domains is important for phase prediction accuracy as illustrated in Fig. 2.1-2. Clearly, a scheme which predicts the correct shape of a diurnal phase trace but is displaced by 20-30 cec due to an onset time prediction error is not a useful predictor.

2.5.1 Definition of Onset/Recovery Time Parameters

Sunrise/sunset onset/recovery times refer to the phase behavior along an entire signal path defined by a transmitting source at one end and a receiver at the other end. Since results from the waveguide-mode model are used for the spatial sub-models, the signal path along the two-dimensional EI waveguide is broken into path segments (see Fig. 2.5-1). Within each of these 0.01-radian segments, the path spatial properties are assumed constant and the waveguide is homogeneous. Thus, local ionospheric properties are defined at the segment level and path characteristics reflect the collective segment level properties.

A local, daytime ionosphere is defined as one whose ionization processes are solar-controlled. Clearly, solar radiation controls the ionization of the D-region for $0 \leq \chi \leq \pi/2$. For $\chi \geq \pi/2$, solar radiation must pass through lower altitudes and re-emerge at the desired altitude (see Fig. 2.5-2). This property, which is embodied in the appropriate approximations to the Chapman function, means that the rate of attenuation of solar radiation (due to changing solar zenith angle) becomes very rapid. Solar photoionization is still expected to dominate other sources until the radiation "beam" incident upon the 75-85 km ionospheric layer (from below)
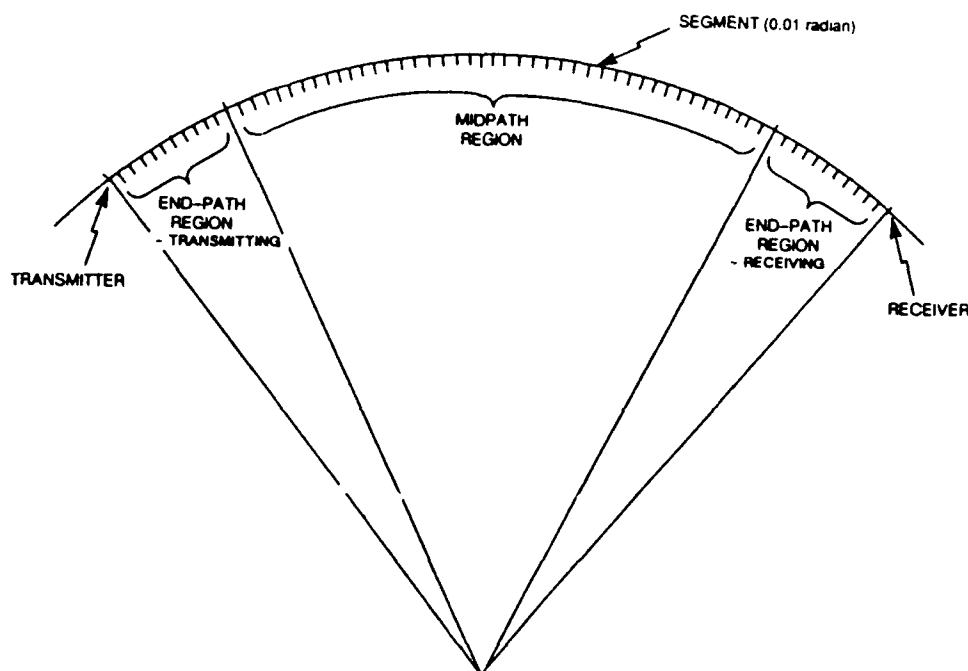
Figure 2.5-1 Segmentation of the Signal Path

attains an enroute minimum of about 50 km. At this point the concentration of ozone which efficiently absorbs EUV radiation becomes substantial and ionization due to solar radiation effectively ceases. The solar zenith angle corresponding to this condition is called the threshold solar zenith angle (χ_{THR}) and, for a nighttime reflection height of about 85 km, is approximately 96° (see Fig. 2.5-2).

Ionization does not occur immediately after radiation is incident upon a region of neutral constituents. Solutions of the continuity equation, Eq. 2.2-3, for an impulse-type electron production function show that the electron density "impulse" follows the impulsive production by a time interval, τ, given by

$$\tau = \frac{1}{2a_E'N_e} = \frac{1}{2\sqrt{a_E'q'}} = \text{ionospheric response time}$$

In the E-region the recombination coefficient is given as 10^{-7} cm^3/sec (Ref. 13). When used with D-region electron densities, however, this numerical value of a_E' yields an unacceptably large

Ozone layer cutoff $\cong$ 50 km

Reflection height $\cong$ 85 km

Threshold solar zenith angle (χ_{THR}) $\cong$ 96°

Figure 2.5-2 Illustration of the Threshold Solar Zenith Angle which Separates Day and Night for the Lower Ionosphere
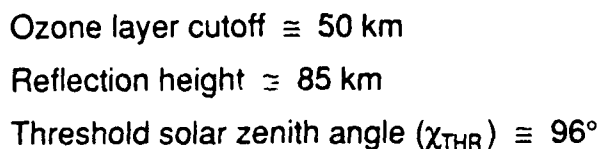
value of τ. Observational data (Ref. 11) suggests ionospheric response times of about 1/8 hour (day) and 1.13 hours (night). Fig. 2.5-3 illustrates the determination of ionospheric response time.

In determining the onset/recovery of daytime or nighttime conditions along a signal *path*, the interaction of the wave with the ionosphere must be considered in addition to the ionospheric changes. Since the wave interacts with the ionosphere over a substantial fraction of the path, it is important to know the point on the path at which the first effective path/ionosphere interaction takes place.

An Omega antenna can be modeled as monopole source which radiates energy outward and upward from its location on the earth's surface. The steeply launched portions of the transmitted wave interact first with the ionosphere but are reflected between the earth's surface and ionosphere before traveling outward to any appreciable distance. Those portions of the

D-Region Balance Equation

$$\frac{dN_e}{dt} = q - \alpha N_e^2$$

N_e = Electron density

q = Electron production

α = Recombination coefficient

Early Experimental Results Indicated

$\tau_D \cong 6$ minutes (day)

$\tau_N \cong 66$ minutes (night)

Response Time (τ) = $\dfrac{1}{2\alpha N_e}$ = $\dfrac{1}{2\sqrt{\alpha q}}$
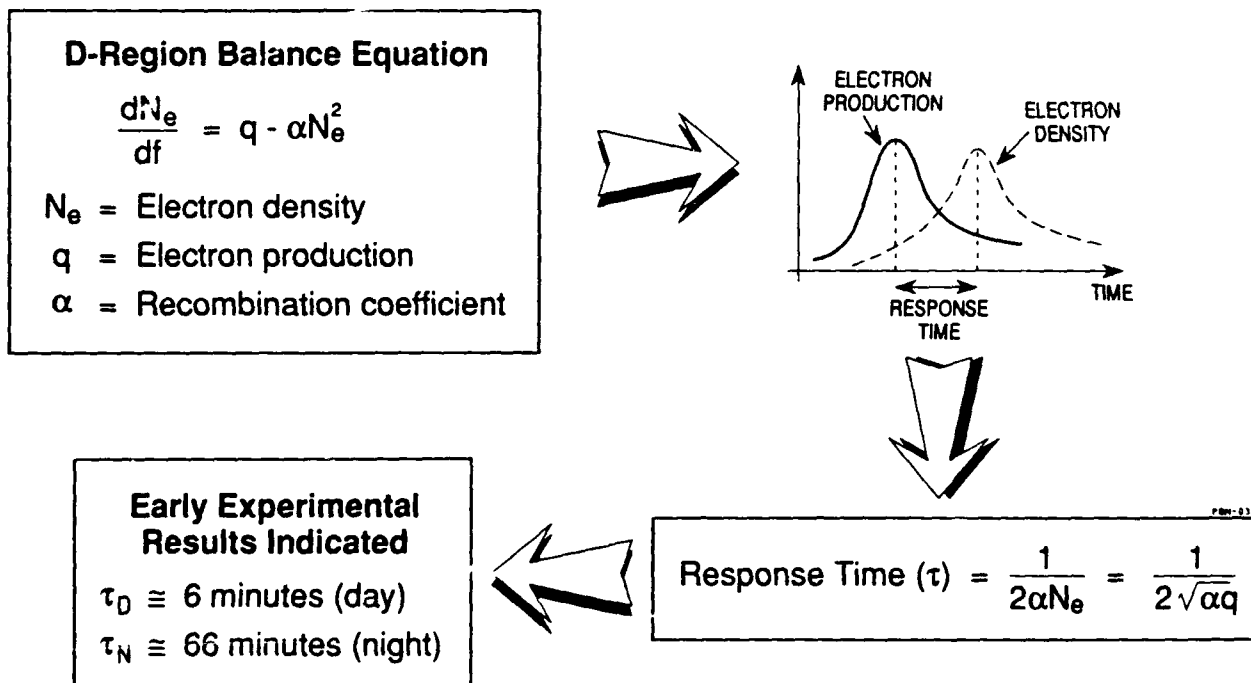
Figure 2.5-3 Origin of the Day/Night Ionospheric Response Time

transmitted wave which are launched nearly tangentially to the earth's surface travel farthest outward before interacting with the ionosphere. Because of its relatively low attenuation, this wave structure generally dominates all others (in signal energy) at distances (along the earth's surface) beyond the wave's first interaction with the ionosphere. The wave structure which survives in the far field is launched at an angle slightly less than 90° from the zenith which satisfies the reinforcement condition between the reflected wave and the direct wave. Satisfaction of this condition insures that the wave is an eigenmode (Mode 1) of signal propagation (at a particular Omega frequency) in the earth-ionosphere waveguide. Further discussion of these modes is given in Chapter 3.

Figure 2.5-4 illustrates the geometry of the Mode 1 wave interaction with the ionosphere. The point of first ionospheric interaction, P, is separated from the transmitting source by an internal angle, a, measured at the center of the earth. Since $R_E a >> h$, VLF signal paths are usually measured by their arc length over the earth's surface. The table in Fig. 2.5-4 indicates how a varies with ionosphere illumination and frequency. Night values are larger than day because h is greater so that the wave travels outward further before intersecting the ionosphere. Angular values are higher for 13.6 kHz than 10.2 kHz because the corresponding eigenangle is larger for the higher frequency (wavelength is smaller so mode resonance condition more closely approximates a $\psi = 90°$ launch). Because of the general reciprocity features of electromagnetic waves (reciprocity is not strictly valid due to the anisotropic magnetized ionospheric plasma), the same geometry holds for the receiving end of the path. Thus, if the transmitter in Fig. 2.5-4 is replaced by the receiver, then P becomes the *last* point of ionospheric interaction for the Mode 1 signal (angular relationships are approximately the same).

2.5.2 Numerical Testing of Sub-model Forms

Since the diurnal sub-model, by definition, contains no provision for any sources of phase variation other than the diurnal variation of effective ionospheric reflection height, comparison with observed data on paths of conventional length is not feasible, primarily because of the coupling between the diurnal and spatial sub-models. However, the onset/recovery time parameters are essentially independent of the spatial contributions to the phase prediction and thus can be tested.

Day and night functional forms presented in Sections 2.3 and 2.4 are computed at each segment (depending on solar zenith angle) and combined with the reference phase depending

ψ = Real part of Mode 1 eigenangle for frequency / illumination condition

h = Ionospheric reflection height

R_E = Radius of earth

α = Angular extent of near-field region (no ionospheric interaction with Mode 1 signal)

P = Point of first ionospheric interaction

α (radians) :

FREQ. (kHz) \ ILLUM.	DAY	NIGHT
10.2	0.081	0.131
13.6	0.104	0.157
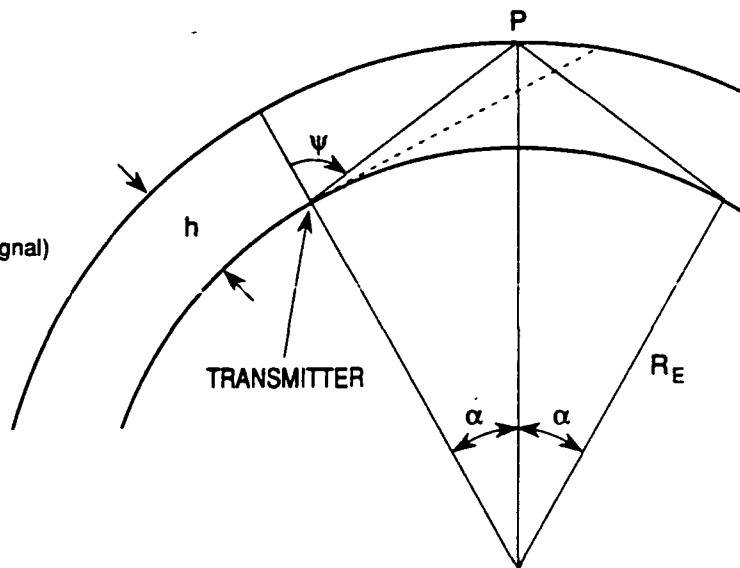
Figure 2.5-4 Schematic of Path Geometry to Illustrate Point of First Ionospheric Interaction for a Mode 1 Signal

only on path length. The path/time computer program (developed under this effort) contains path segmentation and solar position subroutines similar to those used in earlier PPC models (Ref. 3). Required inputs to the program are transmitting station, receiving site, signal frequency, and time (month/day/year). Input values are also used to identify the path segment number defining point of first/last ionospheric interaction, solar zenith angle threshold, and day/night ionospheric response times. The program computes path phase values at six-minute intervals based only on diurnal effects and reference wave number. Figure 2.5-5 shows a sample printout from the program which lists the beginnings of sunset, night, sunrise, and day (note that path sunset recovery time is the same as the beginning of path night and path sunrise recovery time is the same as the beginning of path day). Time units are in 0.1 hour (6 minutes) and the "-1", "-2" for each time domain allows for double-diurnal effects (see Appendix B). The phase data given at the bottom of the printout for each 6 minute interval is plotted in Fig. 2.5-6.

```
**** THIS IS THE DATA FOR PLOT FILE BA260988.13T  ****
BREAK POINTS:   49    62   182    190    0    0    0    0
SUNSET -1  BEGINS AT INDEX 182; MAX PHASE=  1.085    MIN PHASE=   .729
SUNSET -2  BEGINS AT INDEX   0; MAX PHASE= *******    MIN PHASE= *******
NIGHT  -1  BEGINS AT INDEX 190; MAX PHASE=  1.143    MIN PHASE=  1.085
NIGHT  -2  BEGINS AT INDEX   0; MAX PHASE= *******    MIN PHASE= *******
SUNRISE-1  BEGINS AT INDEX  49; MAX PHASE=  1.095    MIN PHASE=   .744
SUNRISE-2  BEGINS AT INDEX   0; MAX PHASE= *******    MIN PHASE= *******
DAY    -1  BEGINS AT INDEX  62; MAX PHASE=   .744    MIN PHASE=   .472
DAY    -2  BEGINS AT INDEX   0; MAX PHASE= *******    MIN PHASE= *******
TOTAL NUMBER OF DATA POINTS     =        289
TRANSMITTING STATION            =   LIBERIA
MONITORING STATION              =   NORWY
FREQUENCY                       =   13.6 kHz
DAY                             =   26
MONTH                           =   SEP
YEAR                            =   1988
SEG # FOR PT. OF 1ST INTERACT.  =        11
CHI THRESHOLD                   =    96.140000
DAY IONOSPHERIC TIME CONST.     =     6.000000 MINUTES
NIGHT IONOSPHERIC TIME CONST.   =     6.000000 MINUTES
DAY/NIGHT SCALING FACTOR        =   8.100000E-01
MAXIMUM PHSARY VALUE            =   314.143400
MINIMUM PHSARY VALUE            =   313.000000
314.143 314.143 314.143 314.143 314.143 314.143 314.143 314.142 314.142 314.142
314.141 314.141 314.140 314.140 314.139 314.139 314.138 314.137 314.136 314.136
314.135 314.134 314.133 314.132 314.131 314.130 314.129 314.127 314.126 314.125
314.124 314.122 314.121 314.120 314.118 314.117 314.115 314.114 314.112 314.111
314.109 314.108 314.106 314.104 314.103 314.101 314.099 314.097 314.095 314.090
314.083 314.072 314.060 314.042 314.023 313.998 313.972 313.938 313.902 313.856
313.801 313.744 313.685 313.648 313.619 313.601 313.586 313.575 313.565 313.558
313.551 313.545 313.539 313.535 313.531 313.526 313.523 313.520 313.517 313.514
313.511 313.509 313.506 313.504 313.502 313.500 313.498 313.496 313.495 313.493
313.491 313.490 313.488 313.487 313.486 313.485 313.484 313.483 313.482 313.481
313.480 313.479 313.478 313.478 313.477 313.476 313.476 313.475 313.475 313.474
313.474 313.473 313.473 313.473 313.472 313.472 313.472 313.472 313.472 313.472
313.472 313.472 313.472 313.472 313.472 313.472 313.472 313.472 313.473 313.473
313.473 313.473 313.474 313.474 313.475 313.475 313.476 313.477 313.477 313.478
313.479 313.480 313.480 313.481 313.482 313.483 313.484 313.485 313.487 313.488
313.489 313.491 313.492 313.494 313.495 313.497 313.499 313.501 313.503 313.505
313.508 313.510 313.513 313.515 313.519 313.522 313.525 313.529 313.533 313.538
313.543 313.549 313.555 313.563 313.572 313.583 313.595 313.611 313.630 313.656
313.690 313.729 313.777 313.824 313.881 313.933 313.991 314.036 314.073 314.085
314.087 314.089 314.091 314.093 314.095 314.096 314.098 314.100 314.102 314.103
314.105 314.107 314.108 314.110 314.111 314.113 314.115 314.116 314.117 314.119
314.121 314.122 314.123 314.124 314.126 314.127 314.128 314.129 314.130 314.131
314.133 314.133 314.134 314.135 314.136 314.137 314.138 314.139 314.139 314.140
314.140 314.141 314.141 314.142 314.142 314.143 314.143 314.143 314.143 314.143
314.143 314.143 314.143 314.143 314.143 314.143 314.143 314.142 314.142 314.142
314.141 314.141 314.140 314.140 314.139 314.139 314.138 314.137 314.136 314.136
314.135 314.134 314.133 314.132 314.131 314.130 314.129 314.127 314.126 314.125
314.124 314.122 314.121 314.120 314.118 314.117 314.115 314.114 314.112 314.111
314.109 314.108 314.106 314.104 314.103 314.101 314.099 314.097 314.095    .000
   .000    .000    .000    .000    .000    .000    .000    .000    .000    .000
```

Figure 2.5-5   Sample Printout from Path/Time Computer Program to Test
              Diurnal Sub-model Forms
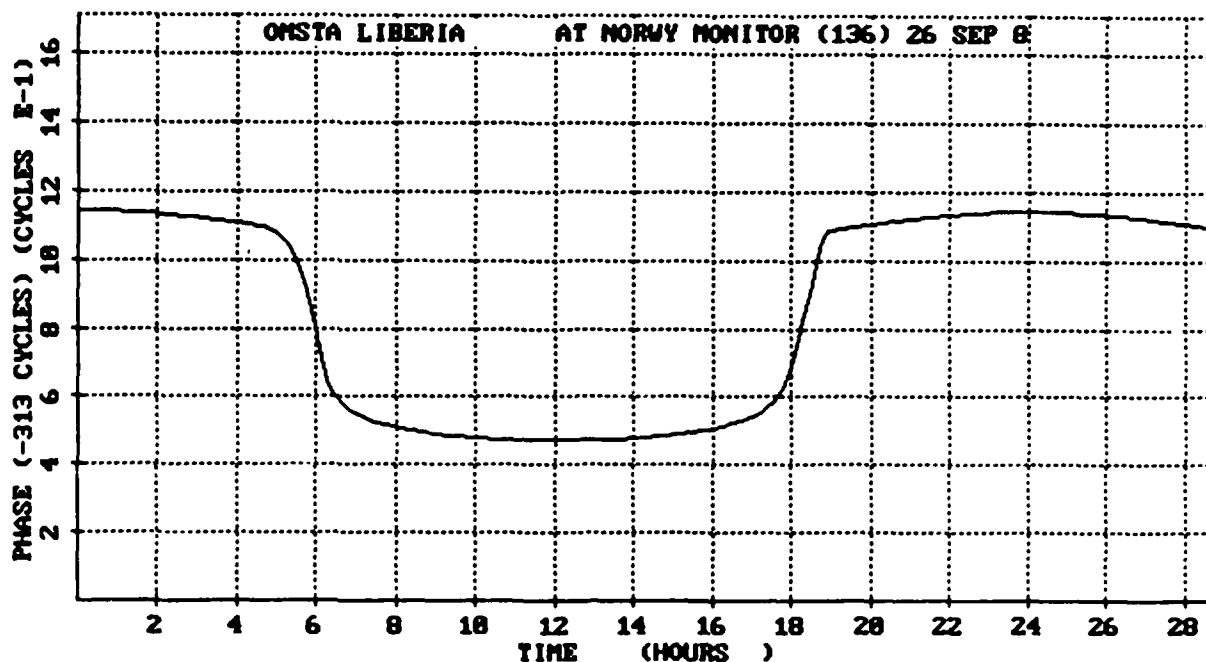
Figure 2.5-6 Plot of Diurnal Phase Prediction

It is important to recognize that the diurnal phase behavior plotted in Fig. 2.5-6 does not account for any spatial variation in phase (i.e., that due to the geomagnetic field or ground conductivity) and thus cannot be properly compared to observed data. It is shown to indicate how phase variation would appear in a spatially homogeneous world.

Comparison of predicted and observed onset/recovery times for sunrise and sunset is given in Appendix B. There it is shown that the predictions are in close agreement with the observations studied using default onset/recovery time parameters.

2.6 SUMMARY

In this chapter the specific functional behavior of the VLF signal phase with solar zenith angle is developed for two broad classes of local ionospheric conditions:

- control by direct solar radiation (day)
- control by nighttime radiation sources (night).

The daytime phase variation is based on a Chapman model of electron photoionization/absorption and numerical values indicate a qualitative agreement with observed data. The nighttime

phase variation is developed from empirical measurements of scattered Lyman-alpha flux using a method of analysis similar to Chapman's. The resulting phase variation exhibits a phase change with solar zenith angle at night — a phenomenon also detected in the observed data.

Parameters defining the path sunrise/sunset onset/recovery times are identified and a path/time computer program is written to compare the predicted times with observed data. Comparison of the predicted times using default parameters with a limited sample of observations show excellent agreement. Although eventual calibration with observed phase data will give more precise values, these results show that the default values are good estimates of the onset/recovery time parameters.

3.   GEOMAGNETIC/CONDUCTIVITY SUB-MODEL

3.1   INTRODUCTION

This chapter presents the methodology followed to develop the structure of the geomagnetic/conductivity sub-model. This sub-model is the spatial component of the overall Omega signal phase prediction model (referred to as the 1990 PPC model) described in this report. The 1990 PPC model predicts the phase of a received Omega signal (a multimode signal) by assuming the signal's Mode 1 component amplitude greatly exceeds all other component mode amplitudes.

The Mode 1 signal phase can be separated into two components:

$$\phi = \phi_1(d) + \phi_2$$

where ϕ_1 depends on path length (d) and ϕ_2 does not. The first component may be expressed as (assuming insignificant signal dispersion):

$$\phi_1(d) = k\ d = \left(\frac{f}{v}\right) d$$

where k is the wave number, f is the frequency and v is the phase velocity. For a signal of fixed frequency and signal path of fixed length, ϕ_1 thus depends on wave number or phase velocity. For this reason, ϕ_1 is called the wave number or *phase velocity* component. The component ϕ_2 is called the *excitation factor phase*. This sub-model describes the theoretical dependence of these Mode 1 signal phase components as functions of the locally-varying spatial parameters (i.e., ground conductivity, geomagnetic field in the ionosphere, and signal propagation direction) at each segment of the signal path for:

- Each of the two extreme (day and night) solar illumination conditions
- Each of three (10.2, 11 1/3, and 13.6 kHz) Omega navigational frequencies.

An overview of the Omega signal propagation mechanism/theory is given in Section 3.2. The methodology used for developing the theoretical database, from which the sub-model is

derived, is given in Section 3.3. The methodology used to develop the sub-model and the resulting sub-model structure is presented in Section 3.4. The chapter is summarized ir Section 3.5.

3.2 OMEGA SIGNAL PROPAGATION MECHANISM/THEORY

As presented in Chapter 2, Omega signals propagate in the EI waveguide, i.e., the space between the earth's surface and the D-region of the ionosphere. In this waveguide, signals radiated by a transmitting station propagate essentially along great-circle radials emanating from the station. The propagation characteristics of an Omega signal along a radial path* are functions of the electromagnetic properties of the path waveguide. The lower boundary of this waveguide is the earth's surface characterized by a spatially-varying ground conductivity (and associated permittivity). Table 3.2-1 lists the worldwide values of the earth's ground conductivity (and permittivity) at VLF/Omega signal frequencies.

The upper boundary of the EI waveguide is the D-region of the ionosphere which is anisotropic due to the vector geomagnetic field. Most VLF propagation prediction models (in particular, the waveguide-mode model (Ref.20)) assume the electron density varies exponentially with altitude in the vicinity of the reflection height, i.e.,

$$N_e(z) = N_e(z_0) \, e^{b(z-z_0)}$$

Table 3.2-1 Earth's Ground Conductivity Levels and Associated Conductivity/Permittivity Values (Ref. 19)

LEVEL	CONDUCTIVITY (mho/m)	RELATIVE PERMITTIVITY
1 (Ice Cap)	1.0×10^{-5}	10.0
2	3.2×10^{-5}	10.0
3	1.0×10^{-4}	15.0
4	3.2×10^{-4}	15.0
5	1.0×10^{-3}	15.0
6	3.2×10^{-3}	15.0
7	1.0×10^{-2}	20.0
8	3.2×10^{-2}	20.0
9	1.0×10^{-1}	45.0
10 (Seawater)	4.0	81.0

---

*"Path" refers to a two-dimensional waveguide in which one dimension is the altitude above the earth's surface and the other dimension is the arc length from the transmitting station along the surface of the earth.

where z_0 is the *effective reflection height* and b (b>0) is the electron density gradient. These models also assume that the collision frequency profile is exponential in the vicinity of the effective reflection height, i.e.,

$$\nu_e(z) = \nu_e(z_0) \ e^{-a(z-z_0)}$$

where $\nu_e(z)$ is the electron collision frequency (electron/neutral and electron/ion) and a (a>0) is the collision frequency gradient. For very low signal frequencies, the direct conductivity is defined as

$$\sigma_0(z) \approx \frac{\omega_p^2(z)}{\nu_e(z)}$$

where ω_p is the plasma frequency defined in Chapter 2.

In Section 2.2 it is shown that ω_p^2 is proportional to the electron density, $N_e(z)$. Thus the direct conductivity is proportional to $N_e(z)/\nu_e(z)$ and hence is also exponential (as a function of altitude) in the vicinity of $z - z_0$ with gradient β where

$$\beta = a + b$$

The effective reflection height, z_0, and the conductivity gradient, β, are the parameters required by waveguide-mode model calculations of signal propagation. Numerical values of these parameters are given in Table 3.2-2.

Since Omega signal path parameters vary both spatially (along the path) and temporally (at each point along a path), Omega signal paths, and hence the associated waveguides, are inhomogeneous. The waveguide-mode model transforms an inhomogeneous path waveguide into a set of homogeneous waveguides by means of the following procedure: (1) divide the inhomogeneous waveguide/path into a large number of concatenated homogeneous-property segments, (2) treat each segment as a homogeneous, infinitely long waveguide with properties corresponding to the upper and lower boundaries of the segment, and determine the allowed modes/signal

Table 3.2-2 Typical Values of Daytime and Nighttime Ionospheric Parameters

IONOSPHERE ILLUMINATION CONDITION	IONOSPHERIC REFLECTION HEIGHT (km)	IONOSPHERIC CONDUCTIVITY GRADIENT (km^{-1})
Day	70	0.3
Night	87	0.5

behavior, (3) determine mode conversion effects (scattering of the incident signal) occurring at each of the interfaces between the homogeneous segments, and (4) connect the multimode signal solutions at each segment by properly accounting for the mode conversion effects at the interfaces.

In the waveguide-mode theory, an electromagnetic signal field is expressed as a sum of the signal fields corresponding to the "characteristic" modes of the waveguide. The modes characterize the solutions of the waveguide-mode equation, which describes the allowable wave launch angles that establish reinforcement between the transmitted and reflected waves. Each mode has an associated complex eigenvalue (also referred to as an eigenangle). The eigenangle is a function of the path parameters and signal frequency. The signal parameters of a mode, i.e., the amplitude and phase, are functions of the following components:

- Attenuation rate — the rate at which the amplitude of the signal changes along the path

- Phase velocity — the rate at which a point of constant phase appears to propagate along the path

- Excitation factor (a complex quantity) — the relative efficiency with which the signal is excited by the transmitting antenna, or received by the receiving antenna.

These signal components are functions of the mode eigenvalue and signal frequency. The attenuation rate and excitation-factor amplitude jointly determine the amplitude of the mode signal. The phase velocity and excitation-factor phase jointly determine the phase of the mode signal.

Individual mode solutions of the waveguide-mode equation are distinguished from each other by numbering with positive integers. The lowest phase-velocity mode is usually labeled as "Mode 1"; Mode 2 has the next lowest phase velocity, and so on. In this mode numbering system, odd- and even-numbered modes are the transverse-magnetic (TM) and transverse-electric (TE) modes, respectively. The electric field of a TM (TE) mode is vertically (horizontally) polarized.* Therefore, the TM mode signals are most effectively received by antennas such as a vertical whip or a loop antenna, whose symmetry axis is parallel to the ground.

Mode 1 signals, in addition to having the lowest phase velocity, usually have the smallest attenuation rate and a relatively high excitation-factor amplitude. As a consequence, Omega station signals are usually dominated by their respective Mode 1 components. Omega signals

---

*Vertical, i.e., perpendicular to the earth's surface.

are not dominated by their associated Mode 1 components in the station "near-field" region which typically extends to ranges of 300-500 km during daytime, 1000-3000 km during nighttime, and for all ranges along certain westerly-directed, nighttime paths. The signal condition in which Mode 1 is not dominant is commonly referred to as the "modal condition." A modal signal is either composed of several semi-dominant modes or dominated by a single mode, other than Mode 1. A modal signal is unsuited for Omega navigation.

3.3 THEORETICAL DATABASE

This section presents the approach used to generate the theoretical database required to develop the geomagnetic/conductivity sub-model. Also described in this section are relevant features of the Mode 1 database which consists of theoretical values of the Mode 1 signal phase components (i.e., phase velocity and excitation-factor-phase) as functions of the worldwide values of the spatial parameters (i.e., ground conductivity and geomagnetic field). The Mode 1 signal phase components are computed for:

- Daytime and nighttime
- The three signal frequencies: 10.2, 11 1/3, and 13.6 kHz.

The conductivity at a path segment is simply the ground conductivity (read from a conductivity map/file) at the center of the path segment. Other spatial parameters include the vector geomagnetic field and the direction of signal propagation. If the geomagnetic field is approximated as an earth-centered magnetic dipole field, then, in terms of path coordinates (i.e., two axes parallel $(T_{||})$ and perpendicular $(T_{\perp})$ to the path in the local tangent plane of the earth, and one axis radially upward), the field components may be written

$$B_{T_\perp} = M \sin\beta_m \cos\theta_m \; ; \; B_{T_{||}} = M \cos\beta_m \cos\theta_m \; ; \; B_r = 2M \sin\theta_m$$

where

$$M = \frac{|B_{EQ}|}{(1 + 3\sin^2\theta_m)^{1/2}}$$

β_m = geomagnetic path bearing ; θ_m = geomagnetic latitude

Here, $|B_{EQ}|$ is the magnitude of the geomagnetic field at the earth's surface* at the geomagnetic equator. Thus only β_m and θ_m (in addition to the fixed constant $|B_{EQ}|$) are needed to specify the geomagnetic field components relative to the path orientation.

As described in Section 3.2, the phase components of a mode signal are derived from the eigenvalue of the mode and signal frequency. Thus to form the required database for the submodel, a database of Mode 1 eigenvalues must be computed which is parametric in the spatial path parameters, signal frequency, and illumination condition. The approach used here to generate such an eigenvalue database is to use the IPP computer code (Ref. 18), together with the MODESRCH computer code (Ref. 19) both developed at the Naval Ocean Systems Center.

Since the desired database currently exists for 10.2 and 13.6 kHz (Ref. 21), the 11-1/3 kHz database was generated under this effort. The 11-1/3 kHz database was generated using IPP, aided by MODESRCH (as needed) for conductivity level 10 only; otherwise the database included values for the same path parameter combinations as the 10.2 and 13.6 kHz databases. The combinations included each of the ten ground conductivity levels, σ_e, (for 10.2 and 13.6 kHz only), the geomagnetic latitude, θ_m, and geomagnetic bearing, β_m, as listed in Table 3.3-1. The geomagnetic latitude/bearing grid used in the nighttime database computations is purposely chosen to be non-uniform with increasing number of grid computation points

Table 3.3-1   Geomagnetic Latitude and Bearing Grids used in the Database

ILLUMINATION	GRID TYPE	SPACING BETWEEN GRID LINES $\Delta\theta_m \times \Delta\beta_m$ (deg)	GRID BOUNDS	
			GEOMAGNETIC LATITUDE, θ_m (deg)	GEOMAGNETIC BEARING, β_m (deg)
Degree	D-1	10×10	$0 \le \theta_m \le 90$	$90 \le \beta_m \le 270$
Night	N-1	10×10	$30 \le \theta_m \le 90$	$90 \le \beta_m \le 270$
	N-2	5×5	$10 \le \theta_m < 30$	$90 \le \beta_m \le 270$
	N-3	1×5	$0 \le \theta_m < 10$	$90 \le \beta_m \le 170$ and $210 \le \beta_m \le 270$
	N-4	1×1	$0 \le \theta_m < 10$	$170 < \beta_m < 210$

*There is negligible difference between $|B_{EQ}|$ at the earth's surface and $|B_{EQ}|$ at D-region altitudes.

at lower geomagnetic latitudes and westerly geomagnetic bearings where mode eigenvalues change very rapidly for a small change in the spatial parameters.

The available 10.2 and 13.6 kHz databases include three daytime modes (Modes 1, 2, 3) and five nighttime modes (Modes 1, 2, 3, 4, X). The 11-1/3 kHz database is limited to two daytime modes (Modes 1, 2) and three nighttime modes (Modes 1, 2, X). Because of the approximate symmetry of the eigenvalues (e) i.e.,

$$e\ (\theta_m, \beta_m)\ =\ e\ (-\theta_m, \beta_m) \tag{3.3-1}$$

$$e\ (\theta_m, \beta_m)\ =\ e\ (\theta_m, 180^\circ - \beta_m) \tag{3.3-2}$$

the eigenvalues were computed (and are contained in the database) only for $0^\circ \leq \theta_m \leq 90^\circ$, and $90^\circ \leq \beta_m \leq 270^\circ$.

Figures 3.3-1(a) and 3.3-1(b) depict the θ_m- and β_m-dependence of the eigenvalues for daytime/nighttime, 13.6 kHz signal frequency, and conductivity level 10 (seawater). The eigenvalues are from the database described above. Similar dependence is exhibited by the modes at other frequencies (e.g., 10.2 and 11-1/3 kHz) and ground conductivity levels (Ref. 22). In the nighttime database (see Fig. 3.3-2); the mode labeled as Mode X is a new mode, identified in recent work (Ref. 22). Mode X is found to exist for the westerly geomagnetic bearings and low geomagnetic latitudes (typically $\theta_m < 15^\circ$) at all Omega frequencies and ground conductivity levels. Mode X eigenvalues become increasing difficult to find as θ_m increased above 15° and/ or β_m decreased below 185°. The Mode X eigenvalues are shown in Fig. 3.3-1(b) for only $\theta_m \leq 10^\circ$. Similar Mode X behavior is seen at other frequencies and ground conductivity levels. The causes of this anomalous Mode X behavior are currently not well understood and need to be investigated. In the nighttime plot (Fig. 3.3-1(b)), each of the odd-numbered modes exhibits "trend reversal" in its θ_m and β_m behavior. Thus, for example in Fig. 3.3-1(b), over the entire range of β_m values, the β_m-dependence of Mode 1 for $\theta_m \leq 5^\circ$ (and Mode 3 for $\theta_m \leq 7^\circ$) is opposite in shape to that of Mode 1's β_m-dependence for $\theta_m \geq 6^\circ$ (and Mode 3 for $\theta_m \geq 8^\circ$). Earlier work (Ref. 3) did not identify a trend reversal in the nighttime Mode 1 eigenvalues with the implication that the β_m-dependence for the eigenvalues has the same characteristic shape for $\theta_m < 10^\circ$ as that found for $\theta_m > 10^\circ$. The earlier work further implies that higher-order odd modes have a similar dependence on θ_m and β_m as Mode 1. The nighttime Mode 1 eigenvalue pattern of θ_m and β_m dependence implied by the earlier work is composed of portions of Mode 1 and Mode X as defined in this report. For example, Mode 1 as used in the 1980 PPC
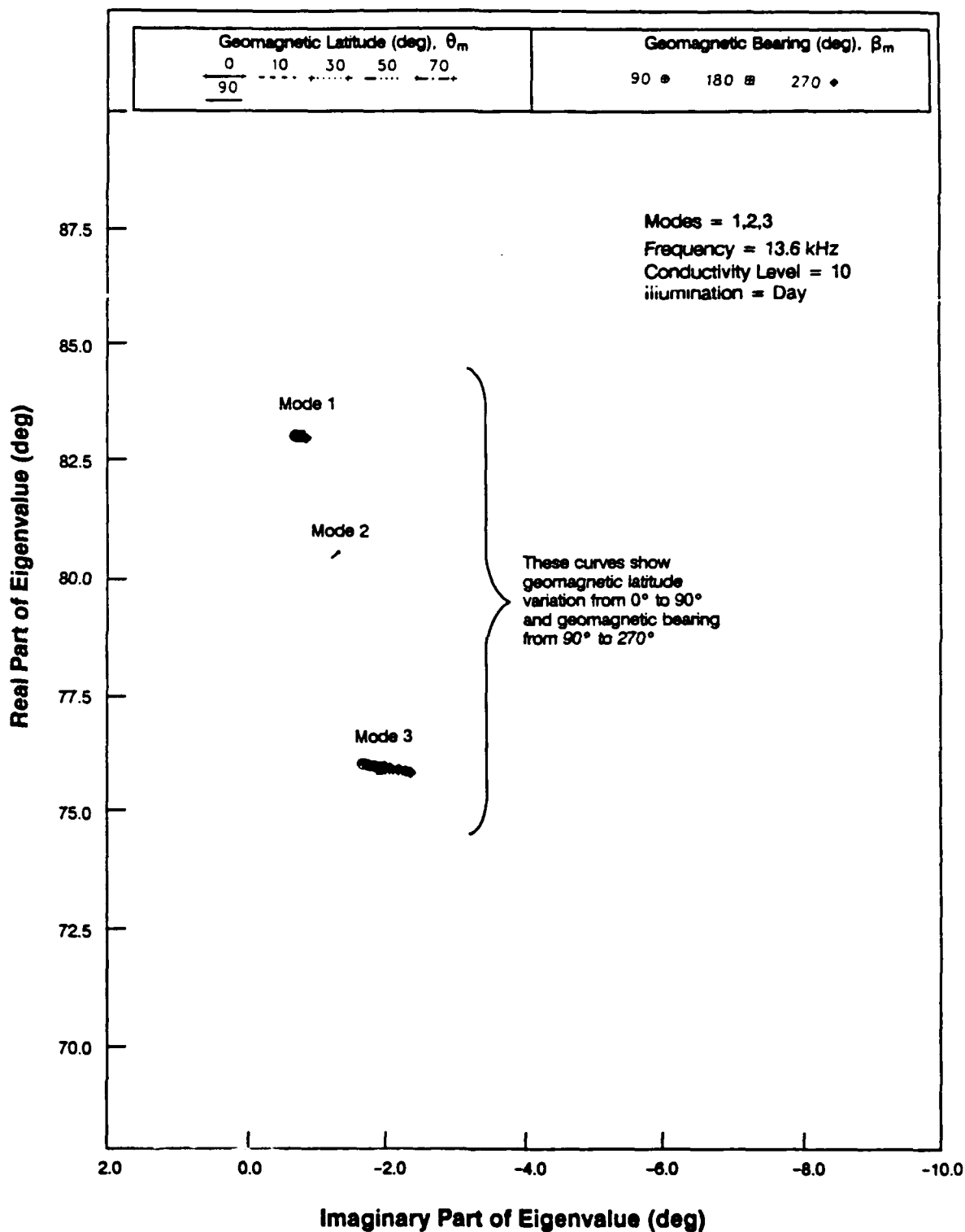
Figure 3.3-1(a) Eigenvalue Plots of Daytime Modes 1,2,3:
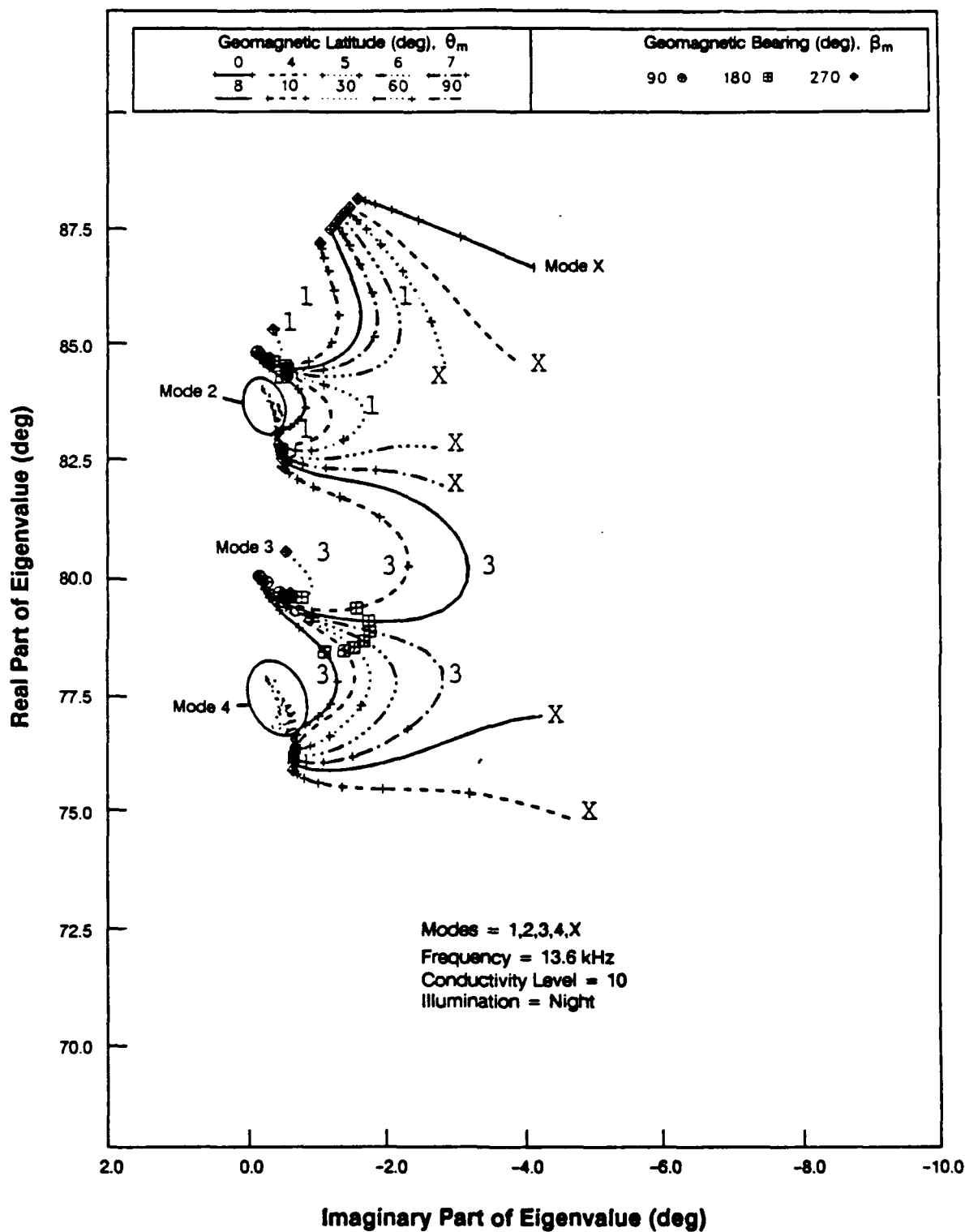Geomagnetic Latitude/Geomagnetic Bearing

Figure 3.3-1(b) Eigenvalue Plots of Nighttime Modes 1,2,3,4,X:
Geomagnetic Latitude/Geomagnetic Bearing

3-9

model[*] is made of the following portions of the eigenvalue curves in Fig. 3.3-2: (1) Mode 1 for $|\theta_m| \geq 6°$, (2) Mode 1 for $|\theta_m| < 6°$ and $90° \leq \beta_m \leq 180°$, and (3) Mode X for $|\theta_m| \leq 5°$ and $180° < \beta_m < 270°$. The composite behavior of this mode, referred to as Mode 1: Candidate II, is shown in Fig. 3.3-2(a). The other possibility is that the Mode 1 eigenvalue behavior as a function of β_m and θ_m is that identified in Fig. 3.3-1(b), including the two characteristic classes of shapes, one for $\theta_m \geq 6°$ and one for $\theta_m < 6°$. The composite behavior of this mode, referred to as Mode 1: Candidate I, is depicted in Fig. 3.3-2(b).

In view of the above two differing candidate structures for the Mode 1 eigenvalues, it is recommended that the model structure be calibrated using functional forms derived from each of the two candidate Mode 1 structures. If sufficient data exists with the appropriate ranges of θ_m and β_m, the results of the model calibration should determine which candidate best explains the observations. Section 3.4 presents the functional forms for the two candidates.

Figure 3.3-3 depicts the θ_m- and β_m-dependence of the phase components of the daytime Mode 1 for conductivity level 10 (seawater) and a frequency of 13.6 kHz. Figures 3.3-4 and 3.3-5 show the θ_m and β_m-dependence of the computed phase components of the nighttime Mode 1: Candidate I and Mode 1: Candidate II, respectively, for the same ground conductivity level and frequency as for the daytime phase components plots. The detailed expressions relating the signal amplitude/phase components to the associated mode eigenvalue and signal frequency are given in Ref. 23. Information in Figs. 3.3-3 through 3.3-5 is derived from the eigenvalue data shown in Figs. 3.3-1 and 3.3-2. The phase components database, as described in Section 3.4, is used to develop the structure of the Mode 1 signal phase components sub-model.

3.4   SUB-MODEL STRUCTURE

This section presents the structure of the geomagnetic/conductivity sub-model including two candidates (Mode 1: Candidate I and Mode 1: Candidate II) for the nighttime Mode 1. To formulate the sub-model, daytime/nighttime plots of the Mode 1 phase components, as functions of frequency, ground conductivity level, geomagnetic latitude, and geomagnetic bearing were examined to identify signal frequency and path parameter-dependent trends.

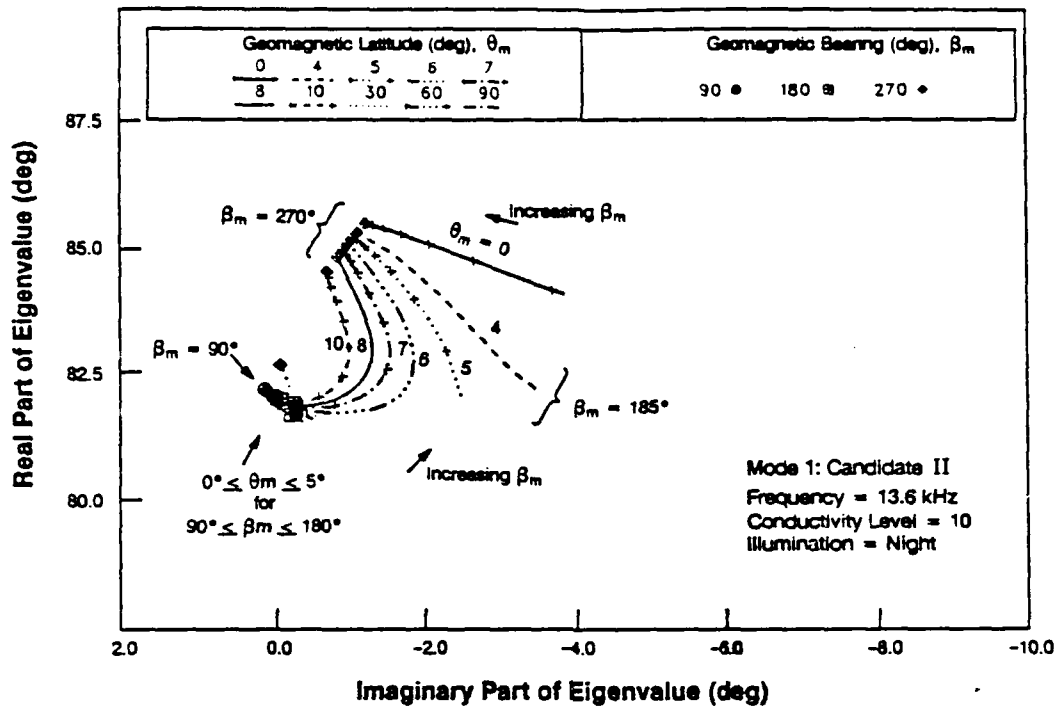[*]As implied by the phase velocity functional forms for bearing/dip angle.

Figure 3.3-2(a)　Eigenvalue Plots of Nighttime Mode: Candidate II as Functions of Geomagnetic Latitude and Geomagnetic Bearing
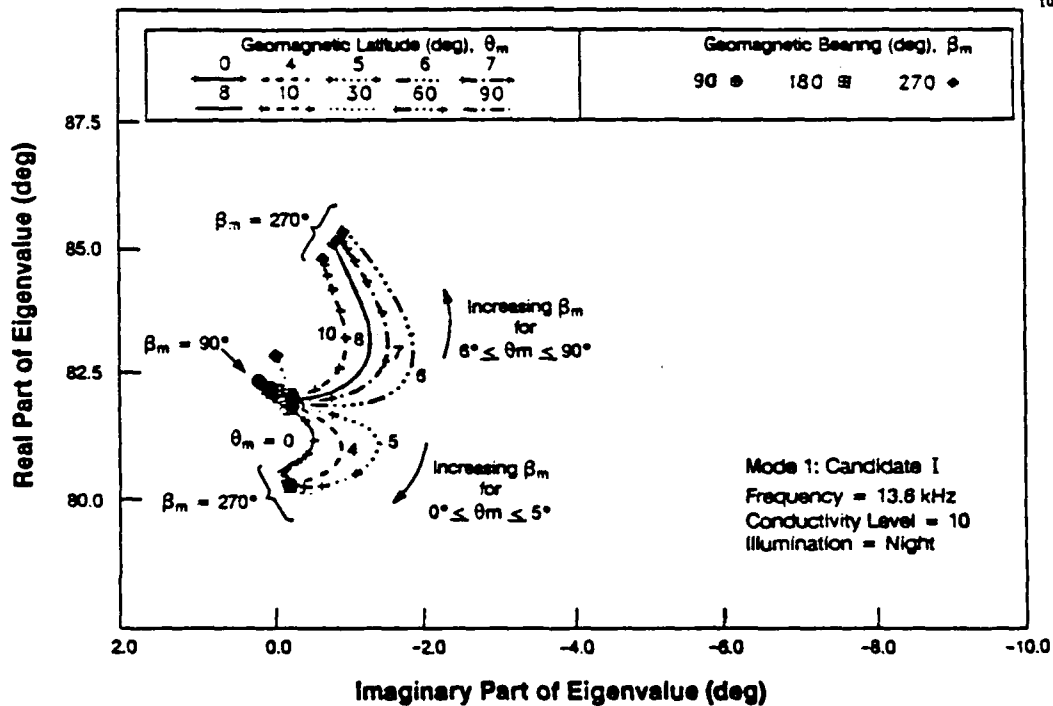
Figure 3.3-2(b)　Eigenvalue Plots of Nighttime Mode: Candidate I as Functions of Geomagnetic Latitude and Geomagnetic Bearing
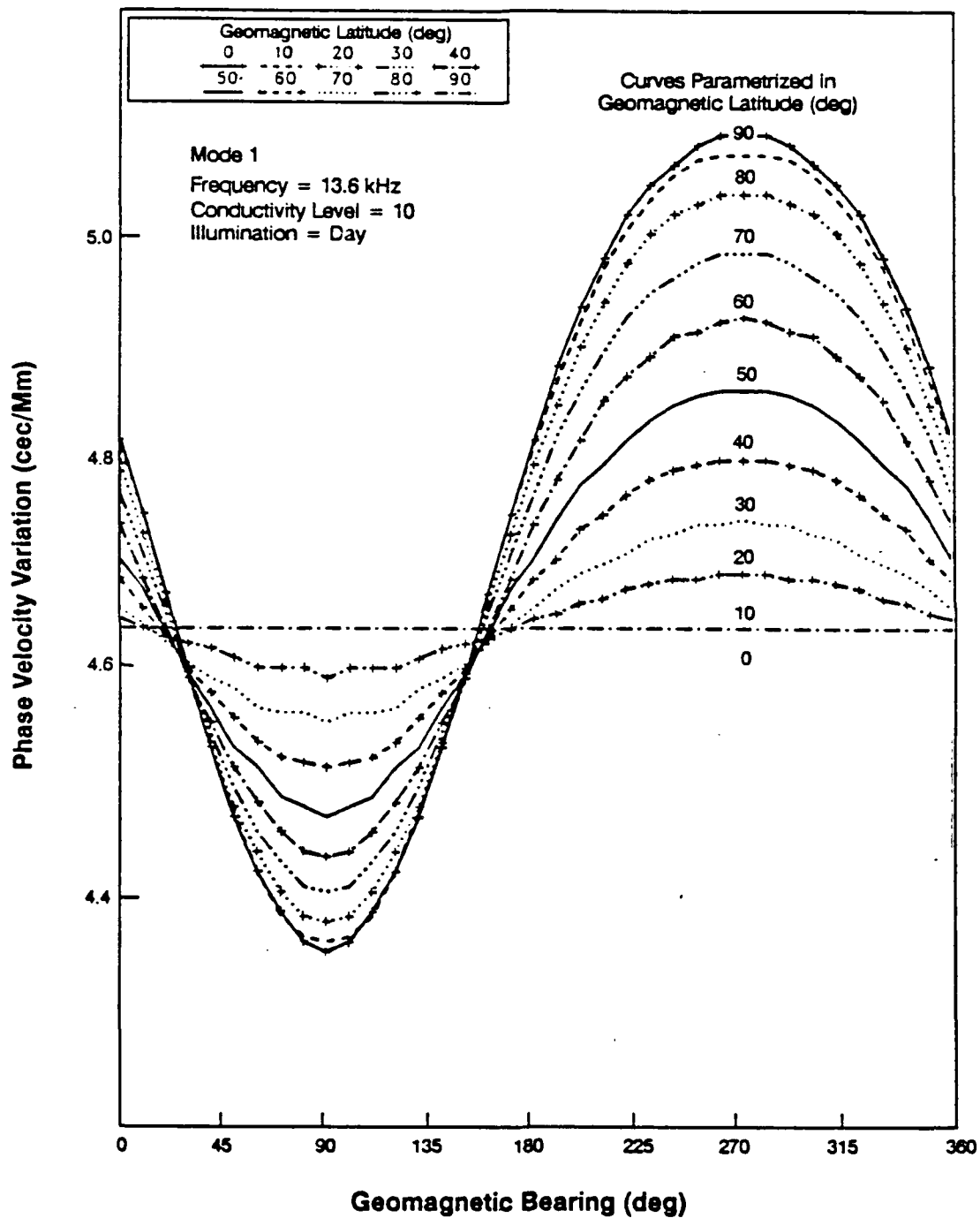
Figure 3.3-3(a) Daytime Mode 1 Phase Velocity Dependence on Geomagnetic Latitude/Geomagnetic Bearing
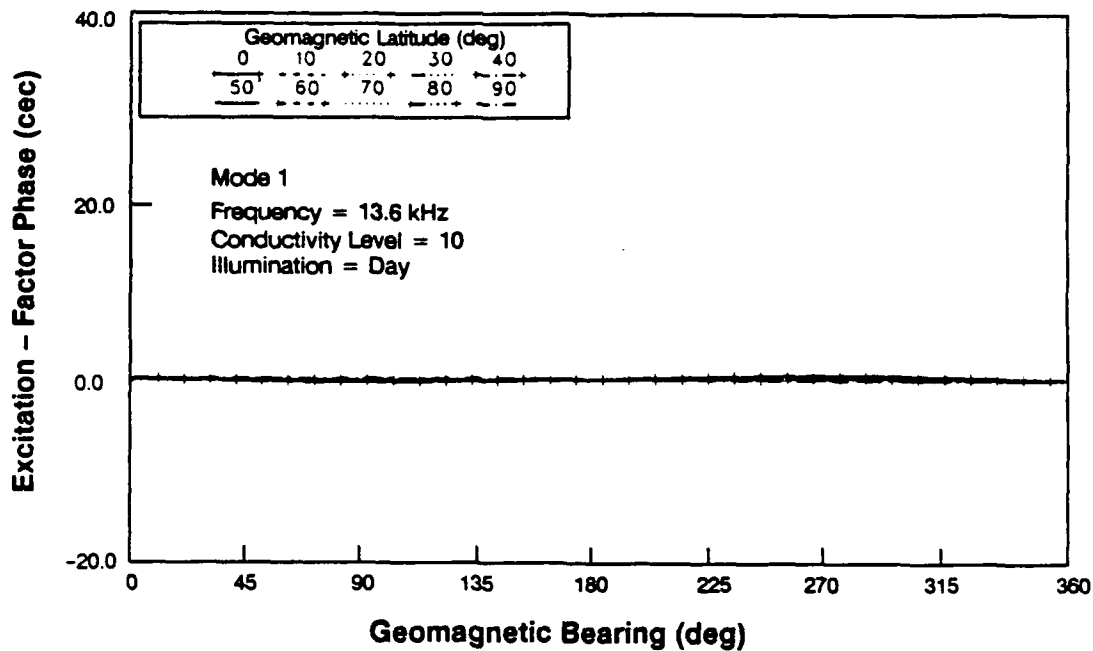
Figure 3.3-3(b) Daytime Mode 1 Excitation-Factor Phase Dependence on Geomagnetic Latitude/Geomagnetic Bearing

Examination of the parameter trends in the plots suggested the following form to model the phase component behavior as a function of frequency, conductivity-level, and illumination condition:

$$
\begin{bmatrix} \text{Phase component} \\ \text{for a specified} \\ \text{combination of} \\ f_p, \ \sigma_l, \ D/N \end{bmatrix} = \sum_{j=1}^{J^{D/N}} C_j^{f_p,\sigma_l,D/N} \ F_j^{D/N}(\theta_m,\beta_m)
$$

$$
+ \sum_{i=1}^{I^N} D_i^{f_p,\sigma_l,N} \ G_i^{f_p,\sigma_l,N}(\theta_m,\beta_m)]
$$

(3.4-1)

where

D/N	= Day/Night
f_p	= p^{th} frequency (f_1=10.2, f_2=111/3, and f_3=13.6 kHz)
σ_l	= ground conductivity for l^{th} conductivity level (l=1,2, ..., 10)
θ_m	= geomagnetic latitude
β_m	= geomagnetic bearing

3-13
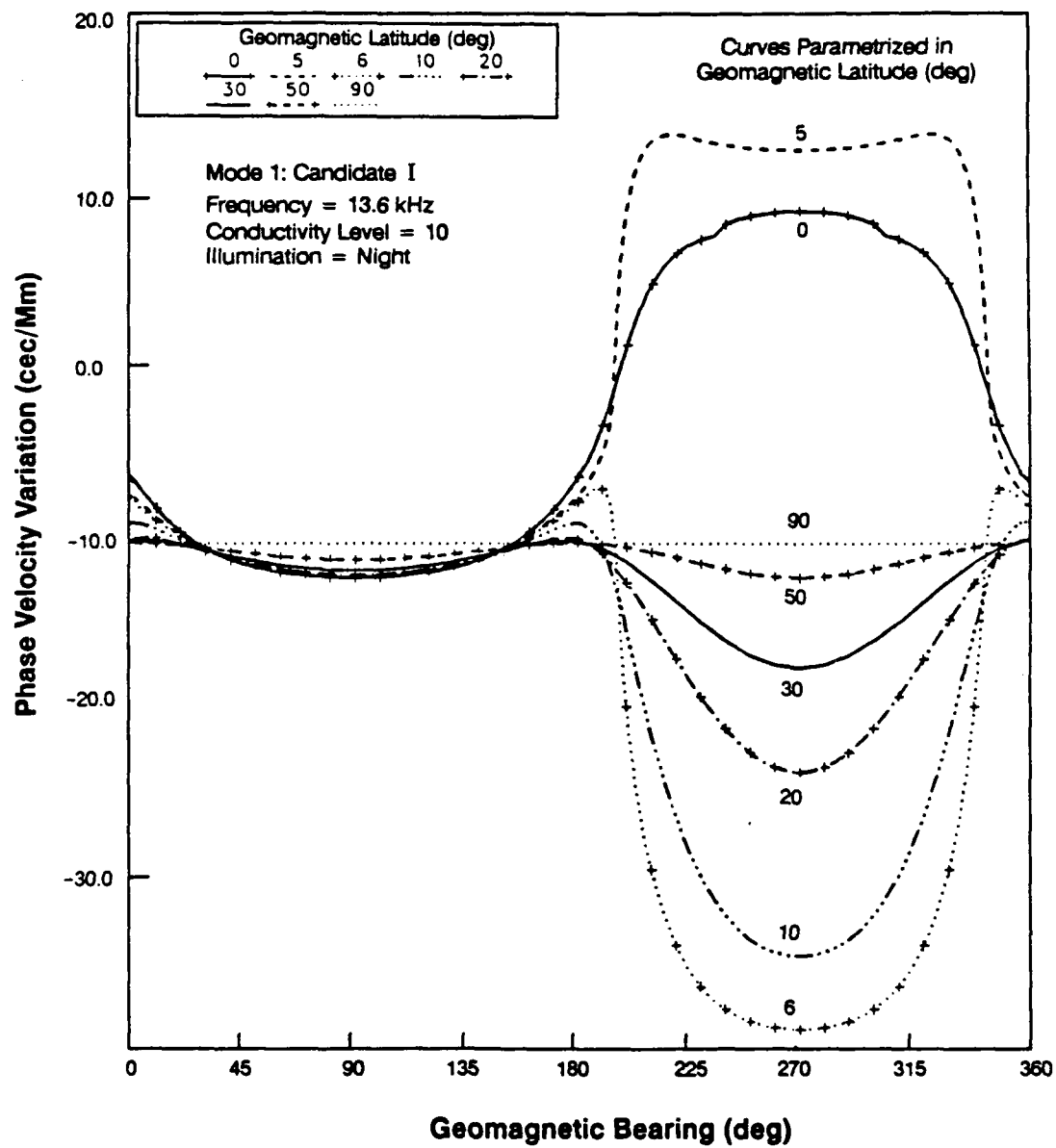
Figure 3.3-4(a) Nighttime Mode 1: Candidate I Phase Velocity Dependence on
Geomagnetic Latitude/Geomagnetic Bearing

Figure 3.3-4(b) Nighttime Mode 1: Candidate I Excitation Factor Phase
Dependence on Geomagnetic Latitude/Geomagnetic Bearing
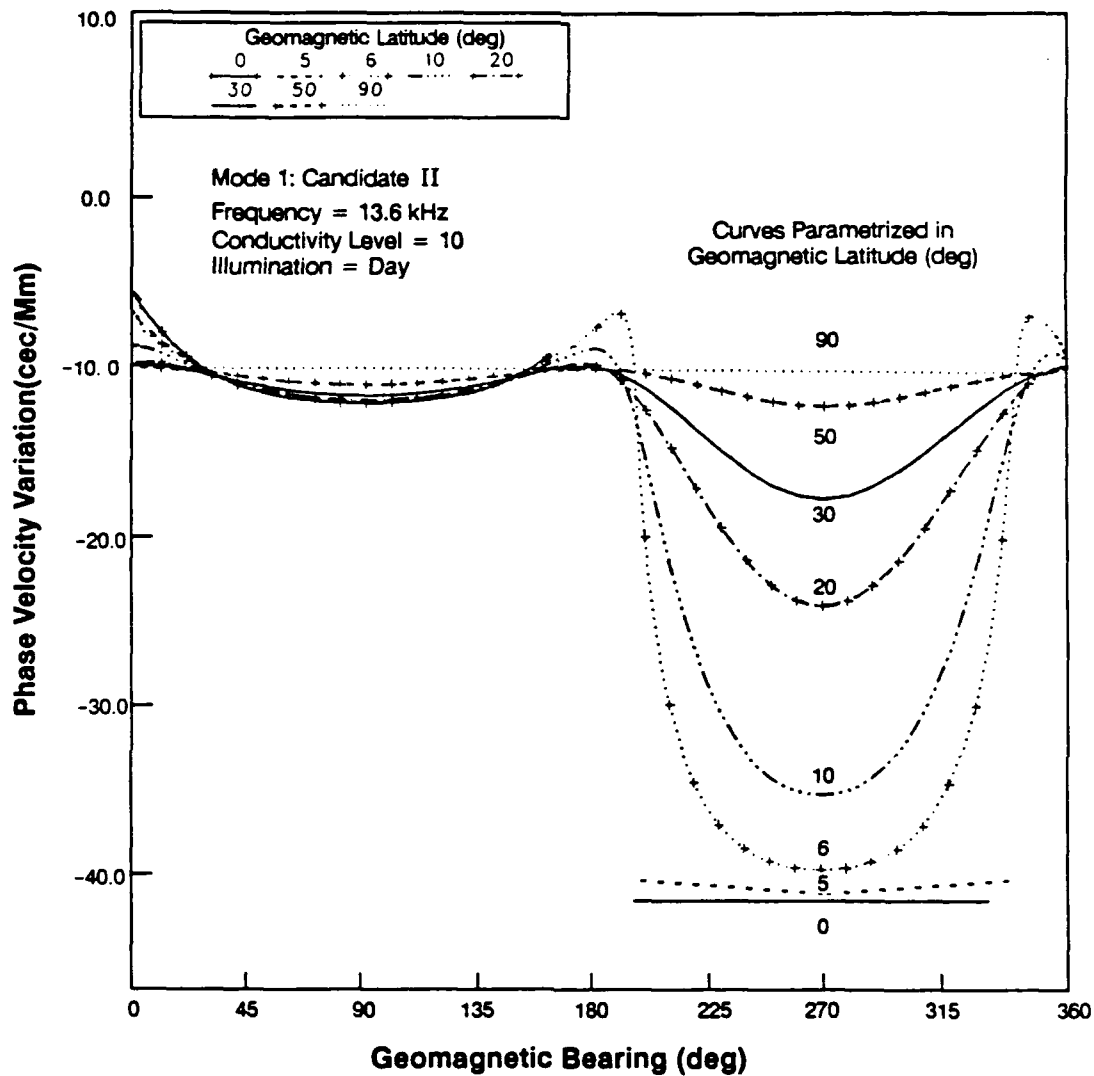
Figure 3.3-5(a) Nighttime Mode 1: Candidate II Phase Velocity Dependence
on Geomagnetic Latitude/Geomagnetic Bearing

$C_j^{f_p,\sigma_l,D/N}$ = j^{th} calibration coefficient associated with analytic functional
form j for frequency f_p and conductivity σ_l for day/night

$F_j^{D/N}(\theta_m, \beta_m)$ = j^{th} analytic functional form for day and night depending
on θ_m and β_m

$D_i^{f_p,\sigma_l,N}$ = i^{th} calibration coefficient associated with tabulated functional
form i for frequency f_p and conductivity σ_l for day/night
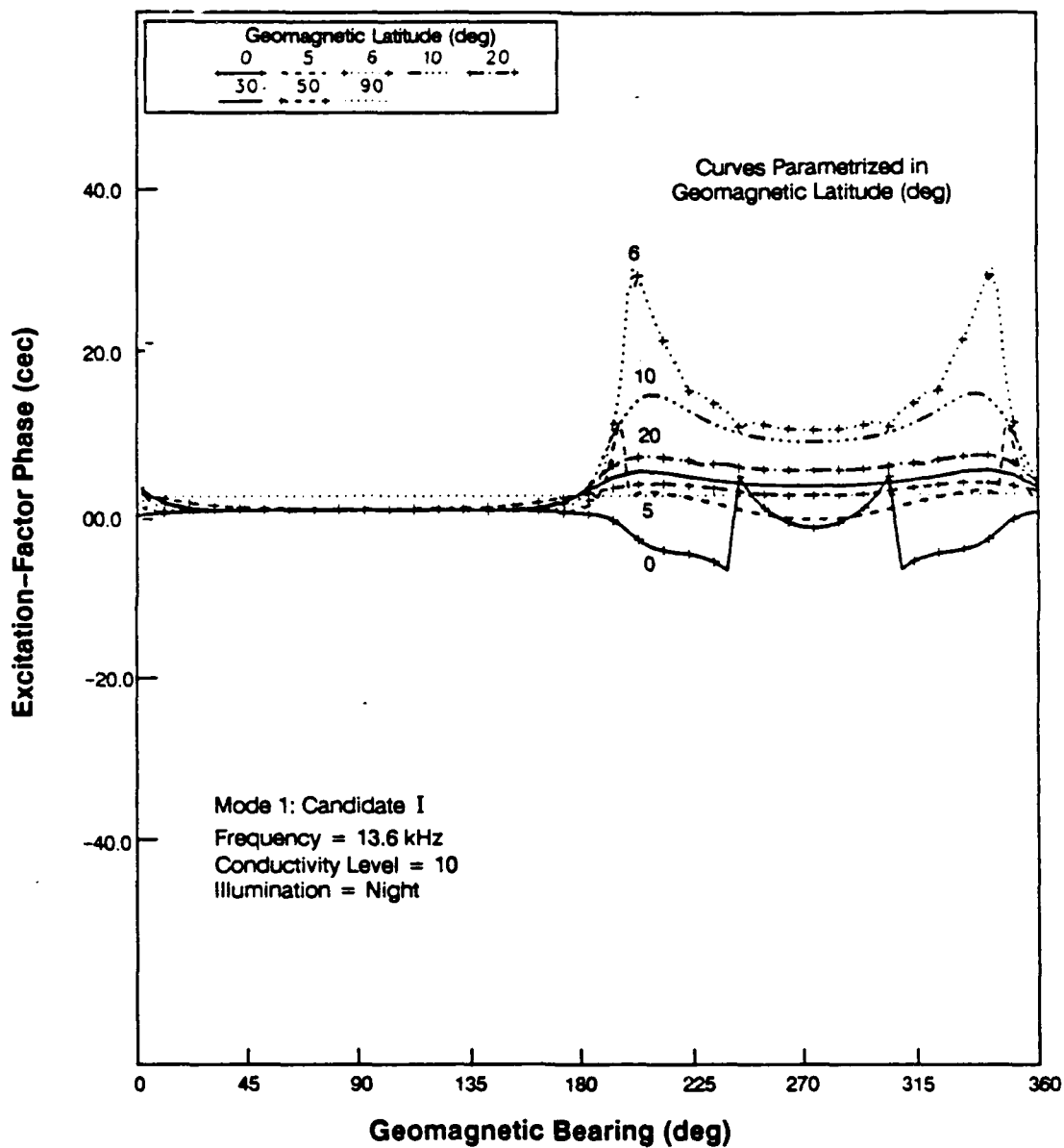
Figure 3.3-5(b) Nighttime Mode 1: Candidate II Excitation-Factor Phase Dependence on Geomagnetic Latitude/Geomagnetic Bearing

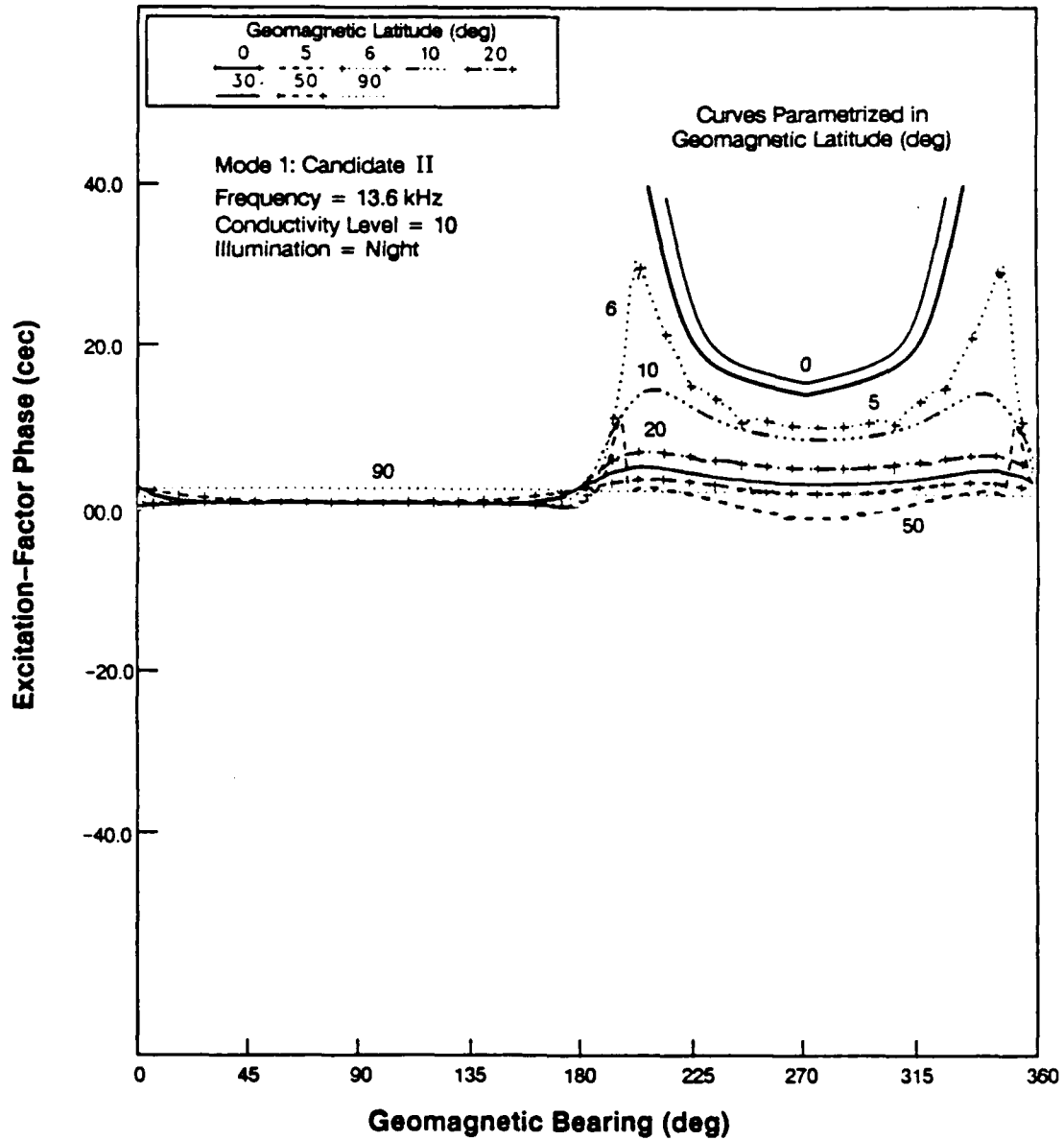$G_i^{f_p,\sigma_l,N}(\theta_m,\beta_m)$ = i^{th} tabulated nighttime functional form for frequency f_p and conductivity σ_l depending on θ_m and β_m

$J^{D/N}$ = Number of day (D)/night (N) calibration coefficients associated with the analytic functional forms

I^N = Number of night (N) weighting coefficients associated with the tabulated functional forms.

The analytic functional form is a combination of trigonometric and/or exponential functions of θ_m and β_m, whereas the tabulated functional form is a look-up table of data values for each conductivity level and frequency parametric in θ_m and β_m. Note that the analytic functional forms are independent of frequency and conductivity level, whereas the tabulated functional forms are specified for each frequency and conductivity level. The tabulated functional forms describe the nighttime behavior of the phase components for each of the two nighttime Mode 1 candidates (proposed in Section 3.3), under the condition $\theta_m < \theta_m^{T(f_p,\sigma_l)}$ where $\theta_m^{T(f_p,\sigma_l)}$ is the geomagnetic latitude value at which Mode 1 exhibits reversal of its characteristic dependence on θ_m and β_m. Also, $\theta_m^{T(f_p,\sigma_l)}$ varies slightly with signal frequency, f_p, and the conductivity level, σ_l.

The sub-model phase components dependence on θ_m and β_m should be determined separately for the three frequencies and five of the ten conductivity levels. The reason for selecting five of the ten conductivity levels is that the phase component value for any of the missing conductivity levels (i.e., levels 5, 6, 7, 8, or 9; see Table 3.2-1) can be accurately obtained by linearly interpolating the phase component values between the conductivity levels 4 and 10.

The methodology for developing each of the phase components of the sub-model is as follows. First, alternative candidate expressions, consisting of different sets of analytic/tabulated functional forms, are postulated for the phase component. Second, each candidate expression is fit to the data (from the theoretical database) of the associated phase component, using a least-squares estimation technique. Third, the rms (root-mean-square) fit error of the selected candidate expressions are compared along with the number of calibration coefficients included in the corresponding expressions. Fourth, and finally, based on a tradeoff between minimizing the number of calibration coefficients and minimizing the fit error, a "best-fit" expression is chosen for the selected phase components. Tables 3.4-1 and 3.4-2 present the calibration coefficients and the analytic/tabulated functional forms representing the selected best-fit expressions for the phase velocity and excitation-factor-phase components. These tables show the theoretical, frequency-specific values of the calibration coefficients for conductivity level 10 (seawater).

Table 3.4-1 Phase Velocity Component* Functional Forms and Associated Calibration Coefficients: Conductivity Level 10

ILLUMINATION	F_j/G_i	FORM	θ_m	β_m	10.2	11-1/3	13.6
Day	F_1	1	$0 \le \lvert\theta_m\rvert \le \frac{\pi}{2}$	$0 \le \beta_m \le 2\pi$	14.49	10.77	4.64
	F_2	$\sin \beta_m \cos \theta_m$			−0.21	−0.27	−0.32
	F_3	$\cos 2\,\beta_m \cos \theta_m$			0.09	0.07	0.04
	F_4	$\frac{1}{2}(1 + \cos 2\,\theta_m)$			0.06	0.05	0.03
	F_5	$\sin \beta_m \cos 3\,\theta_m$			−0.05	−0.05	−0.03
Night	F_1	1		$0 \le \beta_m \le 2\pi$	−1.00	−4.20	−10.08
	F_2	$\begin{aligned}\sin \beta_m \cos \theta_m \\ 0.0\end{aligned}$	$\frac{\pi}{30} \le \lvert\theta_m\rvert \le \frac{\pi}{2}$	$\begin{aligned}0 \le \beta_m \le \pi \\ \pi < \beta_m \le 2\pi\end{aligned}$	0.53	0.72	1.44
	F_3	$\begin{aligned}\cos 2\,\beta_m \exp[-(\theta_m/0.235\pi)^2] \\ 0.0\end{aligned}$		$\begin{aligned}0 \le \beta_m \le \pi/4 \\ \text{and} \\ \frac{3\pi}{4} \le \beta_m \le 2\pi \\ \frac{\pi}{4} \le \beta_m < \frac{3\pi}{4}\end{aligned}$	3.26	3.80	5.58
	F_4	$\begin{aligned}\lvert\sin \beta_m\rvert^{0.7} \exp[-(\theta_m/0.1\pi)^2] \\ 0.0\end{aligned}$		$\begin{aligned}\pi \le \beta_m \le 2\pi \\ 0 \le \beta_m \le \pi\end{aligned}$	−19.39	−19.50	−19.98
	F_5	$\frac{1}{2}(1 + \cos 2\,\theta_m)$		$0 \le \beta_m \le 2\pi$	−0.43	−0.53	−0.85
	G_1	Tabulated Function, G_1	$0 \le \lvert\theta_m\rvert \le \frac{\pi}{30}$		1	1	1

COEFFICIENT (cec/Mm) FOR EACH FREQUENCY (kHz)

*Except for the tabulated function, G_1, all other functions and coefficients are same for both Mode 1: Candidate I and Mode 1: Candidate II

Table 3.4-2 Excitation-Factor Phase Component* Functional Forms and Associated Calibration Coefficients: Conductivity Level 10

ILLUMINATION	FUNCTIONAL FORM				COEFFICIENT (cec) FOR EACH FREQUENCY (kHz)		
	F_j/G_i	FORM	PARAMETER LIMITATIONS		10.2	11·i/3	13.6
			θ_m	β_m			
Day	F_1	1			2.44	2.49	2.67
	F_2	$\sin \beta_m \cos \theta_m$	$0 \leq |\theta_m| \leq \dfrac{\pi}{2}$	$0 \leq \beta_m \leq 2\pi$	-0.57	-0.51	-0.43
Night	F_1	1		$0 \leq \beta_m \leq 2\pi$	1.81	1.88	2.21
	F_2	$\sin \beta_m \exp[-(\theta_m/0.098\pi)^2]$ $\cdots\cdots$ 0.0	$\dfrac{\pi}{30} \leq |\theta_m| \leq \dfrac{\pi}{2}$	$\pi < \beta_m \leq 2\pi$ $\cdots\cdots$ $0 \leq \beta_m \leq \pi$	-3.21	-4.69	-6.81
	F_3	$\sin \beta_m \cos \theta_m$		$0 \leq \beta_m \leq 2\pi$	-1.37	-1.41	-1.78
	F_4	$\exp\{-[(\beta_m - 1.138\pi)/0.148\pi]^2\}$ $\times \exp[-(\theta_m/0.098\pi)^2]$			8.62	9.21	11.31
	G_1	Tabulated Function*, G_1	$|\theta_m| < \dfrac{\pi}{30}$	$0 \leq \beta_m \leq 2\pi$	1	1	1

*Except for the tabulated function, G_1, all other functions and coefficients are same for both Mode 1: Candidate I and Mode 1: Candidate II

Note that the calibration coefficients are uniquely defined for frequency and conductivity level and therefore a different set of coefficients will be obtained for different combinations of frequency and conductivity level. Also, the tabulated functional forms in the tables will be different for different combinations of frequency and conductivity level. It is seen that the analytic functional forms are same for both nighttime Mode 1 candidates (Mode 1: Candidate I and Mode 2: Candidate II); however the tabulated functional forms are significantly different for the two candidates. Although Tables 3.4-1 and 3.4-2 include a single tabulated functional form, G_1, for each the nighttime phase component and conductivity level/frequency combination, it would be desirable to have several (instead of one) tabulated functional forms if the additional calibration coefficients associated with the additional tabulated forms can be adequately calibrated with the available observational data.

Table 3.4-3 gives fit-error performance of the daytime and nighttime phase components for conductivity level 10 and all three frequencies. Since the nighttime phase components for the two nighttime Mode 1 candidates differ only in the tabulated functional form which has no fit error, the performance of each of the phase components is the same for the two Mode 1 candidates.

Table 3.4-3(a) Performance of Best-Fit Functional Forms/Coefficients for Phase Velocity Component: Conductivity Level 10

ILLUMINATION	NUMBER OF CALIBRATION COEFFICIENTS	RMS (MAXIMUM) FIT-ERROR (cec/Mm) FOR EACH FREQUENCY (kHz)		
		10.2	11-1/3	13.6
Day	5	.03 (0.07)	.03 (.07)	0.03 (0.05)
Night	5	0.49 (1.48)	0.57 (1.78)	0.76 (2.41)

Table 3.4-3(b) Performance of Best-Fit Functional Forms/Coefficients for Excitation-Factor Phase Component: Conductivity Level 10

ILLUMINATION	NUMBER OF CALIBRATION COEFFICIENTS	RMS (MAXIMUM) FIT-ERROR (cec) FOR EACH FREQUENCY (kHz)		
		10.2	11-1/3	13.6
Day	2	0.05 (0.12)	0.05 (0.14)	0.05 (0.12)
Night	4	0.21 (0.68)	0.33 (0.89)	0.76 (2.50)

3.5 SUMMARY

The geomagnetic/conductivity sub-model of the 1990 PPC model characterizes the dependence of the Omega signal's Mode 1 phase component on the spatially-varying geophysical parameters (ground conductivity and geomagnetic field) of the signal path for day and night solar illumination conditions, and signal frequencies of 10.2, 11-1/3, 13.6 kHz. The signal phase is described in terms of the two phase components (phase velocity and excitation-factor phase) of the Mode 1 signal. Theoretical phase components data parametric in signal frequency and spatial path parameters for both day and night conditions are obtained using a waveguide-mode model of VLF signal propagation prediction. This database is used to deduce the structure of each of the phase components. An examination of the plots displaying the parametric dependence of the mode eigenvalues and phase components indicates that the nighttime Mode 1 behavior (as shown in Fig. 3.3-1(b)) is significantly different from that implied in the 1980 PPC model. Therefore, the sub-model structure is developed for two alternative candidates for the nighttime Mode 1, referred to as Mode 1: Candidate I and Mode 1: Candidate II. Several plausible candidate structures for each of the day and night phase components are postulated. These candidates are calibrated with theoretical data and a best-fit candidate is selected for the sub-model. It is recommended that this structure, as a part of the 1990 PPC model, be calibrated with observational data to: (1) select the correct nighttime mode from the proposed two candidates, and (2) determine the values of the calibration coefficients.

4. OVERALL PPC MODEL STRUCTURE

4.1 INTRODUCTION

The temporal and spatial sub-models, introduced in Chapters 2 and 3, describe signal phase variations under conditions in which one of the categories of parameters (spatial or temporal) varies from segment-to-segment while the other category has its parameters fixed at nominal values. Thus, in the diurnal sub-model, the day-to-night scaling is selected as that expected for a mid-latitude, north-south path over seawater. Similarly, for the geomagnetic/latitude sub-model, the local ionosphere is considered either "day" ($\chi = 0$) or night ($\chi = \pi$). The method by which the spatial and temporal phase variations are combined to provide a total phase variation is specified by the overall model structure. This chapter explains the roles of the two sub-models in calculating the total phase prediction/propagation correction (PPC). Also, a suggested procedure is given for calibrating the model coefficients including the onset/recovery time parameters. Finally, the 1980 (currently used) and 1990 (proposed) PPC model structures are compared.

4.2 COMBINING THE SPATIAL/TEMPORAL SUB-MODELS

In developing the diurnal model, the signal phase variation is described in terms of the variation in effective ionospheric reflection height with solar zenith angle. For the geomagnetic/conductivity sub-model, waveguide-mode solutions for the signal phase are specified for a homogeneous waveguide with an upper ionospheric boundary, at a fixed reflection height (either day or night), composed of a plasma magnetized in various directions with respect to the propagation path and a lower boundary comprising a dielectric medium with various electrical conductivities. In terms of the waveguide-mode model, the phase contributions of the geomagnetic field (upper boundary) and phase contributions of the surface conductivity (lower boundary) are *coupled*, i.e., they cannot be independently specified in computing phase. Moreover, each component functional form making up the geomagnetic/conductivity sub-model is uniquely scaled to represent its particular contribution to the phase for day or night. Aside from the scaling, however, the *evolution* of the component spatial functional forms between the day and night extremes of effective reflection height should be the same. This fundamental assumption appears to be consistent with both theory and observation.

Thus, each spatial functional form F_j is decoupled from the evolutionary (temporal) form $E(\chi)$ and the resulting local space/time phase contribution from functional form i is

$$\Delta\phi_i = C_i F_i E(\chi) \qquad (4.2\text{-}1)$$

where C_i is the model coefficient for spatial functional form i and the expression for $E(\chi)$ is given by either Eq. 2.3-5 (daytime) or Eq. 2.4-6 (nighttime). Essentially, Eq. 4.2-1 states that functional form F_i evolves in time according to $E(\chi)$. An important modification to Eq. 4.2-1 is made depending on the temporal domain(s) over which F is defined. Equation (4.2-1) is a very general expression and its specific form depends upon the temporal domain of F_i as discussed below.

Three types of spatial functional forms are identified which evolve uniquely in time (i.e., solar zenith angle):

1. Functional forms for a local daytime ionosphere $(0 < \chi < \chi_{THR})$
2. Functional forms for a local nighttime ionosphere $(\chi_{THR} < \chi < \pi)$
3. Functional forms defined for both local daytime and nighttime iono-spheres $(0 < \chi < \pi)$.

For the type (1) functional forms, phase behavior is specified for daytime (ionosphere under direct solar control) which has no analog at night (ionosphere under control of scattered Lyman-alpha radiation). Thus as the solar zenith angle increases during daytime, this type of functional form must contribute less to the total predicted phase so that at $\chi = \chi_{THR}$ the contribution must vanish. This means that the daytime evolution function, $E_D(\chi)$, must possess the functional dependence on χ given by Eq. 2.3-5 and also be normalized so that $E_D(0)=1$ and $E_D(\chi)=0$ for $\chi \geq \chi_{THR}$. Thus,

$$E_D(\chi) = \frac{\log_e(Ch(\chi_{THR}, H_{sc})/Ch(\chi, H_{sc}))}{\log_e Ch(\chi_{THR}, H_{sc})} \qquad (0 \leq \chi \leq \chi_{THR}) \qquad (4.2\text{-}2)$$

where the dependence of the Chapman Function on z' has been suppressed. Note this form is independent of wavelength since the spatial functional forms (in some cases) and the calibration coefficients (in all cases) will be wavelength-specific. Figure 4.2-1 shows a schematic plot of $E_D(\chi)$.

The type (2) functional forms describe phase behavior only under nighttime conditions, i.e., phase behavior having the specific functional behavior described by these forms is not

Day-only spatial form: $\Delta\phi = C_D\, F_D\, E_D$
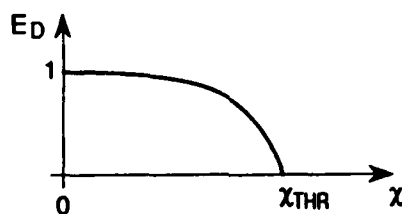
Night-only spatial form: $\Delta\phi = C_N\, F_N\, E_N$
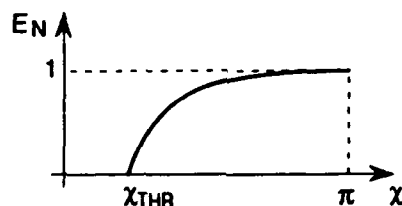
Spatial forms defined for both night and day: $\Delta\phi = (C_N - C_D)\, F E_0 + C_D F$

Figure 4.2-1   Evolution Functions for the Three Classes of Spatial Functional Forms

theoretically predicted during the daytime. Thus as the solar zenith angle decreases during the night, a smaller contribution is expected from th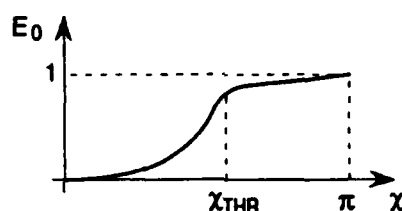is type of functional form until, finally, at $\chi = \chi_{THR}$, the contribution vanishes. The nighttime evolution function $E_N(\chi)$ must have the functional dependence on χ given by Eq. 2.4-6 and also be normalized so that $E_N(\pi)=1$ and $E_N(\chi)=0$ for $\chi \le \chi_{THR}$. Hence,

$$E_N(\chi) = \frac{\cos\chi_{THR} - \cos\chi}{1 + \cos\chi_{THR}} \qquad (\chi_{THR} \le \chi \le \pi) \qquad (4.2\text{-}3)$$

As for the daytime case, this form is independent of wavelength since the wavelength dependence is absorbed in the calibration coefficients C_N. Figure 4.2-1 shows a schematic plot of $E_N(\chi)$.

Type (3) functional forms are those which describe specific functional behavior of the phase predicted for both daytime and nighttime ionospheres. The night and day model coefficients associated with these forms furnish a measure of the scale of the day-to-night phase variation (diurnal shift) for the particular functional form. Scaled by the diurnal shift, the phase variation is given by Eqs. 2.3-5 and 2.4-6 with matching at $\chi = \chi_{THR}$. A default night variation

of 10% of the total diurnal shift is based on preliminary analysis of the data (Appendix B). Using these conditions and normalizing yields

$$E_0(\chi) = \frac{H_{sc} \log_e Ch(\chi, H_{sc})}{-A + B} \qquad \chi < \chi_{THR}$$

$$= \frac{A \cos \chi + B}{-A + B} \qquad \chi > \chi_{THR}$$

(4.2-4)

where

$$A = \frac{H_{sc} \log_e Ch(\chi_{THR}, Hsc)}{(1 - \frac{1}{\gamma})(1 + \cos \chi_{THR})}$$

$$B = H_{sc} \log_e Ch(\chi_{THR}, H_{sc}) \frac{\left(1 - \frac{(1 + \cos \chi_{THR})}{\gamma}\right)}{(1 - \frac{1}{\gamma})(1 + \cos \chi_{THR})}$$

and γ is the nighttime phase variation expressed as a fraction of the diurnal shift (default $\gamma = 0.1$). With $E_0(\chi)$ so defined, $\Delta\phi$ is generalized from the form given in Eq. 4.2-1 to explicitly show how the difference in night and day coefficients determines the scale of the diurnal shift for functional form F_i, viz.

$$\Delta\phi_i = (C_N - C_D) F_i E_0(\chi) + C_D F_i$$

(4.2-5)

For $F_i = 1$, the purely diurnal phase model of Chapter 2 is recovered. Figure 4.2-1 shows a plot of $E_0(\chi)$.

4.3 OVERALL EXPRESSION FOR PREDICTED PHASE AND PPC

In the waveguide-mode model, the predicted VLF signal phase measured on a homogeneous path from a transmitting source is

$$\phi = k R_E \psi + \phi_E^T + \phi_E^R$$

(4.3-1)

where $k = 1/\lambda$ (λ = wavelength) is the (assumed constant) wave number, R_E is the earth's radius, ψ is the radian measure of the (great-circle) path, and ϕ_E^T, ϕ_E^R are the excitation-factor phases

at the transmitting source and receive point, respectively. For an inhomogeneous path (i.e., a real path), the first term in Eq. 4.3-1 is replaced by a path integral (or sum). For the path segmentation introduced in Chapter 2, Eq. 4.3-1 becomes

$$\phi = \sum_i \sum_j k_{ij} R_E \Delta a_i + \phi_E^T + \phi_E^R \qquad (4.3\text{-}2)$$

where i indexes path segment, j indexes the component functional form of the spatial submodel, and $\Delta a_i = 0.01\,\text{radian}$ for all i. k_{ij} is the wave number corresponding to path segment i and functional form j.

In order to express the phase given by Eq. 4.3-1 in terms of the spatial functional forms/ model coefficients, a relationship is needed between the wave number and the model coefficient/functional form product. Each contribution (j) to the phase velocity (v_j) component is actually computed as (see, e.g., Fig. 3.3-3(a), vertical scale)

$$C_j F_j = (1 - v_j/c)\frac{1}{\lambda} = (1 - v_j/c)k_o \qquad (4.3\text{-}3)$$

where calibration coefficient, C_j, has units of cycles/Mm, F_j is the jth dimensionless functional form (and has magnitude between 0 and 1), k_o is the free space wave number in units of Mm^{-1}, and c is the speed of light in free space. The wave number k_j is related to the phase velocity v_j as

$$k_j = \frac{f}{v_j} \quad \text{or} \quad k_{ij} = \frac{f}{v_{ij}} \qquad (4.3\text{-}4)$$

where f is the frequency and the i is attached to show the dependence of the wave number/phase velocity on path segment. Using Eq. 4.3-3 to obtain v_j ($\rightarrow v_{ij}$) yields

$$v_{ij} = \left(1 - \frac{C_j F_{ij}}{k_o}\right) c$$

This relation together with Eq. 4.3-4, produces the following result for the wave number, k_{ij}

$$k_{ij} = \frac{f}{(1 - \frac{C_j F_{ij}}{k_o})c} = \frac{k_o}{1 - \frac{C_j F_{ij}}{k_o}} \qquad (4.3\text{-}5)$$

4-5

since $f = ck_o$. Inspection of Table 3.4-1 shows that $|C_j| < 0.20$ cycle/Mm and $|F_{ij}| \leq 1$. Thus, $|C_j F_{ij}| < 0.20$ and $k_o(10.2 \text{ kHz}) \cong 33 \text{ Mm}^{-1}$ with larger values for the other frequencies. Hence $|C_j F_{ij}/k_o| \ll 1$ and only first-order terms need be retained in the binomial series expansion of Eq. 4.3-5. Thus

$$k_{ij} = k_o(1 + \frac{C_j F_{ij}}{k_o} + ...) \cong k_o + C_j F_{ij}$$

and Eq. 4.3-2 becomes

$$\phi = k_o R_E a + R_E \sum_i \sum_j C_j F_{ij} \Delta a_i + \phi_E^T + \phi_E^R \qquad (4.3\text{-}6)$$

If N_T is defined as the total number of path segments and N_S is the number of path segments to the point of first ionospheric interaction (see Fig. 2.5-4), then $N_T - N_S$ is the number of segments to the last point of ionospheric interaction. Thus, index i is summed from N_S to $N_T - N_S$ since all sub-model components are defined only within this region (recall that the functional dependence of phase velocity couples ground conductivity and ionospheric parameters in the waveguide-mode model). The so-called "VLF ground-wave" effects over the first and last N_S segments of the path are assumed to be adequately approximated by the free-space wave number. The excitation-factor phase components, ϕ_E^T, ϕ_E^R are assumed to depend only on spatial parameters (magnetic field, path orientation, and ground conductivity) at the segments N_S and $N_T - N_S$ since these are the first/last point of ionospheric interaction and thus serve to define the spatial geophysical environment for initial/final excitation of the wave into/from the earth-ionosphere waveguide. Thus, Eq. 4.3-6 may be written

$$\phi = k_o R_E a + R_E \sum_{i=N_S}^{N_T-N_S} \sum_{j=1}^{N_f} C_j F_{ij} \Delta a_i + \sum_{i=N_S, N_T-N_S} \sum_{j=1}^{N_f'} C_j' F_{ij}' \qquad (4.3\text{-}7)$$

where the unprimed sums are associated with wave number/phase velocity components and the primed sums with excitation factor components (N_f, N_f' is the number of functional forms for the unprimed, primed component).

The expression for predicted phase, Eq. 4.3-7, is valid only at an instant of time. Dependence of the phase prediction on solar zenith angle is implemented by inserting the three types

of evolution functions (day, night, and day/night) according to the prescriptions, Eq. 4.2-1 or Eq. 4.2-5. Thus

$$\phi = k_o R_E a + R_E \sum_{i=N_s}^{N_T-N_s} \left[\sum_j C_j^D F_{ij}^D E_D(\chi_i) + \sum_j C_j^N F_{ij}^N E_N(\chi_i) \right.$$

$$\left. + \sum_j (C_j^N - C_j^D) F_{ij} E_o(\chi_i) + \sum_j C_j^D F_{ij} \right] \Delta a_i + \sum_{i=N_s,N_T-N_s} \sum_j C_j' F_{ij}' \qquad (4.3\text{-}8)$$

where the superscript D(N) on the functional form indicates that day-only (night-only) forms are to be invoked; no superscript implies that the form is invoked both night (with coefficient C^N) and day (with coefficient C^D). The primed terms again refer to the excitation factor phase component, evaluated at segments N_S and N_T-N_S, which evolves with solar zenith angle in the same fashion as phase velocity. Since, according to Table 3.4-2, there are no excitation factor forms defined for day *only*[*], $C^{D'}F^{D'} = 0$ and the excitation factor contribution to Eq. 4.3-8 becomes

$$\sum_{i=N_s,N_T-N_s} \sum_j C_j' F_{ij}' = \sum_{i=N_s,N_T-N_s} \left[\sum_j C_j^{N'} F_{ij}^{N'} E_N(\chi_i) + \sum_j (C_j^{N'} - C_j^{D'}) F_{ij}' E_o(\chi_i) + \sum_j C_j^{D'} F_{ij}' \right]$$

By definition, the propagation correction (PPC) is (Ref. 3)

$$\text{PPC} \equiv \text{NOMINAL PHASE} - \text{PREDICTED PHASE}$$

where the nominal phase is defined for a great-circle path subtending a radians as

$$\text{NOMINAL PHASE} = 0.9974\, k_o R_E a$$

Thus, the PPC becomes

$$\text{PPC} = -0.0026\, k_o R_E a - S$$

where S is that part of the predicted phase (Eq. 4.3-8) which involves the calibration coefficients, i.e.,

$$S = \phi - k_o R_E a$$

---

*Note that Table 3.4-2 contains day and night functional forms for the excitation-factor phase component. However, the two daytime functional forms are *identical* to two of the nighttime forms so that there are no *unique* daytime forms.

4.4 MODEL CALIBRATION CONSIDERATIONS

By definition, a semi-empirical model contains both theoretical and observational components. Theory is used to determine how the signal phase varies with a single parameter (e.g., ground conductivity) holding all other parameters constant. Analytical/tabular approximations to these single-parameter variations comprise the functional forms described in Chapter 3. To derive a complete expression for phase based on the known contributing variables is intractable from a theoretical viewpoint (for all but exactly linear models). In a semi-empirical formulation, calibration coefficients are used with a linearized model to approximate the exact dependence of phase on the dependent variables. Observational data is then enlisted to determine the best estimates of the calibration coefficients/parameters.

The calibration procedure must be carefully chosen due to the parameter coupling inherent in the model — especially the spatial-temporal coupling. The recommended calibration procedure addresses the three different categories of calibration coefficients/parameters according to the following sequence:

1) Daytime coefficients (both day-only and day/night)
2) Nighttime coefficients (both night-only and day/night)
3) Onset/recovery time parameters.

This sequence (which may require more than one cycle) specifies calibration of the daytime coefficients first because these coefficients should be the most stable and well-defined. Once these are determined from phase data over the appropriate observation hours (as defined below), the nighttime coefficients are computed using default onset/recovery time parameter values. Finally, the onset/recovery time parameters are determined from single-station analog phase data (as discussed below).

To isolate the daytime coefficients, phase data is selected for those hours producing the minimum predicted phase for a given path. Here, "minimum" is used loosely since the "midday" phase behavior is usually quite shallow (see Fig. 2.5-6). To define this shallowness more quantitatively, Eq. 4.2-2 may be used to show that

$$0.963 \leq E_D(\chi) \leq 1.000 \quad \text{for} \quad 0^\circ \leq \chi \leq 50^\circ$$

for default values of threshold solar zenith angle and scale height. Moreover, from Eq. 4.2-4, it can be shown that

$$0 \leq E_o(\chi) \leq 0.0335 \quad \text{for} \quad 0^\circ \leq \chi \leq 50^\circ$$

Thus in Eq. 4.3-8, the first term inside the brackets (which is defined for night-only) is zero and the fourth term may be neglected in comparison to the second term for solar zenith angles less than 50°*. Thus, Eq. 4.3-8 becomes

$$\phi = k_o R_E a + R_E \sum_{i=N_s}^{N_T-N_s} \left[\sum_j C_j^D F_{ij}^D E_D(\chi_i) + \sum_j C_j^D F_{ij} \right] \Delta a_i \qquad (4.4-1)$$

$$+ \sum_{i=N_s,N_T-N_s} \sum_j C_j^{D'} F_{ij}' \qquad\qquad 0 \le \chi \le 50°$$

For a given path and time, Eq. 4.4-1 can be used with observations for which $\chi \le 50°$ at all path segments to estimate the coefficients C_j^D and $C_j^{D'}$. It may be convenient to modify this procedure in actual practice to accept phase data only for those paths/hours in which the phase change from the "minimum day" value is less than some threshold value or acceptable fraction of the default diurnal shift.

Once the daytime calibration coefficients are determined, the nighttime coefficients (C_j^N and $C_j^{N'}$) are estimated with the use of path phase observations measured during nighttime conditions. As in the case of the daytime observations, the nighttime measurement hours are selected so that the appropriate evolution function ($E_N(\chi)$) is approximately independent of χ. This is done to reduce the sensitivity of E_N to the parameter χ_{THR} which is determined in the next calibration step. Here, an iterative approach can be used in which measurement within a given range of χ are used to calibrate the night coefficients, using Eq. 4.3-8 and a default value of χ_{THR}. If subsequent calibration yields a substantially changed value of χ_{THR}, then the night coefficients should be recalibrated using measurements from a smaller range of χ. Alternatively, if subsequent calibration of χ_{THR} yields a value close to the default value, then the night coefficients can be recalibrated using measurements corresponding to a larger range of χ. Nighttime evolution functions for two ranges of χ, computed using Eq. 4.2-3, are as follows ($\chi_{THR} = 96°$)

$$0.9327 < E_N(\chi) < 1 \quad \text{for} \quad 160° < \chi < 180°$$

$$0.6011 < E_N(\chi) < 1 \quad \text{for} \quad 130° < \chi < 180°$$

The same considerations apply to $E_o(\chi)$ which has similar numerical values for the two ranges of χ used for $E_N(\chi)$ above.

---

*Small excitation effects have also been ignored.

For nighttime conditions, Eq. 4.3-8 may be written

$$\phi = k_o R_E a + R_E \sum_{i=N_s}^{N_T-N_s} \left[\sum_j C_j^N F_{ij}^N E_N(\chi_i) + \sum_j (C_j^N - C_j^D) F_{ij} E_o(\chi_i) \right.$$

$$\left. + \sum_j C_j^D F_{ij} \right] \Delta a_i + \sum_{i=N_s, N_T-N_s} \left[\sum_j C_j^{N'} F_{ij}^{N'} E_N(\chi_i) + \sum_j (C_j^{N'} - C_j^{D'}) F_{ij}' E_o(\chi_i) \right. \quad (4.4\text{-}2)$$

$$\left. + \sum_j C_j^{D'} F_{ij}' \right]$$

Since the C_j^D and $C_j^{D'}$ are determined in the first calibration step, the only unknowns (other than the onset/recovery time parameters embedded in E_N, E_o) on the right-hand side of Eq. 4.4-2 are the coefficients C_j^N and $C_j^{N'}$.

The three principal onset/recovery time parameters, defined in Chapter 2, are given as follows:

1. Distance from transmitter (receiver) to point of first (last) ionospheric interaction (ΔL)

2. Threshold solar zenith angle (χ_{THR})

3. Ionospheric response time (τ_D, τ_N).

To show how these parameters are combined to give the sunrise/sunset onset/recovery time, consider a path at the onset of sunrise in which the transmitter is east of the receiver. It can be easily shown that other situations (i.e., sunrise recovery, sunset onset/recovery, and paths with different east/west orientations) produce the same basic expression for the appropriate time condition. The onset time must be referenced to an epoch whose occurrence is reasonably "close" in time. A convenient choice is the time at which ground sunrise occurs at the transmitter. Thus, the relative path sunrise onset time, for this case, is defined as

$$\Delta T = \text{(path sunrise onset time as observed on phase measurement)}$$
$$- \text{(time at which } \chi = \pi/2 \text{ at transmitter)}$$

This onset time can be separated into three components as follows:

$$\Delta T \equiv \Delta T_1 + \Delta T_2 + \Delta T_3 = T'(d = \Delta L) - T(\chi = \pi/2, \ d = 0)$$

where

$$\Delta T_1 \equiv T(\chi = \pi/2, \ d = \Delta L) - T(\chi = \pi/2, \ d = 0)$$

$$\Delta T_2 \equiv T(\chi = \chi_{THR}, \ d = \Delta L) - T(\chi = \pi/2, \ d = \Delta L)$$

$$\Delta T_3 \equiv T'(d = \Delta L) - T(\chi = \chi_{THR}, \ d = \Delta L)$$

In the above, $T(\chi, d)$ is the time at which the solar zenith angle is χ at distance d along the path (measured from the transmitter) and $T'(d)$ is the time at which the portion of the ionosphere at distance d on the path becomes ionized as a result of incident solar radiation at solar zenith angle χ_{THR}. Depending on the values of χ_{THR} and ΔL and the orientation of the path, the quantity ΔT_2 may be positive or negative (see Fig. 4.4-1). From the above definitions, the components of ΔT may be written

$$\Delta T_1 = \frac{\Delta L}{\dot{S}} \quad ; \quad \Delta T_2 = \frac{\Delta \chi}{\dot{\chi}} \quad ; \quad \Delta T_3 = \tau_D$$

where $\dot{S}$ is the rate at which the path becomes illuminated, $\Delta \chi = \chi_{THR} - \pi/2$, $\dot{\chi}$ is the rate of change of solar zenith angle, and τ_D is the daytime ionospheric response time (see Chapter 2).
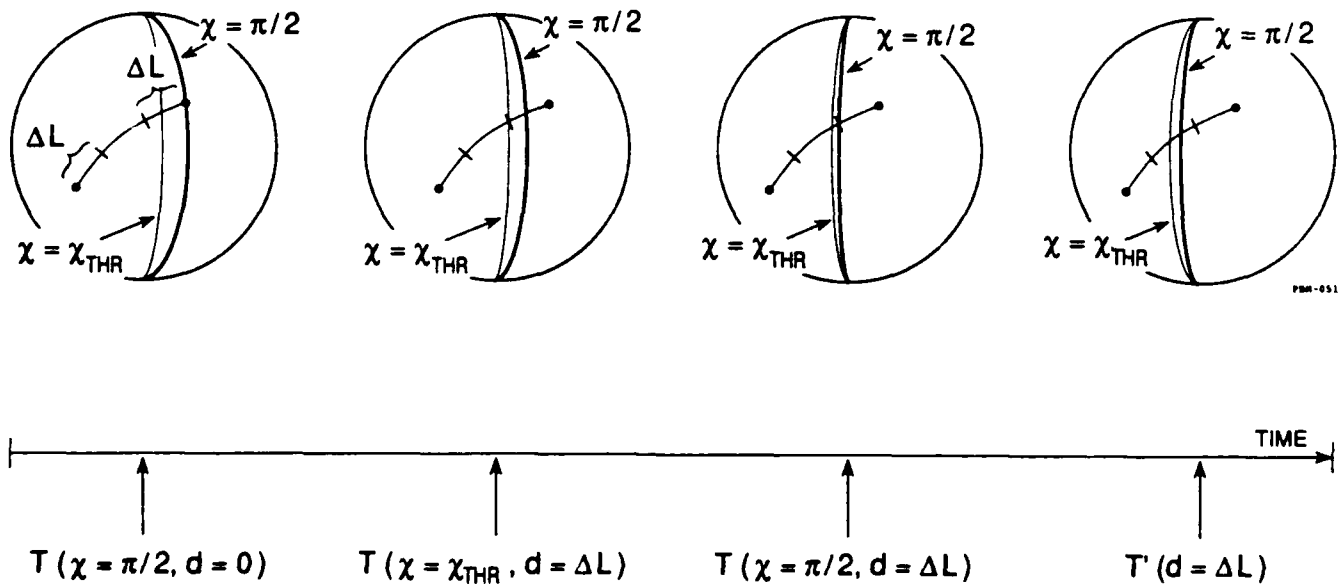

Figure 4.4-1   Time Sequence Leading to Sunrise Onset from Reference
Time Epoch (Solar Zenith Angle, χ, is $\pi/2$ at Transmitter)

4-11

To account for the uncertainty in these parameters and to provide for comparison with observations, calibration parameters C_L, C_χ, and C_τ are inserted as follows:

$$\Delta T = C_L \frac{\Delta L}{\dot{S}} + C_\chi \frac{\Delta \chi}{\dot{\chi}} + C_\tau \tau$$

Observations of path sunrise onset time can thus lead to estimates of the calibration parameters C_L, C_χ, and C_τ since the quantities $\dot{S}$ and $\dot{\chi}$ near the time of onset are easily computed. Moreover, with the use of default values of ΔL, χ_{THR}, and τ, the numerical estimates of the calibration coefficients are equivalent to estimates of the true values of ΔL, χ_{THR}, and τ. The coefficients C_L, C_χ, C_τ can be specified separately for first (near transmitter)/last (near receiver) points of ionospheric interaction and sunrise/sunset. If reciprocity is, as expected, approximately valid, then the coefficients should be the same for the first/last point of ionospheric interaction but the sunrise and sunset values are, in any case, likely to be different.

Once the onset/recovery time parameters are calibrated, the day and night coefficient calibrations can be refined using *all* the hourly data available. This will permit a more precise calibration of all unknown parameters and thereby provide more accurate predictions.

4.5 COMPARISON OF 1980 AND 1990 PPC MODEL STRUCTURE

The 1980 and 1990 PPC models are both based on a waveguide-mode model of wave propagation and employ a path segmentation scheme for both temporal and spatial sub-model contributions to the phase. As a result, the models are similar in many respects but there are important and even fundamental differences which are briefly described in this section.

Table 4.5-1 summarizes the principal distinctions between the two model structures by comparing the temporal and spatial sub-model features and the overall model structure. The following three sub-sections amplify the comparison between the two model structures given in the figure.

4.5.1 Diurnal Sub-model Comparison

Both models rely on solar zenith angle as the principal time-dependent variable for temporal phase variation. The 1980 model (Ref. 3) uses an empirically-based piecewise linear (three linear forms connecting phase variation and $\cos \chi$) diurnal function which prescribes an

Table 4.5-1 Comparison of 1980 (Current) and 1990 (Proposed) PPC Model Structure

	1980 MODEL	1990 MODEL
Diurnal	Piecewise linear interpolation function Transition dynamics based on linear electron loss Sunrise/sun set dump schedule	Day model based on Chapman theory Night model based on Lyman-alpha scattering Accurate prediction of onset/recovery times by use of calibratable parameters
Geomagnetic/ Conductivity	Correlated analytic magnetic forms Uncoupled conductivity forms Possible erroneous Mode 1 behavior on certain azimuths near equator	Coupled magnetic/conductivity forms Mix of independent analytic & tabular forms Mode 1/Mode X behavior specified in equatorial region
Overall Structure	Interpolation of spatial forms between night/day using piecewise linear diurnal function Calibration using all-day or all-night paths Day data constructed using previous calibration parameters	Evolution functions describe time behavior of spatial sub-models Data from all hours used for calibration Cyclical calibration involving day/ night spatial parameters and onset/recovery time parameters

unchanging phase variation at nig.it ($\chi \geq 98°$). The 1990 model employs a Chapman theory-based phase variation with solar zenith angle which applies during the period when solar photo-ionization controls the effective reflection height of the ionosphere. The two prediction methods yield similar results for $\chi - 0$ but can differ markedly for larger χ.

For $\chi \geq 70°$ on a path segment, the 1980 model invokes a "dynamic" phase variation resulting from a differential equation analogous to an ionosphere continuity equation with a linear

loss term*. Sunrise and sunset schedules of electron "dumping" are also invoked in the 1980 to account for excess ionization by minority ionospheric constituents. The temporal functional form used in the 1990 model embodies changes from a simple $\log_e \sec \chi$ behavior to a steeper, more complex form (i.e., Chapman Function begins accounting for a curved ionosphere) for $\chi \geq 70°$. No dump schedules are included in the 1990 model because the observed phase variation ascribed to anomalous electron dumps does not warrant the complexity of their inclusion in the prediction model. The 1990 diurnal sub-model focuses on predicting a particular set of time parameters to which phase prediction error is especially sensitive: sunrise/sunset onset/recovery times. Parameters are identified in the 1990 sub-model which are used to accurately compute the onset/recovery times.

As mentioned above, the 1980 model predicts a fixed phase variation for $\chi \geq 98°$, i.e., no change in predicted nighttime phase. The 1990 model includes a nighttime variation with solar zenith angle based on satellite observations of scattered Lyman-a radiation. The 1980 model also contains a long-term (year-dependent) functional form which is being investigated under a separate effort (Ref. 16). The work described in this report does not address a long-term phase variation.

4.5.2 Spatial Sub-model Comparison

The 1980 PPC model contains separate, uncoupled spatial sub-models for: (1) geomagnetic latitude/bearing, (2) ground conductivity, (3) auroral zone, and (4) polar regions. The 1990 PPC model contains a single sub-model for geomagnetic latitude/bearing and ground conductivity which accounts for the known coupling between these two categories of spatial parameters. Modification of the auroral and polar sub-models is not addressed in the work described by this report so that these two sub-models are currently planned for inclusion into the 1990 model in their present form. The 1980 geomagnetic latitude/bearing sub-model contains functional forms which are highly correlated while the 1990 geomagnetic/conductivity sub-model contains essentially independent, uncorrelated functional forms. All functional forms of the 1980 sub-models are analytic forms (including the constant, unity) whereas the 1990 geomagnetic/conductivity sub-model contains a mix of analytic and tabular functional forms to minimize the complexity, increase the accuracy, and facilitate the calibration of the model. The 1980 geomagnetic/bearing sub-model specifies functional forms on certain nighttime low-latitude,

---

*Current models of D/E region ionization dynamics include a quadratic loss term as indicated in Eq. 2.2-3.

westerly-directed path segments which may implicitly model the behavior of a higher-order mode (Mode X see Chapter 3). The 1990 geomagnetic/conductivity sub-model includes two sets of candidate functional forms which permit selection of the correct propagation model(on night-time path segments within the appropriate range of geomagnetic bearing and latitude) using the observed data.

4.5.3 Overall Model Structure Comparison

Both the 1980 and 1990 PPC models use an interpolative scheme to combine the spatial and temporal sub-models but with important individual differences. The 1980 model uses an empirically-derived diurnal function (modified by the "dynamic" diurnal function under local transition conditions) which is piecewise-linear in cos χ to interpolate *all* spatial functional forms between their daytime and nighttime levels (as given by the calibration coefficients). Thus, the phase variation at a path segment (ignoring transition and dump schedule contributions) is given by

$$\Delta\phi = \sum_j C_j^D F_j + \sum_j f(C_j^N - C_j^D)F_j \qquad \text{(1980 model)} \qquad (4.5\text{-}1)$$

where $C_j^N(C_j^D)$ are the calibration coefficients for nighttime (daytime) corresponding to the jth functional form, F_j, and the sum is over all spatial functional forms. The diurnal function, f, is one for nighttime conditions and decreases through two types of linear functions of cos χ to a value of zero at normal illumination (sun directly overhead). Those functional forms which apply to daytime only are selected by taking $C_j^N = 0$. Thus, the predicted phase variation for *daytime-only* forms is (from Eq. 4.5-1)

$$\Delta\phi = \sum_{\substack{\text{DAY} \\ \text{ONLY}}} \sum_j C_j^D(1-f)F_j \quad \text{(sum over day-only forms)}$$

which gradually decreases in magnitude as χ increases until nighttime (f=1) is achieved at which $\Delta\phi = 0$. Similarly, those functional forms defined for *night only* are selected by taking $C_j^D = 0$. In this case, the predicted phase variation is (from Eq. 4.5-1)

$$\Delta\phi = \sum_{\substack{\text{NIGHT} \\ \text{ONLY}}} \sum_j C_j^N f \, F_j \qquad \text{(sum over night-only forms)}$$

The above form is zero only for f=0 (sun directly overhead) but for all other values of χ it is non-zero. This means that the functional forms specified for nighttime-only are invoked for

virtually all local daytime conditions (amplitude of the contribution increasing with increasing χ) as well as nighttime conditions.

The 1990 PPC model avoids this difficulty by specifying three separate evolution functions depending on the temporal domain of definition for the functional form: (1) daytime-only (2) nighttime-only and (3) daytime *and* nighttime. In each case, the actual form of the variation is based on either the Chapman photoionization model (daytime) or scattered Lyman-a radiation (nighttime) but the forms are displaced/normalized so as to apply only in the appropriate temporal domain.

The 1980 PPC model is structured to be calibrated using data recorded only on signal paths which are either all-day or all-night. Data on transition paths are not used in the calibration since no calibration coefficients appear in the diurnal function (or "dynamic" diurnal function). This means that large observed errors on transition paths will not be corrected by the usual process of coefficient calibration. Daytime data is modified (using an earlier set of calibration coefficients) by subtracting the time-dependent component of the predicted phase prior to the conventional daytime calibration procedure. Since the time-dependent portion depends on the *old* calibration coefficients, a cyclical procedure is indicated but not normally carried out. Because the diurnal function, f, is one at night, the nighttime coefficient calibration requires no *a priori* data modification.

The 1990 model invokes a 3-step calibration cycle in which the daytime coefficients are first calibrated from data on paths limited to a certain range of χ. In the second step, nighttime coefficients are also calibrated on paths limited to a certain range of χ. The limitation on χ in the first two steps is primarily due to the need to reduce the sensitivity of the terms multiplying the calibration coefficients to the onset/recovery time parameters (in particular, χ_{THR}) assumed. The third step is the calibration of the onset/recovery time parameters using analog data from which sunrise/sunset onset/recovery times are extracted. Comparison of the calibrated onset/recovery time parameters with default values will determine the revised range of χ allowed for paths used in the second cycle of daytime/nighttime coefficient calibration. Once stable values of the onset/recovery time parameters are obtained, calibration of the daytime and nighttime coefficients can be performed using data on paths with any range of solar zenith angle. This means that a well-balanced set of data on all paths and at all times is used to calibrate the model.

4.6 SUMMARY

The model structure developed in this report specifies a means for combining the spatial sub-model describing the phase changes due to local variations in geomagnetic/conductivity effects with the temporal dependence given in the diurnal sub-model. The functional forms for wave number/phase velocity and excitation-factor phase are defined for two temporal extremes: day ($\chi - 0$) and night ($\chi - \pi$). The physics-based diurnal forms (introduced in Chapter 2) are shifted/normalized (but retaining the same basic form) to serve as evolution functions which modify the spatial forms at intermediate values of solar zenith angle. Separate evolution functions are defined for three types of spatial functional forms: (1) day-only, (2) night-only, and (3) day/night.

Calibration of the model is carried out in a three-step cycle: (1) daytime coefficient calibration, (2) nighttime coefficient calibration, and (3) onset/recovery time calibration. Daytime coefficients are calibrated using data recorded at hours for which the maximum solar zenith angle is less than about 50° along the path. These coefficients are calibrated first because: (1) the predicted phase is, for the indicated range of solar zenith angles, approximately expressed in terms of daytime coefficients, and (2) daytime (midday) phase is usually inherently stable and repeatable. Nighttime coefficients are calibrated next using data recorded at hours in which the path solar zenith angles are in some appropriate range so that the predicted phase is essentially independent of solar zenith angle for default values of the sunrise/sunset onset/recovery time parameters. In the third step, the onset/recovery time parameters, which include: (1) distance to first/last point of ionospheric interaction, (2) threshold solar zenith angle, and (3) day/night ionospheric response times, are calibrated from analog phase measurements of onset/recovery times. Once the onset/recovery time parameters are established, the calibration cycle can be repeated without limitation on the path range of solar zenith angle.

5.   SUMMARY, CONCLUSIONS, AND RECOMMENDATIONS

The development and structure of the 1990 PPC model are summarized in the first section of this chapter. Conclusions are then presented regarding the physical processes addressed by the model, spatial/temporal coupling, accommodation of calibration data, and expected accuracy. The 1980 and 1990 PPC model structures are also compared. Finally, recommendations are made regarding sub-model refinement, additional sub-model development, and model calibration procedures/requirements.

5.1   SUMMARY

The development of the diurnal sub-model (presented in Chapter 2) represents, in many ways, a new approach to the prediction of temporal phase by focusing on physics-based modeling of the ionosphere and on those predictive features to which the phase error is most sensitive. The importance of computing correct sunrise/sunset onset/recovery times for phase prediction accuracy is demonstrated to motivate the analysis of parameters which determine these times. Background information on ionospheric physics is presented to provide a framework for the development of daytime and nighttime phase variation models. The daytime phase variation is developed using a Chapman model of photoionization dynamics to describe how the effective VLF wave reflection height varies with solar zenith angle. Effective reflection height is related to phase variation to obtain the functional form for daytime phase variation. The nighttime ionosphere is not controlled directly by solar radiation so that other sources of ionization described in the literature are analyzed in terms of their relative dominance. Solar Lyman-alpha radiation resonantly scattered from the earth's geocorona is the dominant nighttime ionization source and satellite measurements of Lyman-alpha intensity indicate a solar zenith-angle dependence and sufficient flux to ionize the nighttime D/E-regions. The nighttime phase variation is determined by using an approach similar to Chapman's development of electron production in the ionosphere. Parameters defining sunrise/sunset onset/recovery times are described in terms of ionospheric properties and wave propagation features. Results of a path/time phase prediction computation (using only diurnal forms) are compared with observed data.

The geomagnetic/conductivity sub-model is a fully coupled characterization of the phase variation due to spatial variations in the earth's magnetic field, signal propagation direction, and

conductivity of the earth's surface. This is the only spatial sub-model treated herein; other spatial sub-models, such as those specifying phase variation over the auroral zones and polar regions, are not addressed in the work covered by this report. The spatial phase variation is separated into two components: (1) a path length-dependent part known as the wave number or phase velocity component and (2) a path length-independent part referred to as the excitation factor phase component. The waveguide-mode model treats the total signal field as a sum of independent signal modes, each with its own amplitude and phase. By design, the PPC model predicts only the phase components of the Mode 1 signal. These components are computed from full-wave waveguide-mode models in terms of geomagnetic latitude, path bearing (with respect to geomagnetic north), and ground conductivity for both day and night for each of the three frequencies, 10.2, 11-1/3, and 13.6 kHz. Functional forms are developed from plots of the theoretical phase components (as a function of each spatial parameter) and other considerations. For geomagnetic latitudes less than 10 degrees, phase component behavior is very complex so that tabulated functions are substituted for analytic functional forms. Linear combinations of functional forms are fit to the theoretical phase component behavior by means of calibration coefficients. At low geomagnetic latitiudes and within a certain range of geomagnetic bearings, the identity of the Mode 1 signal is somewhat obscure. As a result, two candidate forms (tabular) are developed for the nighttime phase components in this limited region of parameter space which approximate the two alternative behaviors for Mode 1. Selection of the correct alternative is possible through separate calibration of each candidate functional form using observational data.

In synthesizing the spatial and temporal sub-models into an overall model structure, the basic assumption is made that, although the diurnal scaling of the individual spatial functional forms is different, their *evolution* in changing solar zenith angle from day to night (or night to day) has the same functional behavior (given by the evolution functions) for all spatial functional forms. Evolution functions are developed for functional forms defined within three temporal domains: (1) daytime-only, (2) nighttime-only, and (3) both day and night. The evolution function for a given temporal domain is obtained from the phase behavior developed for that temporal domain. The expression for the predicted phase and PPC is written using the defined evolution functions to drive the solar zenith angle-dependence of the functional forms. The model structure suggests a three-step cyclical calibration procedure in which daytime coefficients are first calibrated using data from paths/times having an allowed range of solar zenith angle. In the second step, nighttime coefficients are calibrated using data from paths/times

having a different allowed range of solar zenith angle. The third step involves calibration of the onset/recovery time parameters using observed onset/recovery times from analog data. Once the onset/recovery times are established, the daytime and nighttime coefficients may be recalibrated using data on all path/times.

Comparison of the 1980 and 1990 PPC models indicates that, for the temporal dependence, the 1990 model daytime phase variation follows a Chapman-type behavior with solar zenith angle up to the day/night threshold value, thus excluding any special contributions from "transition" effects or sunrise/suset dump schedules included in the 1980 PPC model. The 1990 model predicted nighttime phase varies with solar zenith angle unlike the 1980 model in which the nighttime phase is fixed. The phase dependence on geomagnetic field (including signal propagation direction) and ground conductivity is coupled (as predicted by theory)in the 1990 model and uncoupled in the 1980 model. As a result of this coupling, the spatial functional forms (all analytic for the 1980 model and a mix of analytic and tabular for the 1990 model) for the two models are different. Because of the uncertain identity of Mode 1 in a certain range of low geomagnetic latitudes and westerly bearings, the 1990 spatial sub-model contains two candidate forms for Mode 1 behavior whereas the 1980 model assumes that only one of the forms characterizes Mode 1 behavior. The 1980 PPC model uses a diurnal function, piecewise linear in cosine of solar zenith angle, as a means of combining spatial and temporal forms. In addition, a "dynamic" contribution and sunrise/sunset "dumps" are added during transition conditions. The 1990 model uses evolution functions for spatial functional forms defined for three temporal domains to combine spatial and temporal forms. Finally, the 1980 model is structured for calibration using data from day-only and night-only paths whereas the 1990 model may be calibrated (via a three-step, cyclical procedure) using data from mixed (day/night) as well as day-only and night-only paths.

5.2   CONCLUSIONS

The structure of the 1990 PPC model presented in this report should be used as the basis for a fully calibrated phase prediction model/algorithm to support the operational needs of Omega users worldwide. The features of this semi-empirical model are:

- A strong adherence to physical models of the D/E-region ionosphere and VLF signal propagation
- Specific focus on those temporal/spatial aspects of the model to which phase prediction accuracy is most sensitive

- A model structure which is amenable to calibration using all path data collected on a 24-hour basis

- A model structure which guarantees correct temporal invocation of appropriate spatial functional forms

- A minimal number of independent spatial functional forms which couple appropriate geophysical parameters and accurately fit theoretical computations.

A fully operational, properly calibrated model based on the structure described herein is expected to provide substantially improved phase corrections. This expected improvement is based on a comparison of the 1980 and 1990 PPC models in terms of underlying physical models, expected phase prediction accuracy during sunrise/sunset, and adaptibility to calibration by available observational data. The potential improvement is limited by the fact that the current auroral and spatial sub-models and the long-term time behavior are not addressed in the work covered by this report. Although the structure of auroral and polar sub-models is not analyzed, the pertinent geophysical parameters contributing to the phase variation for these sub-models is not expected to couple significantly to the parameters of the spatial sub-model considered in this report. As noted earlier, the long-term phase dependence is not addressed in the work covered by this report. The nature of the long-term phase dependence is the subject of a separate effort (Ref. 16) and its effect on the eventual performance of the model is not known.

5.3 RECOMMENDATIONS

The current work reported herein does not address the revision/modification of the auroral/polar sub-models. It is recommended that these sub-models be analyzed in light of current knowledge of polar/auroral ionospheres and magnetosphere/ionosphere interaction. Upgrade of these semi-empirical sub-models to a synoptic-type sub-model (one depending on near-real time inputs) should also be investigated.

The 1980 PPC model does not contain an equatorial sub-model (separate contribution to phase variation in the geomagnetic equatorial region). However, large phase prediction errors observed on transequatorial paths suggest the need for such a sub-model. It is recommended that the need for, and the physical basis of, such a sub-model be investigated.

The 11 1/3 kHz calibration coefficients and tabular functional forms are determined only for conductivity level 10 since a separate conductivity sub-model, *per se*, is not specifically

addressed in the work reported herein. It is recommended that the 11 1/3 kHz calibration coefficients and tabular functional forms for the geomagnetic/conductivity sub-model be computed for the five important (in terms of phase variation sensitivity) conductivity levels.

Pending a decision on the "other" sub-models (auroral, polar, equatorial, and long-term time dependence), *it is recommended that the 1990 model structure presented in this report be calibrated with recent years' three-frequency data on effectively "one-way" paths.* To provide observability of all sub-model functional forms, phase difference data on appropriate paths may also be required. Following calibration, the model should be tested and compared with the 1980 PPC model on an independent database. Finally, the model calibration, testing, comparison with the 1980 model, and operational description should be documented.

APPENDIX A
CHAPMAN FUNCTION APPROXIMATIONS

The Chapman Function is important in the quantitative description of ionospheric dynamics. Some characteristics and an approximate analytic expression for this function are given in this appendix.

The Chapman Function evaluated at a point P is defined (Ref. 7) as

$$Ch(x, \chi) = \frac{\tau(h, \chi)}{\sigma n(h) H} = \frac{1}{n(h) H} \int_h^\infty n \, ds \qquad (A-1)$$

where $\tau(h, \chi)$ is the optical depth at point P which is at altitude h above the surface of the earth. χ is the corresponding solar zenith angle at point P, σ is the absorption cross section for incident solar radiation. $n(h)$ is the neutral density at altitude h. H is the (assumed constant) scale height. ds is a differential element of path length along which a beam of radiation travels, and x is defined by

$$x = \frac{R_E + h}{H}$$

where R_E is the mean radius of the (assumed spherical) earth. For small values of χ, the curvature of the ionosphere (which follows the curvature of the earth) can be safely neglected and the Chapman Function is adequately approximated by $\sec \chi$. However, for larger values of solar zenith angle satisfying

$$x(1 - \sin\chi) \geq 81 \qquad (A-2)$$

the $\sec \chi$ approximation is no longer valid and the curvature of the earth must be taken into account. For typical values encountered in VLF signal propagation and modeling (Ref. 7), $x \cong 1290$ and the solar zenith angle corresponding to the equality in Eq. A-2 is about 69.6°.

Thus, for $\chi \geq 69.6°$, Eq. A-1 must be used to compute the Chapman Function. If the neutral density is assumed to decrease exponentially with height (exactly true for an ideal, isothermal gas of neutral particles), then Eq. A-1 can be approximately integrated (Ref. 7) to yield

$$Ch(x, \chi) \cong \left(\frac{1}{2}\pi x \sin\chi\right)^{1/2} e^{(x\cos^2\chi)/2} \left\{1 \pm erf\left[\left(\frac{1}{2}x\cos^2\chi\right)^{1/2}\right]\right\} \qquad (A-3)$$

A-1

where the + sign is used for $\chi > \pi/2$ and the − sign is used for $\chi < \pi/2$.

Equation A-3 is the form used for computing the Chapman Function in the path/time computer program which calculates the diurnal phase variation for VLF signals in the 10-14 kHz range.

APPENDIX B
OBSERVATIONAL PHASE DATA

This appendix describes the diurnal characteristics of Omega signal phase data in analog format received from the U.S. Coast Guard Omega Navigation System Center. These data were analyzed to obtain information used in developing and testing a new propagation correction (PPC) model.

Section B.2-1 presents a description of the phase data analyzed and a summary of the qualitative diurnal features distilled from the data. Section B.2-2 treats a selected sample of observed data and explains certain diurnal features, e.g., onset and recovery times of phase changes due to path sunrise/sunset. Sample comparisons of observed and predicted onset/recovery times are presented in Section B.3. This section also describes the dependence of the predicted onset/recovery times on specific signal propagation/ionospheric parameters.

B.1 PROCEDURES AND PRINCIPAL FEATURES OF DATA ANALYSIS

Analog phase data, recorded on effectively "one-way" Omega signal paths, were examined to identify the following time-dependent features:

- Sunrise onset/recovery time
- Sunset onset/recovery time
- Qualitative behavior of phase on all-day paths
- Qualitative behavior of phase on all-night paths
- Time of minimum phase level for path day
- Diurnal shift
- Any other time-dependent phase behavior characteristics.

Some of this data is used to develop functional forms describing time-dependent phase behavior for the 1990 PPC Diurnal Sub-model. Other data are used to test/verify phase predictions of this sub-model.

The analog data analyzed were recorded at monitor sites co-located with Omega transmitting stations. In addition to the phase of the local station signal, each station monitor records the phase of:

- Six other station signals in digital format (a weak/poor station signal is chosen as a calibration channel)
- Four other station signals in analog format (the station signals used in system synchronization)

at each of three frequencies: 10.2, 11-1/3, and 13.6 kHz. Table B.1-1 is a matrix indicating the paths (defined by a transmitting station and receiver) on which analog data is recorded at the three frequencies. Table B.1-2 gives the WGS 72/84 coordinates (geodetic latitude and longitude) of each transmitting station and its associated station monitor.*

Although no precise† standard time/frequency signal is fed directly into the monitor receiver, the data is *effectively* "one-way" phase since the phase of each of the four "remote"

Table B.1-1 Inter-station Paths (defined by transmitting station and receiver) on which Analog Data is Recorded

TRANSMITTING STATION MONITOR RECEIVER	A	B	C	D	E	F	G	H
A		X	X		X			X
B	X			X	X	X		
C	X			X			X	X
D		X	X			X		X
E	X	X				X	X	
F		X		X	X		X	
G			X		X	X		X
H	X		X	X			X	

*A station monitor is located approximately 1-2 Omega signal wavelengths from the transmitting antenna which is sufficiently far so that the radiated signal field component dominates the electrostatic and inductive field components and close enough so that no diurnal effect is seen (no appreciable ionospheric interaction).

†"Precise" means an accuracy of at least 1 part in 10^{11}, i.e., an offset of about one microsecond/day, so that the information constrained in diurnal traces in not obscured by oscillator drift problems.

station signals is referenced to the phase of the local station signal, which is essentially constant. Thus, the phase (modulo one cycle) of a given remote station signal is not the same as would be obtained by a receiver time-synchronized to the transmitted signal; the difference is just the cumulative phase developed between the local transmitting station and receiver antennas. Since this difference is fixed in time, however, analysis of the diurnal behavior (which does not depend on absolute phase values) is unaffected. The effective receiver time constant is adaptive, varying between 1 and 5 minutes, depending on the tracking error in the phase-lock loop.

The data is recorded on 8-channel chart paper with pre-printed hours (15-20 minute subdivisions) and phase values between 0.00 and 1.00 cycle (in subdivisions of 0.02 cycle (2 centicycles)). Chart speed is nominally 0.5 mm/minute but the drive motor is apparently not precisely controlled so that adjustments of several minutes are frequently made (and annotated on the chart) as often as twice per day. This means that the error in determining specific features, such as onset time, is limited to about one receiver time constant.

The analog data received from the U.S. Coast Guard Omega Navigation System Center (ONSCEN) consists of signal phase traces on the paths indicated in Table B.1-1, at the three frequencies (10.2, 11-1/3, 13.6 kHz) for certain months within the year 1988 (some 1987 and 1989

Table B.1-2 Transmitting Stations and Station Monitor Coordinates
for WGS 1972/1984 Spheroids

STATION	TRANSMITTING STATIONS		STATION MONITORS	
	LATITUDE (DEGREES)	LONGITUDE (DEGREES)	LATITUDE (DEGREES)	LONGITUDE (DEGREES)
A	66.42017/66.42019N	013.13681/013.13697E	66.52930/66.52932N	012.84530/012.84545E
B	06.30531/06.30535N	010.66455/010.66440W	06.42627/06.42631N	010.81398/010.81382W
C	21.40466/21.40470N	157.83098/157.83082W	21.52091/21.52095N	157.99658/157.99642W
D	46.36591/46.36594N	098.33.77/098.33562W	46.55950/46.55953N	098.63880/098.63865W
E	20.97418/20.97414S	055.28974/055.28990E	20.91194/20.91191S	055.51695/055.51710E
F	43.05358/43.05355S	065.19093/065.19078W	42.75328*/42.75325S	065.10094*/065.10079W
G	38.48126/38.48123S	146.93514/146.93530E	38.39556/38.39553S	146.66003/146.66018E
H	34.61470/34.61474N	129.45349/129.45365E	34.32471/34.32474N	129.20640/129.20655E

*Monitor moved in November 1988; previous WGS 1972 coordinates were:
Latitude = 43.22392° South; Longitude = 65.27159° West

data were also included). These years were selected to obtain representative, recent data recorded during periods of median solar activity. Analysis focused on 10.2 and 13.6 kHz data in September, since this month includes the autumnal equinox which is expected to provide a median seasonal component of phase behavior. The days selected include samples near the beginning, middle, and end of the month. A reduced sample of La Reunion data was analyzed since this station's annual maintenance is scheduled in September.

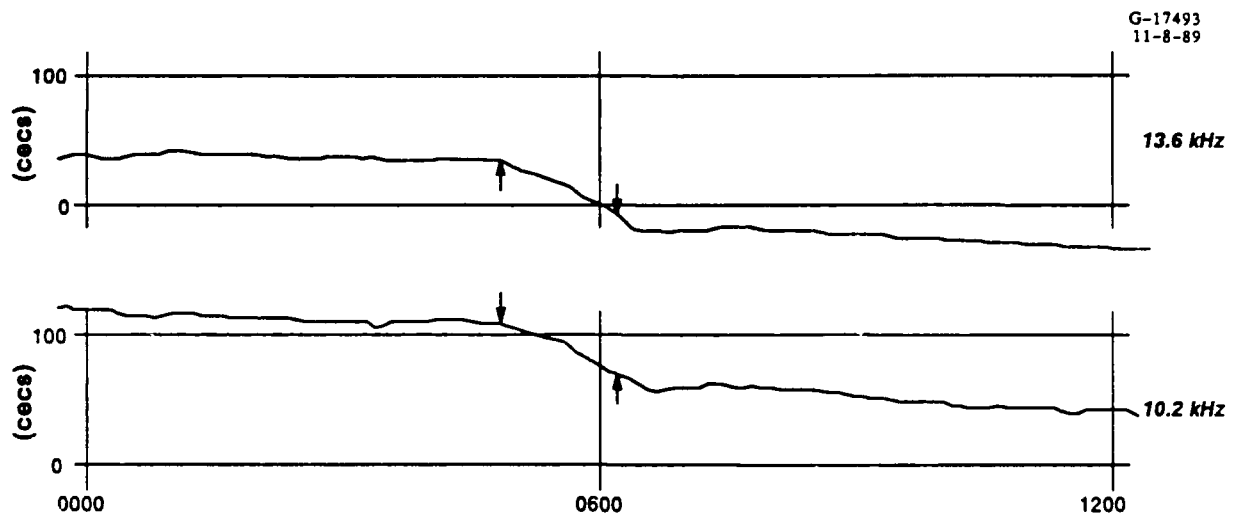The data analysis revealed the following features of the diurnal phase behavior:

- Due to external noise and other influences, onset/recovery times have a maximum identification accuracy of about 5 minutes; paths exhibiting very gradual phase onset/recovery may have substantially poorer accuracy

- Path sunset onset is usually a more gradual, less definite process than path sunrise onset

- The value of the phase at the sunrise recovery time generally differs from that at the sunset onset time; the same is true of the phase at sunset recovery time and sunrise onset time

- Depressions in the phase following sunrise recovery are occasionally found but are relatively small (less than 10 cecs)

- Because of the instabilities observed in the all-night period of the phase trace on certain paths (generally attributed to modal interference), corresponding path sunrise onset and sunset recovery times cannot be accurately determined during these periods

- Sunrise/sunset onset/recovery times are difficult to identify on paths exhibiting a double-diurnal effect.

The double-diurnal effect referred to in the last item refers to a characteristic doubly periodic phase behavior over a 24-hour period. This effect occurs in phase traces on paths in which the path *vertex* (i.e., the point of highest latitude on the path) is not one of the path segment endpoints. The effect is generally more apparent on paths in which the latitude of the path vertex exceeds the latitude of the terminator vertex (i.e., certain polar paths). The magnitude of the effect is diminished by the fact that the solar zenith angle changes relatively little over 24 hours on polar paths since the path is "close" to the earth's rotation axis. Figure B.1-1 illustrates the double-diurnal effect. The features described above are important to the development of the diurnal component of the 1990 r.C model and the methods used in its calibration.
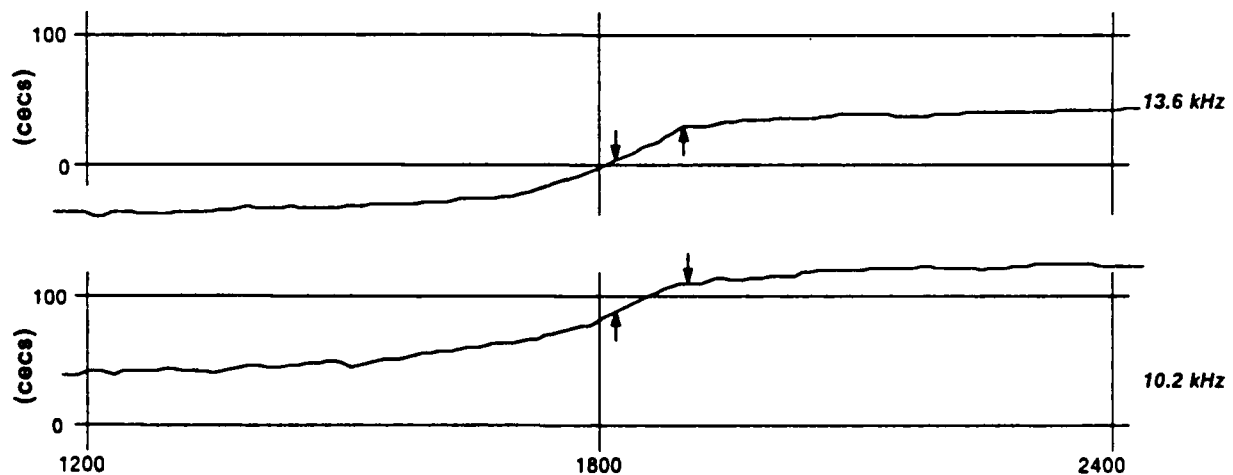
PATH DEFINED BY TRANSMITTER (T) AND RECEIVER (R)

Figure B.1-1 Illustration of Double-Diurnal Effect; North Polar View during Northern Hemisphere Summer

B.2 DESCRIPTION OF OBSERVED DATA SAMPLES

Although nearly 200 separate phase traces were analyzed in detail, only a fraction are presented here to illustrate the behavior of real phase data and to compare predicted and observed sunrise/sunset onset/recovery times. The six paths selected for illustration (three paths plus their near-reciprocals) have large north-south components to minimize the spatial/temporal coupling which is not addressed by the path/time program used to predict the onset/recovery times. Signals at two frequencies (10.2 and 13.6 kHz) are displayed for each path/time-segment to permit comparison.

Figure B.2-1 shows the observed phase traces of the 10.2 and 13.6 kHz signals on the path from the Liberia transmitting station to the Norway station monitor. Figure B.2-1(a) illustrates the first 12 hours of the UT day (which includes sunrise on this p⊃ᵗ⁻ ⁻ ⁿd Fig. B.2-1(b) illustrates the next 12 hours (including path sunset). The character.. _ _owl-shaped" daytime

*The paths are not exactly reciprocal since the transmitting antenna and monitor are separated by 20-50 km at a station. For a path length of approximately 7,000 km, however, the difference is small, so that the paths are very nearly coincident.

Figure B.2-1 10.2 and 13.6 kHz Phase Data from the Liberia Transmitter to the Norway Station Monitor on 26 September 1988

B–6

trace is noted between the hours of about 0600 and 1800 UT and a slight peak is observed on the nighttime trace near 2400 UT. A slight post-sunrise depression occurs on both 10.2 and 13.6 kHz. The arrows in the figures indicate the predicted onset/recovery times. For example, in Fig. B.2-1 (a) the arrow prior to 0600 UT designates sunrise onset and the arrow following 0600 UT denotes sunrise recovery. Similarly, the arrows in Fig. B.2-1(b) indicate sunset onset and recovery times. Note that sunset onset time is not so readily apparent as the other times; closer examination shows that this time separates the bowl-shaped daytime interval from the more linear path sunset period.

Figure B.2-2 displays the path reciprocal* to that described above, i.e., from the Norway transmitting station to the station monitor at Liberia. The phase behavior is similar to that of Fig. B.2-1 except for greater small-scale instability due probably to the greater local noise at the Liberia monitor. Note that the 13.6 kHz trace shows somewhat less irregularity than that for 10.2 kHz, likely because of the expected higher signal strength at 13.6 kHz.

The signal phase on the path from the Argentina transmitting station to the station monitor at North Dakota is shown in Fig. B.2-3. The phase trace during the first 12 hours of the UT day shown in Fig. B.2-3 (a) is highly oscillatory — the result of nighttime modal interference, characteristic of nighttime transequatorial paths having a westerly propagating component. Note the relatively fewer oscillations on the 13.6 kHz trace than the 10.2 kHz trace prior to 0600 UT, corresponding to less modal interference at this frequency. Onset/recovery times are shown in the figure, but are not particularly meaningful during periods in which modal interference is this severe. Note especially the single large oscillation following the predicted sunrise onset time. This oscillation probably results from modal conversion at the terminator and is not observed at sunset recovery — possibly because of the different path-terminator orientations at sunrise and sunset. Sunrise recovery at both frequencies, however, is cleanly predicted Figure B.2-3(b) shows primarily the daytime phase behavior which is much more stable than the nighttime phase behavior. This figure shows the asymmetry between sunrise recovery (beginning of all-day path) and sunset onset (end of all-day path).

Figure B.2-4 displays the reciprocal path, i.e., from the North Dakota transmitting antenna to the station monitor at Argentina. It is immediately evident from Fig. B.2-4(a) that little or no modal interference is observed on the phase of the signal propagated on the same path in the opposite direction (geomagnetic south and east). Nighttime and daytime (see Fig. B.2-4(b)) be-
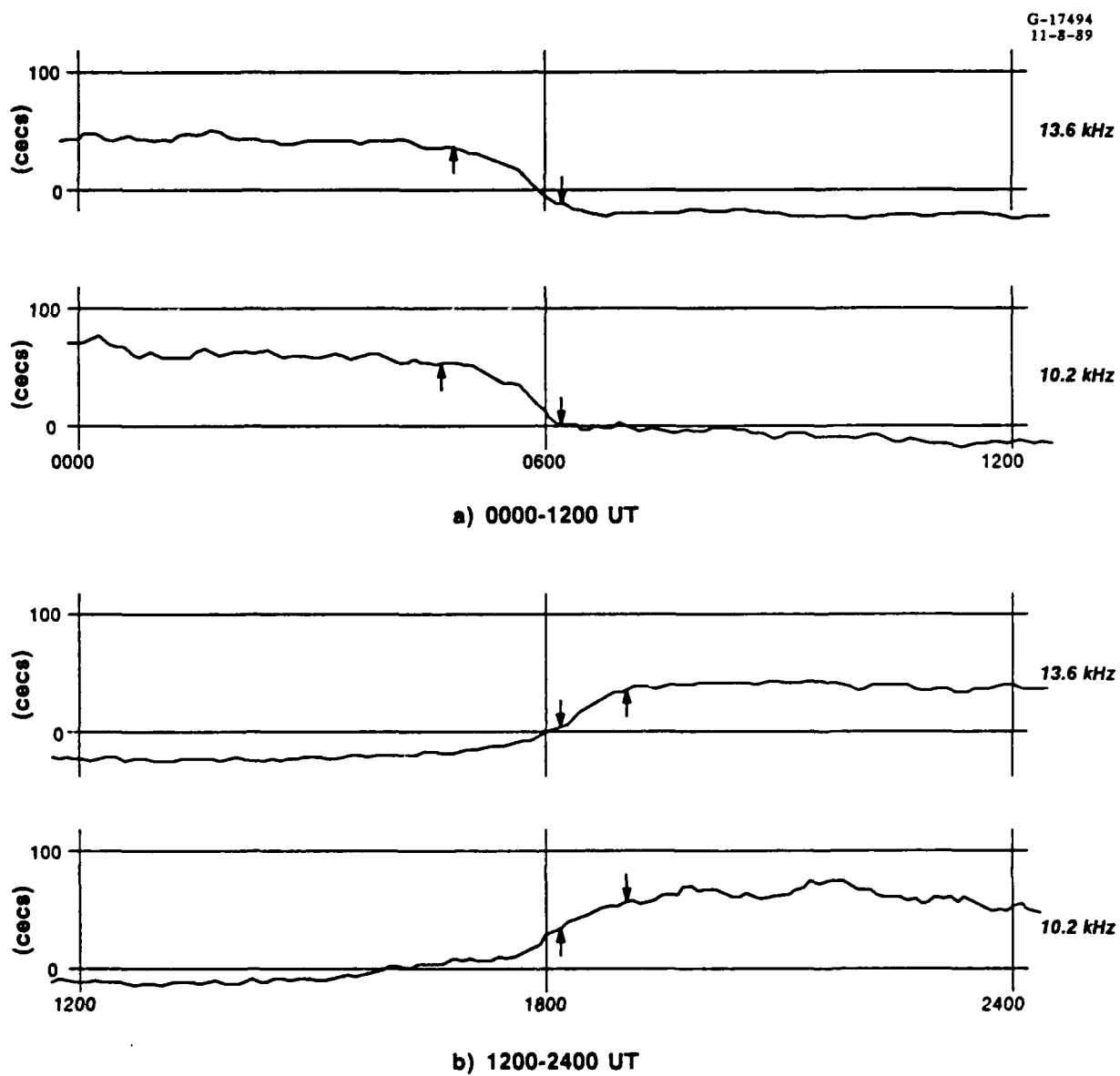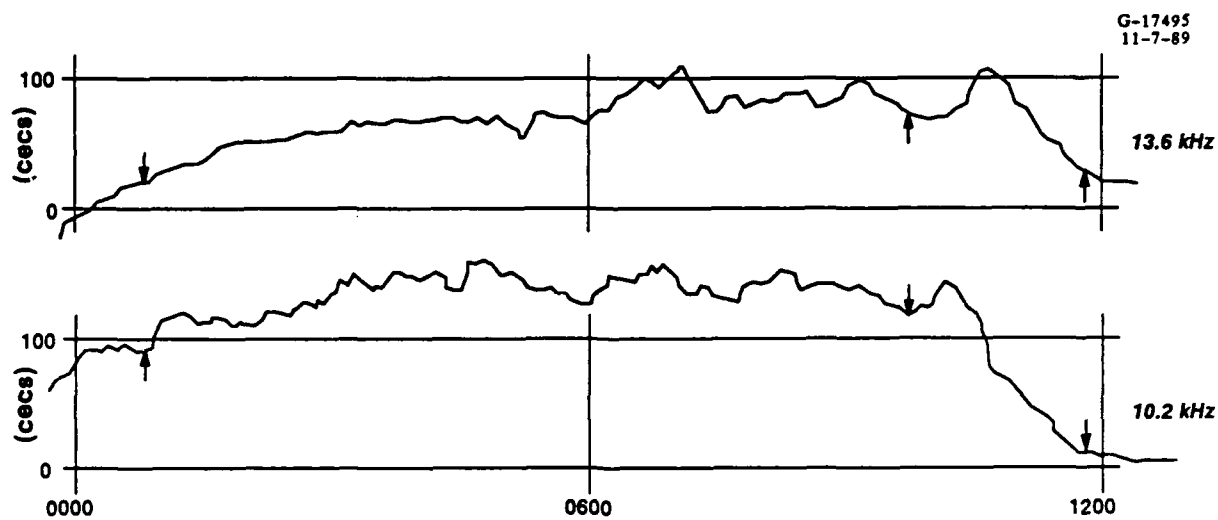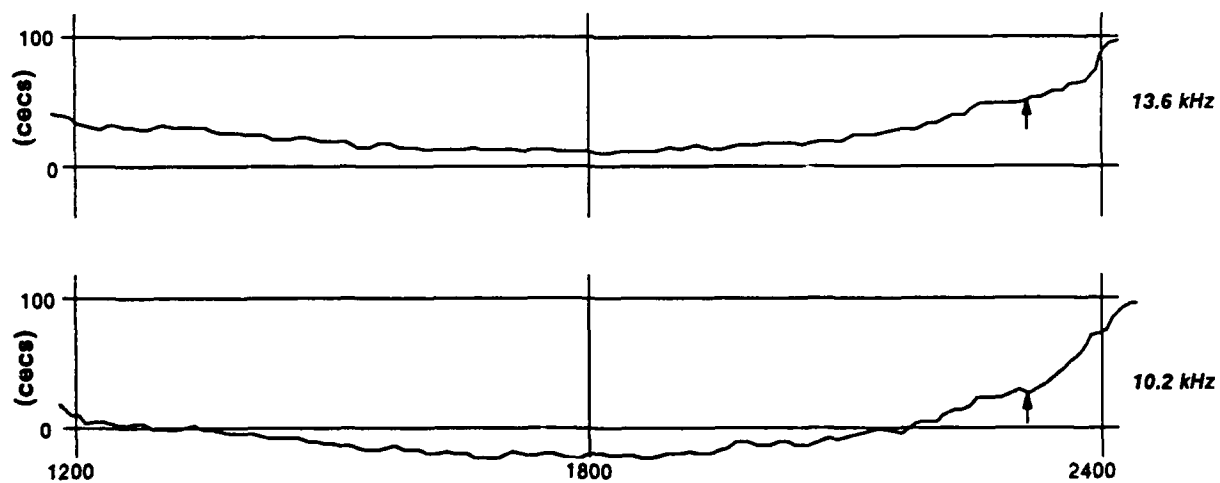
a) 0000-1200 UT

b) 1200-2400 UT

Figure B.2-2 10.2 and 13.6 kHz Phase Data from the Norway Transmitter to the Liberia Station Monitor on 25 September 1988
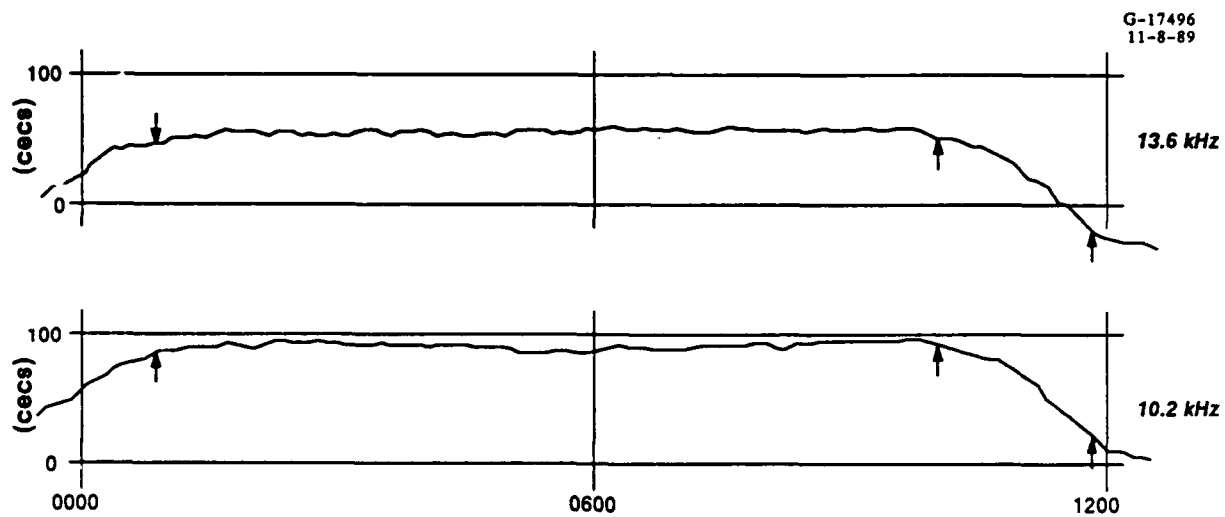
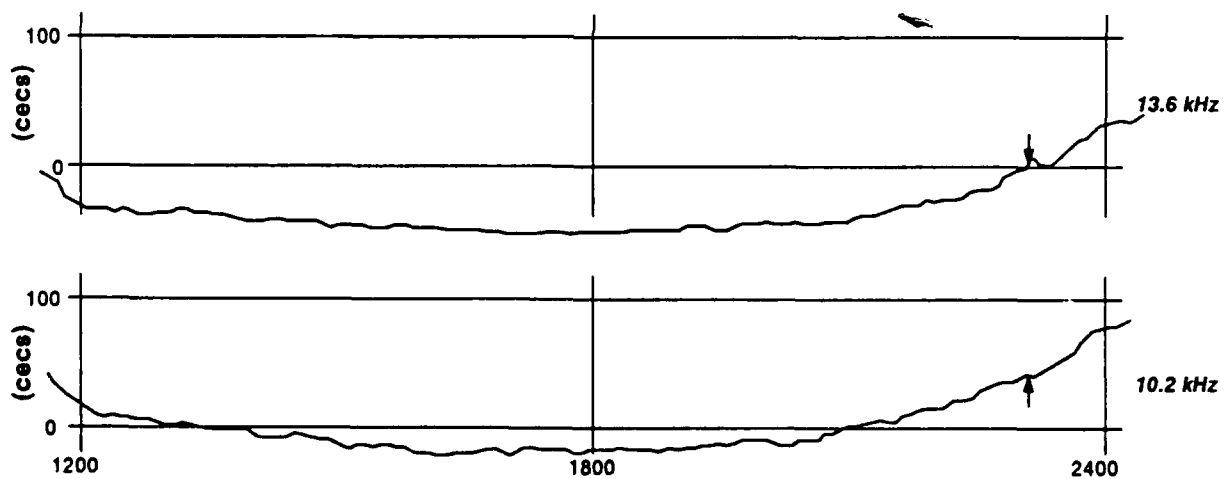**Figure B.2-3** 10.2 and 13.6 kHz Phase Data from the Argentina Transmitter to the North Dakota Station Monitor on 26 September 1988

a) 0000-1200 UT

b) 1200-2400 UT

Figure B.2-4 10.2 and 13.6 kHz Phase Data from the North Dakota Transmitter to the Argentina Station Monitor on 26 September 1988

havior is quite regular and the predicted onset/recovery times are consistent with the observations.

Phase behavior on the path from the Japan transmitting antenna to the station monitor at Australia is shown in Fig. B.2-5. The daytime and sunset periods of the phase traces are given in Fig. B.2-5(a). A distinguishing feature of the trace is the Sudden Ionospheric Disturbance (SID) occurring shortly after 0000 UT on both frequencies. The daytime and sunset phase behavior is otherwise quite normal. Fig. B.2-5(b) displays the nighttime and sunrise periods of phase behavior. The nighttime phase has a broad maximum between 1200 and 1800 UT.

Figure B.2-6 illustrates the phase behavior of the path from the Australia transmitting antenna to the station monitor in Japan, which is the reciprocal of the previously-described path. The SID noted earlier is also seen in Fig. B.2-6(a). The propagated signal on this transequatorial path has a westerly geomagnetic component and thus would be expected to exhibit modal interference. Figure B.2-6(b) shows a distinctive modal signature on the 10.2 kHz trace, especially near 1800 UT. Following 1800 UT, the phase trace exhibits a near cycle slip, recovering (in the correct cycle) just prior to sunrise recovery. In contrast, the 13.6 kHz phase trace is reasonably well-behaved, although a slight step is seen during path sunrise.

B.3 COMPARISON OF OBSERVED AND PREDICTED ONSET/RECOVERY TIMES

Table B.3-1 provides a comparison of observed and predicted sunrise/sunset onset/recovery times for the phase data described in Section B.2. The table provides a sample comparison only and should not be construed as an indicator of ultimate prediction accuracy.

Onset/recovery time prediction accuracy is difficult to measure because of the uncertainty inherent in identifying time of onset/recovery using the analog phase trace. In some cases, the identification is obscured by modal interference or noise. In other cases, however, identification problems arise because of no apparent change in phase behavior near the expected time. Identification errors also result from the assumed symmetry in the phase at sunrise recovery (beginning of all-day path) and sunset onset (end of all-day path). Both of these problems contribute to the large differences between observed and predicted sunset onset times shown in Table B.3-1. Comparison of predictions and observations, in addition to analysis of phase data on diverse types of paths, greatly improves identification accuracy.

Prediction of onset/recovery time is based on three principal elements:

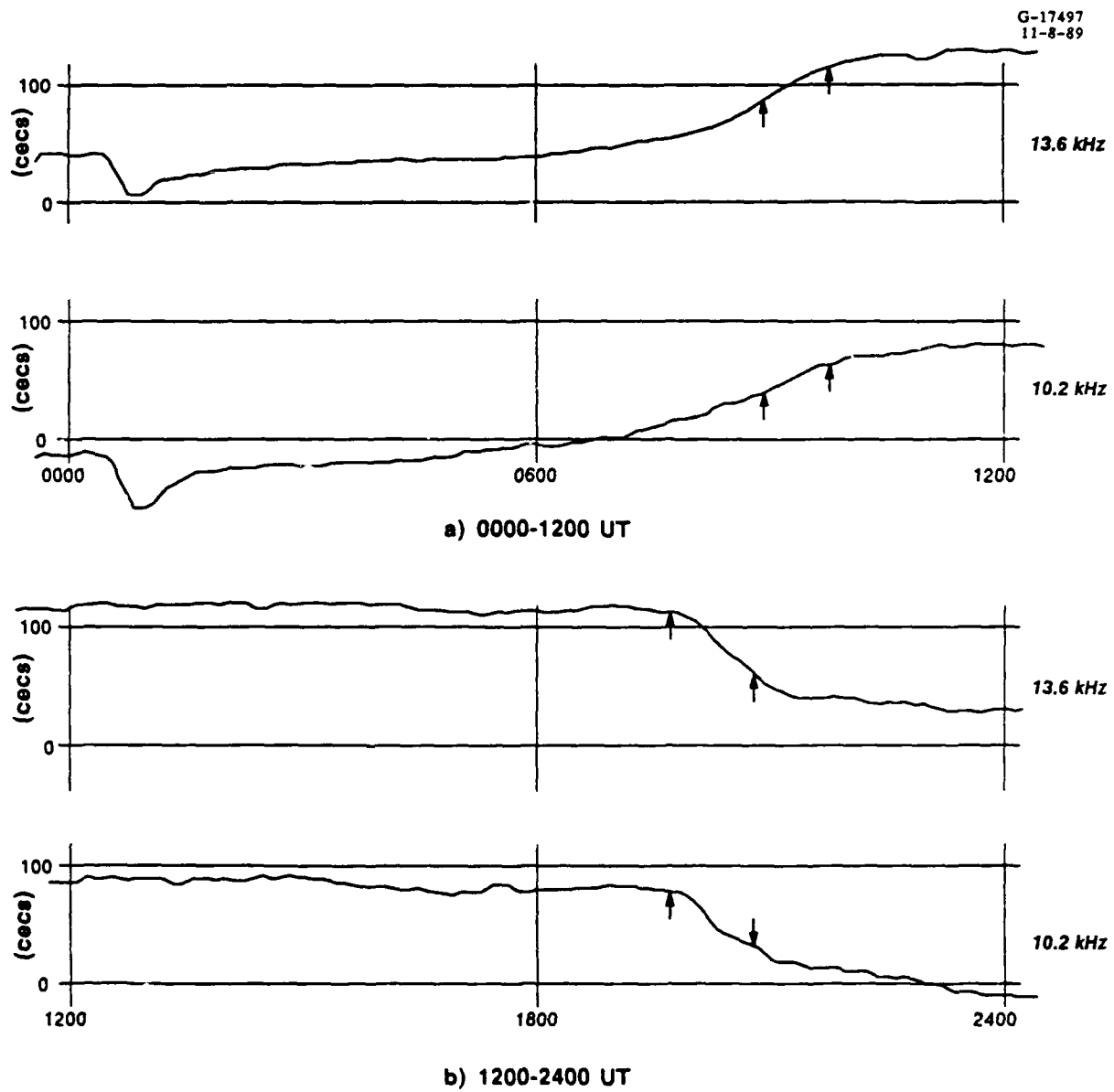**Figure B.2-5** 10.2 and 13.6 kHz Phase Data from the Japan Transmitter to the Australia Station Monitor on 25 September 1988
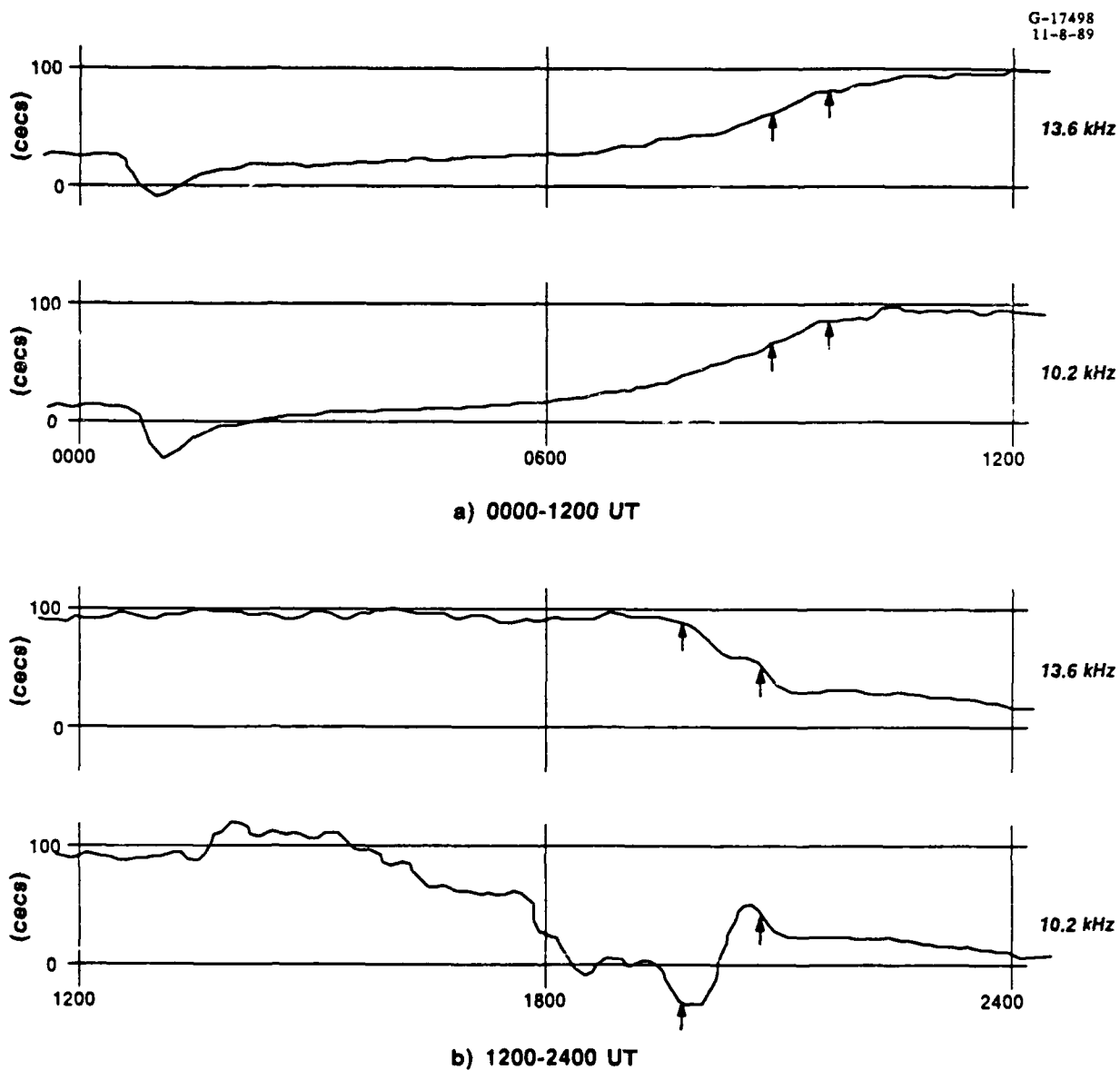
Figure B.2-6 10.2 and 13.6 kHz Phase Data from the Australia Transmitter to the Japan Station Monitor on 25 September 1988

Table B.3-1 Observed and Predicted Onset/Recovery Times for Sample Data

PATH*	FRQ. (kHz)	DATE	SUNRISE TIMES (UT) OBSERVED/PREDICTED		SUNSET TIMES (UT) OBSERVED/PREDICTED	
			ONSET	RECOVERY	ONSET	RECOVERY
B-A	10.2	26 SEP 88	0500/0454	0620/0612	** /1812	1900/1900
B-A	13.6	26 SEP 88	0455/0454	0620/0612	** /1812	1904/1900
A-B	10.2	25 SEP 88	0454/0448	0615/0612	1735/1812	1858/1900
A-B	13.6	25 SEP 88	0448/0448	0604/0612	1800/1812	1857/1900
F-D	10.2	26 SEP 88	** /0954	1156/1154	2305/2306	** /0048
F-D	13.6	26 SEP 88	** /0954	1155/1154	2225/2306	0200/0048
D-F	10.2	26 SEP 88	0950/1000	1200/1154	2315/2312	0102/0048
D-F	13.6	26 SEP 88	0940/1000	1157/1154	2312/2312	0043/0048
H-G	10.2	25 SEP 88	1930/1948	2100/2048	0825/0854	1005/0942
H-G	13.6	25 SEP 88	1938/1948	2104/2048	0815/0854	0937/0942
G-H	10.2	25 SEP 88	** /1948	2102/2048	0755/0854	0920/0942
G-H	13.6	25 SEP 88	1948/1948	2100/2048	0800/0854	1010/0942

* First letter indicates transmitter; second letter indicates station monitor receiver

** Measurement not recorded due to large uncertainty in identifying time

- Point of first/last interaction between the signal wave field and the ionosphere

- Solar zenith angle threshold separating direct solar control of the local ionosphere from control by nighttime sources

- Ionization response time of the local ionosphere following exposure to an ionization source.

These parameters can be varied to match the observed onset/recovery times. The predictions given in Table B.3-1 are based on default values of these parameters and thus are not "optimized." Also, the predictions are made at 6-minute intervals which are about 1-3 receiver time constants and comparable to the uncertainty in the time information derived from the analog charts.

Figures B.3-1 through B.3-3 show the sensitivity of onset/recovery times to each of the three onset/recovery time parameters listed above. The effect of varying the first/last point of ionospheric interaction is illustrated in Fig. B.3-1. Two traces are shown which differ in effective ionospheric path length by 2 × 0.14 radian = 0.28 radian (about 20% of the total path

OMSTA Australia at HAWAI Monitor (10.2 kHz) 05 Sep 88

Legend:

—— First/Last point of interaction = 0.15 radian from path end-points

--- First/Last point of interaction = 0.01 radian from path end-points

SSO Sunset Onset
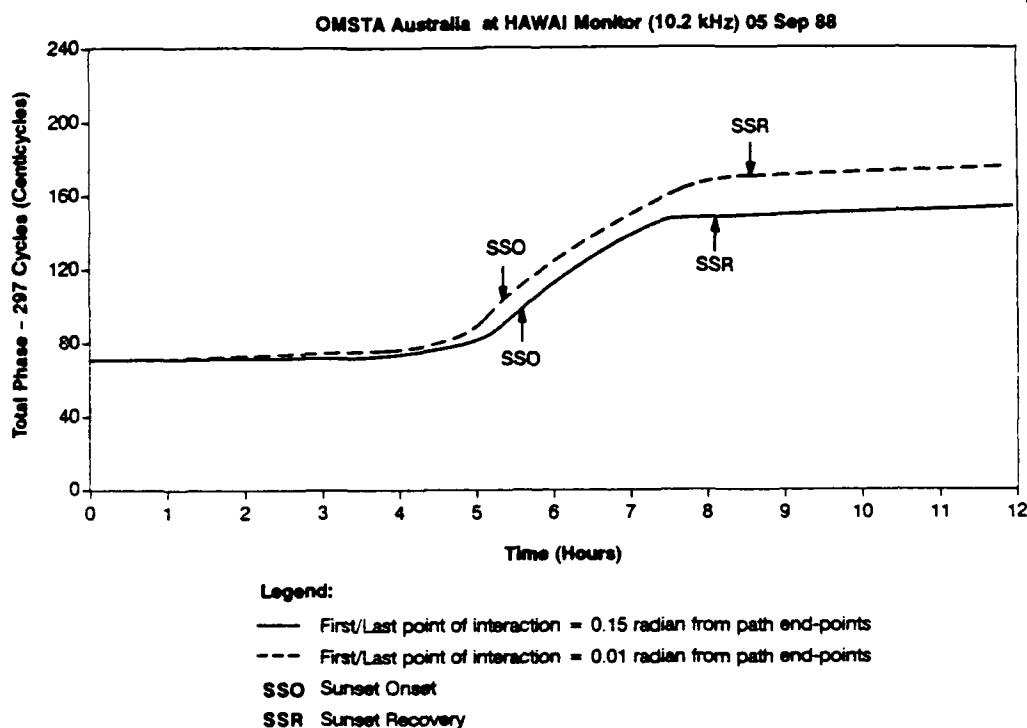
SSR Sunset Recovery

Figure B.3-1 Illustration of Effect of First/Last Point of Wave/Ionosphere Interaction on Diurnal Phase Behavior

length). Increasing the effective ionospheric path length on a path of fixed total length leads to earlier onset times and later recovery times as shown in the figure. Figure B.3-2 illustrates the effect of varying solar zenith angle threshold on diurnal phase behavior. The two traces displayed represent probable extremes in physically realizable solar zenith angle thresholds (91° and 100°). Larger solar zenith angle thresholds tend to shift both onset and recovery to later times as compared to smaller thresholds. In this case the effective ionospheric path length does not change in varying the thresholds, so that the diurnal shift is the same. Note the difference in phase level of the two traces in the all-day portion of the path; this is due to the dependence of the daytime evolution function on the solar zenith angle threshold. The effect of the different daytime and nighttime ionospheric response times is shown in Fig. B.3-3. The solid trace corresponds to an equal daytime and nighttime response time of six minutes while the dashed curve traces the diurnal behavior for the same daytime response time but a nighttime response of 66 minutes (Ref. 16). This day/night response time difference has the effect of delaying the sunset onset and recovery times (as shown) but little effect on the corresponding times for sunrise since the strong solar photoionization takes over rapidly from the weaker nighttime sources.
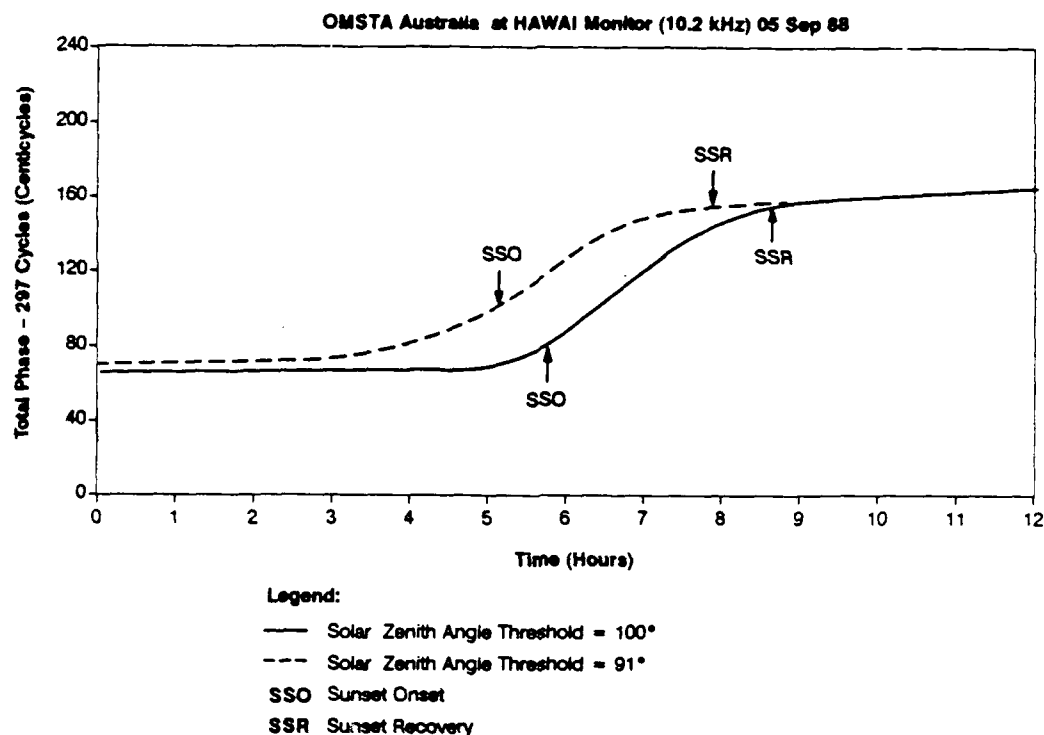
OMSTA Australia at HAWAI Monitor (10.2 kHz) 05 Sep 88

Legend:

— Solar Zenith Angle Threshold = 100°

--- Solar Zenith Angle Threshold = 91°

SSO Sunset Onset

SSR Sunset Recovery

Figure B.3-2 Illustration of the Effect of Solar Zenith Angle Threshold on Diurnal Phase Behavior

OMSTA Australia at HAWAI Monitor (10.2 kHz) 05 Sep 88

Legend:

— Daytime/Nighttime Response = 6 Minutes

--- Daytime Response = 6 Minutes ; Nighttime Response = 66 Minutes

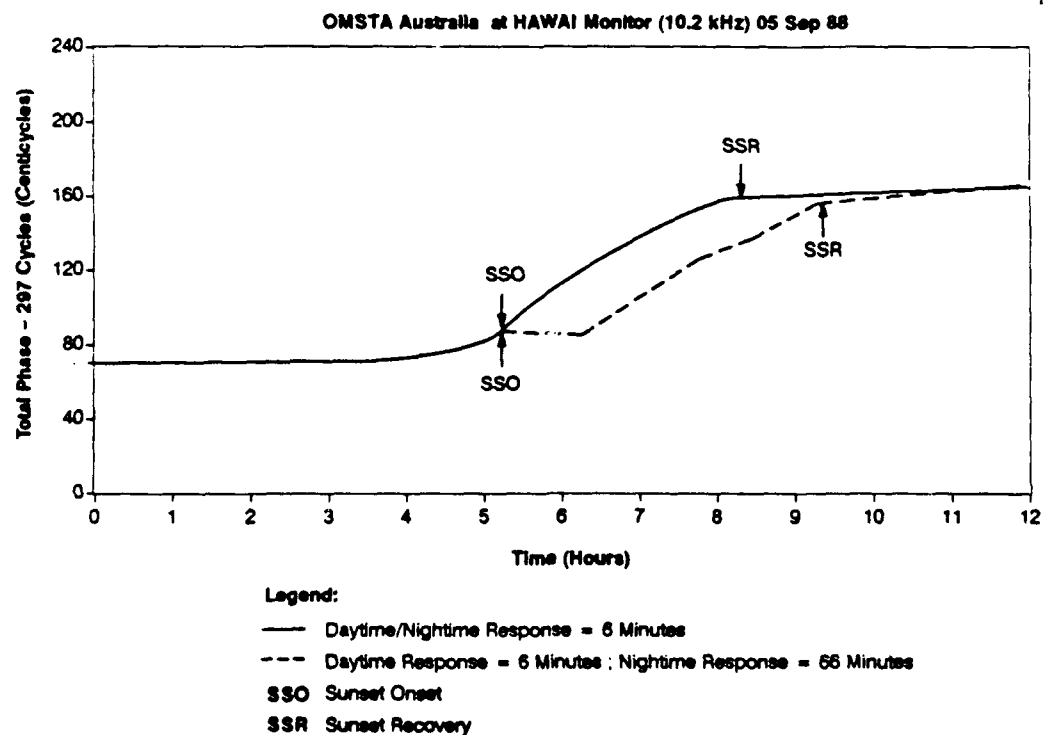SSO Sunset Onset

SSR Sunset Recovery

Figure B.3-3 Illustration of the Effect of Different Daytime and Nighttime Ionospheric Response Times on Diurnal Phase Behavior

REFERENCES

1. Pierce, J.A., *Intercontinental Frequency Comparison by Very Low Frequency Radio Transmission*, Vol. 45, pp. 794–806, June 1957.

2. Swanson, E.R., and Brown, R.P., *Omega Propagation Prediction Primer*, NELC Technical Note TN 2102, 1972.

3. Morris, P.B., and Cha, M.Y., *Omega Propagation Corrections: Background and Computational Algorithm*, ONSOD 01-74, December 1974.

4. Morris, P.B., and Swanson, E.R., *New Coefficients for the Swanson Propagation Correction Model*, Proceedings of the Fifth Annual International Omega Association Meeting, Bergen, Norway, August 1980.

5. Maenpa, J.E., *The 1985 Magnavox Omega Phase Propagation Correction Model*, Proceedings of the Tenth Annual International Omega Association Meeting, Brighton, U.K., July 1985.

6. Gupta, R.R., and Creamer, P.M., *Omega Phase Error Analysis: Phase Difference Error Assessment*, The Analytic Sciences Corporation, **Technical Report TR-1681-1**, August 1982.

7. Rishbeth, H., and Garriott. O.K., *Introduction to Ionospheric Physics*, Academic Press, 1969.

8. Chapman, S., *The Absorption and Dissociative or Ionizing Effect of Monochromatic Radiation in an Atmosphere on a Rotating Earth*, Proceeding of the Physical Society, Vol. 43, pp. 26–45, 1931.

9. Banks, P.M., and Kockarts, G., *Aeronomy (Parts A and B)*, Academic Press, 1973.

10. Meier, R.R., and Mange, P., *Geocoronal Hydrogen: An Analysis of the Lyman-alpha Airglow Observed from OGO-4*, Planetary and Space Science, Vol. 18, pp. 803–821, 1970.

11. Swanson, E.R., and Bradford, W.R., *Diurnal Phase Variation at 10.2 kHz*, NELC TR-1781, August 1971.

12. Ferguson, J.A., *A Report on the Integrated Prediction Program with Nuclear Environment (IPP-2)*, NELC TN 1890, July 1971.

13. Thrane, E.V., *On the Diurnal and Seasonal Variations of the D- and E-regions above Kjeller*, Magnetosphere-Ionosphere interactions, Proceedings of the Advanced Study Institute, Dalseter, Norway, 1971.

14. Berry, L.A., *Wavehop Theory of Long-distance Propagation of Low-frequency Radio Waves*, National Bureau of Standards, Journal of Research, Section D, Radio Science, Vol. 68, 1964.

15. Pappert, R.A., Gossard, E.E., and Rothmuller, I.J., *A Numerical Investigation of Classical Approximations Used in VLF Propagation*, Radio Science, Vol. 2, No. 4, April 1967.

16. Swanson, E.R., *Long-term Variation in Omega Phase*, Proceedings of the Fourteenth Annual International Omega Association, Long Beach, CA, October 1989.

REFERENCES (Continued)

17. Muraoka, Y., Murata, H., and Sato, T., *The Quantitative Relationship between VLF Phase Deviations and 1-8 Å Solar X-ray Fluxes during Solar Flares*, Journal of Atmospheric and Terrestrial Physics, Vol. 39, pp. 797-792, 1977.

18. Donnelly, S.F., *Integrated Propagation Prediction Program Documentation*, The Analytic Sciences Corporation, **Technical Report TR-343-4**, November 1973.

19. Morfitt, D.C., and Shellman, C.H., MODESRCH, *An Improved Computer Program for Obtaining ELF/VLF/LF Mode Constants in an Earth-Ionosphere Waveguide*, Naval Electronics Laboratory Center, NELC Interim Report No. 771, October 1976.

20. Wait, J.R., and Spies, K.P., *Characteristics of the Earth-Ionosphere Waveguide for VLF Radio Waves*, National Bureau of Standards, NBS Technical Note No. 300, December 1964.

21. *Two-Frequency 24-Hour/4-Month Omega Signal Coverage Database Development*, The Analytic Sciences Corporation, **Technical Report TR-5351-2**, September 1988.

22. Gupta, R.R., *Graphical Display of Omega Signal Modal Parameters*, The Analytic Sciences Corporation, **Engineering Memorandum EM-2650** (Volumes I and II), September 1987.

23. Gupta, R.R.. *Theoretical Background of IPP-2*, The Analytic Sciences Corporation, **Technical Report TR-343-2**, February 1973.